JETP Letters, Vol. 81, No. 3, 2005, pp. 102–107. Translated from Pis'ma v Zhurnal Éksperimental'noĭ i Teoreticheskoĭ Fiziki, Vol. 81, No. 3, 2005, pp. 133–138.

^{87}Rb NMR Study of the Magnetic Structure of the Quasi-Two-Dimensional Antiferromagnet $RbFe(MoO_4)_2$ on a Triangular Lattice

L. E. Svistov[1,3], L. A. Prozorova[1], N. Büttgen[2], A. Ya. Shapiro[3], and L. N. Dem'yanets[3]

[1] *Kapitza Institute for Physical Problems, Russian Academy of Sciences, ul. Kosygina 2, Moscow, 119334 Russia*
[2] *EP V, Center for Electronic Correlations and Magnetism, University of Augsburg, D-86135 Augsburg, Germany*
[3] *Shubnikov Institute of Crystallography, Russian Academy of Sciences, Leninskiĭ pr. 59, Moscow, 117924 Russia*

Received December 16, 2004

^{87}Rb nuclear magnetic resonance was experimentally studied in a quasi-two-dimensional Heisenberg antiferromagnet $RbFe(MoO_4)_2$. Dipole fields at the ^{87}Rb nuclei were found over a wide range of temperatures and static magnetic fields. Magnetic structures in the ordered phase were determined at various magnetic fields. © *2005 Pleiades Publishing, Inc.*

PACS numbers: 75.50.Ee, 76.60.–k

1. INTRODUCTION

The problem of establishing antiferromagnetic order on a planar triangular lattice has been intensively studied theoretically in [1–3]. In the Heisenberg and *XY* models, the ground state of such a system is a planar triangular spin structure, which can be described in terms of three sublattices with magnetic moments turned by 120° relative to each other. The orientation of the spin plane is arbitrary in the exchange approximation. Since the magnetic field does not remove the degeneracy in this system in the classical case, weak interactions and fluctuations play an important role in the determination of the structure. For instance, quantum and thermal fluctuations can play the key role in this system [1–3]. In particular, in the absence of fluctuations, a collinear phase is expected to appear only above the field $\frac{1}{3}B_{sat}$ (B_{sat} is the saturation field). At the same time, in the presence of fluctuations, it appears over a wide range of fields and results in the appearance of a characteristic plateau on the $M(H)$ curve at a level of one-third of the saturation magnetization. In iron molybdates $AFe(MoO_4)_2$ (A = K, Na, Rb, …), magnetic ions Fe^{3+} ($S = 5/2$) are situated at the sites of planar triangular lattices separated by layers of nonmagnetic $(MoO_4)^{2-}$ complexes and A^+ ions. Such a layered structure ensures the magnetic quasi-two-dimension character of these compounds [4, 5]. In the $RbFe(MoO_4)_2$ crystals containing a threefold axis (symmetry group D_{3d}^3), the regular triangular structure occurs in each of the magnetic layers, exhibiting the properties of a quasi-two-dimensional antiferromagnet ($T_N = 3.9$ K) with a ratio of 20 between the intra- and interplanar exchange integrals [5] and a magnetic anisotropy of the easy-plane type. Because of the presence of the interplanar exchange interaction and magnetic anisotropy, the magnetic B–T phase diagram of $RbFe(MoO_4)_2$ [5] is more complicated than the theoretical one obtained for two-dimensional antiferromagnets on a triangular lattice [1–3].

In this work, a ^{87}Rb NMR study was carried out to gain information on the magnetic structure of $RbFe(MoO_4)_2$ in the ordered state. The crystal structure of $RbFe(MoO_4)_2$ can be considered as a set of alternating layers of different ions situated perpendicularly to the threefold axis (C^3): $-Fe^{3+}-(MoO_4)^{2-}-Rb^+-(MoO_4)^{2-}-Fe^{3+}-$. Inside the layers, the ions form regular triangular lattices arranged in such a way that the Rb^+ ions and the nearest iron ions in the adjacent layers are positioned on the straight lines parallel to the C^3 axis [4]. The $(MoO_4)^{2-}$ complexes are not shown in Fig. 1.

Single-crystal samples of $RbFe(MoO_4)_2$ were grown by the spontaneous crystallization technique described in [4]. They were crystallized in the form of plates with a thickness of 0.5 mm and a linear in-plane size of up to 6 mm. The plate planes coincided with the layer planes.

The ^{87}Rb ($I = 3/2$, $\gamma = 13.9312$ MHz/T) NMR spectra of $RbFe(MoO_4)_2$ single crystals were studied by the spin-echo technique using a 5 μs–τ_D–10 μs pulse sequence, and the time τ_D between the pulses was equal to 50 μs. Measurements were performed on a hand made phase-detection spectrometer at a constant frequency in the range 35–114 MHz with magnetic-field

sweep in the range 2.5–9 T. The temperature was varied from 1.5 to 300 K and stabilized with an accuracy of better than 0.05 K using a standard flow-through cryostat (Oxford Instruments).

2. THE NMR RESULTS OBTAINED FOR THE $RbFe(MoO_4)_2$ SAMPLES IN THE PARAMAGNETIC PHASE

The NMR spectra recorded at a temperature of 6 K ($>T_N$) and a frequency of 38 MHz are presented in the upper panel in Fig. 1 for two orientations of the magnetic field: $\mathbf{B} \perp \mathbf{C_3}$ and $\mathbf{B} \parallel \mathbf{C_3}$. The NMR spectrum consists of three lines. The central line belongs to the $-1/2 \longleftrightarrow 1/2$ transition, and the satellites correspond to the $-3/2 \longleftrightarrow -1/2$ and $1/2 \longleftrightarrow 3/2$ transitions. The fact that the frequencies of these transitions do not coincide with each other is caused by the quadrupole interaction of the ^{87}Rb nucleus with the electric field gradient produced by the crystalline surroundings. The splitting for the field orientation $\mathbf{B} \parallel \mathbf{C_3}$ is approximately twice as large as that observed for $\mathbf{B} \perp \mathbf{C_3}$. Such a ratio between the quadrupole splittings is typical of a nucleus with spin $I = 3/2$ in an axial crystal field [6]. The NMR conditions corresponding to the transition from a level with quantum number m (–3/2, –1/2, 1/2) to a level with $m + 1$ can be written in the form

$$\nu_m = \gamma B + \gamma B_{\text{eff}} + \Delta\nu_m^q. \quad (1)$$

Here, B is the external magnetic field, B_{eff} is the effective magnetic field produced by the surrounding magnetic ions at the ^{87}Rb nucleus, and $\Delta\nu_m^q$ is the quadrupole contribution. In this work, NMR studies were performed in the frequency range for which the first term in Eq. (1) far exceeded the two remaining terms. The fact that the electron shells of the Rb^+ ion are filled and the nearest magnetic Fe^{3+} ions are spatially separated by the nonmagnetic $(MoO_4)^{2-}$ complexes suggests that B_{eff} is determined by the dipole fields. To reduce the possible experimental error caused by the imperfect orientation of the sample in the magnetic field upon changing the radio frequency of the exciting coils, the main information was acquired from the measured position of the central peak corresponding to the transition from the state with $m = -1/2$ to the state with $m = 1/2$. The value of $\Delta\nu_{-1/2}^q$ for this transition is nonzero only to the second order of perturbation theory and, according to [6], it should decrease as $1/B$ with increasing field. The field dependence measured at $T = 5$ K and $\mathbf{B} \perp \mathbf{C_3}$ for the deviation of the resonant NMR field B_{res} corresponding to the central line from the resonant field $B_0 = \nu/\gamma$ of a free rubidium nucleus is shown in Fig. 1a. In the paramagnetic phase, it is natural to expect that B_{eff} is proportional to the magnetic moment of the sample. At the indicated temperature, it obeys, with a good accuracy,

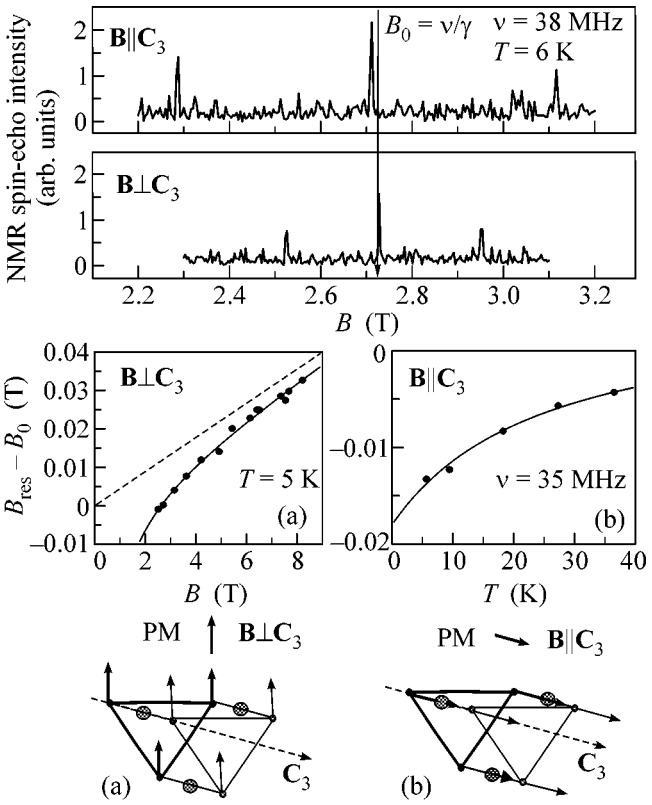

Fig. 1. Upper panel: the NMR spectra recorded in the paramagnetic phase. Middle panel: (a) field and (b) temperature dependences of the deviation of B_{res} corresponding to the central line from the resonant field $B_0 = \nu/\gamma$ of a free Rb^+ nucleus; the solid lines are fits by formula (2). Lower panel: the schemes of magnetic structures of the static magnetic field **B** oriented (a) perpendicular (in plane) and (b) parallel (out of plane) the $\mathbf{C_3}$ axis.

the Curie–Weiss law ($\Theta_{CW} = 25$ K) [5]. The solid line is a fit of the function

$$B_{\text{res}} - \nu/\gamma = B_{\text{eff}} + \Delta\nu_{-1/2}^q/\gamma = \frac{aB}{T + \Theta_{\text{CW}}} + \frac{b}{B} \quad (2)$$

to the experimental points, with the fitting parameters $a = 0.13 \pm 0.02$ K and $b = -0.03 \pm 0.005$ T^2. The parameter b can also be obtained from the quadrupole splitting observed for the $-3/2 \longleftrightarrow -1/2$ and $1/2 \longleftrightarrow 3/2$ transitions. Both b values coincided to within the indicated experimental error. The dashed straight line in Fig. 1 corresponds to the field dependence obtained for the first term in Eq. (2) by the fitting procedure. The positive sign of a indicates that the induced field at the ^{87}Rb nucleus is opposite to the direction of the external magnetic field. This means that the induced field B_{eff} is largely determined by the nearest Fe^{3+} ions (see Fig. 1a for the scheme of the magnetic structure). Using the data on the crystal structure and on the magnetic sus-

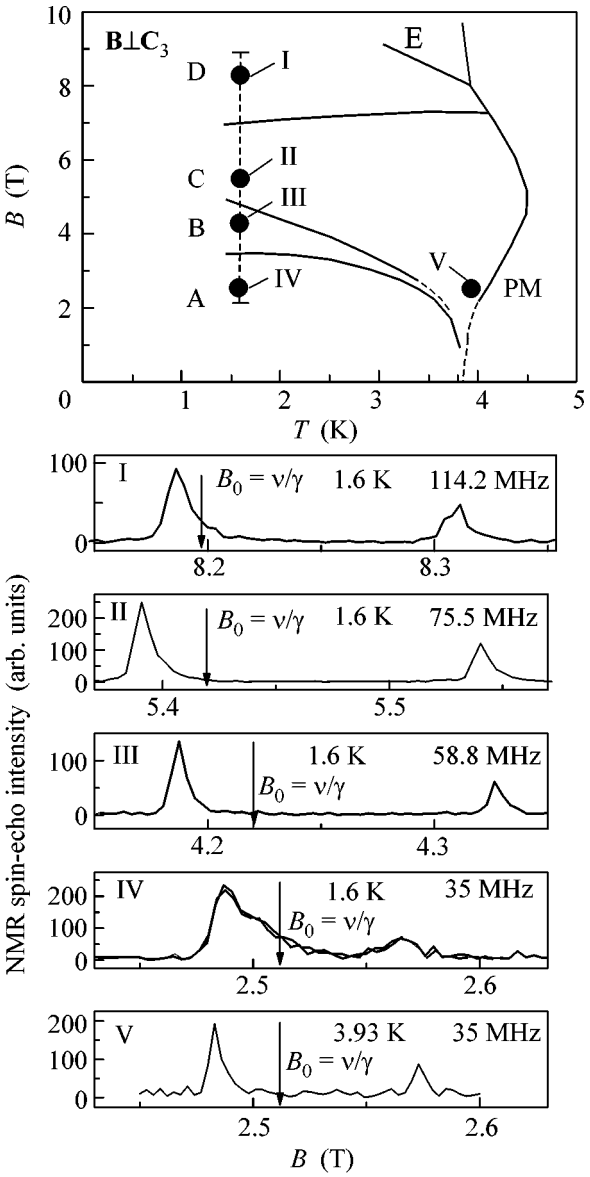

Fig. 2. Upper panel: the phase diagram experimentally obtained in [5, 7] for $RbFe(MoO_4)_2$ in the field oriented as $\mathbf{B} \perp \mathbf{C_3}$. Lower panel: the NMR spectra recorded at different frequencies for the central line ($-1/2 \longleftrightarrow 1/2$) in the magnetically ordered phase. The points on the phase diagram correspond to the values of B and T for which these spectra were recorded.

ceptibility, one can calculate the contribution to a from the dipole field produced by the magnetic Fe^{3+} ions. The corresponding calculations were carried out under the assumption that the dipole field is produced by the point dipoles situated at the positions of the Fe^{3+} ions. The dipole field was determined for the rubidium ion positioned at the center of a model disk-shaped sample whose thickness is equal to one-eighth of its diameter. The sample comprised ~10^5 unit cells, and B_D was determined by summing over the dipole fields of magnetic ions. Upon a proportional change in the sizes of the model sample by several times, the calculated value of a did not change with an accuracy of 5%. To check the computational procedure, the dipole fields B_D were also calculated for a spherical model sample. The calculated values differed from each other by the values corresponding to the differences in the demagnetizing fields. The resulting value of 0.12 K obtained for a is in good agreement with its experimental value.

Figure 1b shows the temperature dependence of the difference between the resonant NMR field B_{res} corresponding to the transition from $m = -1/2$ and the resonant field B_0 measured for the free ^{87}Rb nucleus at the frequency $\nu = 35$ MHz for $\mathbf{B} \parallel \mathbf{C_3}$. For this field orientation, B_{res} decreases with temperature because of a change in the sign of the dipole field at the ^{87}Rb nuclei produced by the nearest Fe^{3+} ions (see Fig. 1b for the scheme of the magnetic structure). The solid line in Fig. 1b is the fit using formula (2) with the parameters $a = -0.24 \pm 0.02$ K and $b = -0.013 \pm 0.008$ T^2. The measured a value coincides with its numerically obtained value $a = -0.244$ K.

Thus, one can conclude from the analysis of the NMR results for the paramagnetic phase that B_{eff} at the ^{87}Rb nucleus in $RbFe(MoO_4)_2$ is mainly determined by the dipole field produced by the magnetic Fe^{3+} ions.

3. THE NMR RESULTS FOR THE $RbFe(MoO_4)_2$ SAMPLES IN THE MAGNETICALLY ORDERED PHASE

The phase diagram experimentally obtained in [5, 7] for $RbFe(MoO_4)_2$ in the orientation $\mathbf{B} \perp \mathbf{C_3}$ is shown in the upper panel in Fig. 2. The magnetic phase diagram consists of at least six phases. The neutron-scattering study of the magnetic structure suggests [7] that the magnetic order in the basal plane is commensurate with the lattice spacing. The magnetic order is incommensurate along the C_3 axis at low fields (A phase) and commensurate with a period of triple the interplanar spacing at high fields (B, C, and D phases).

The NMR spectra recorded at a frequency of 102.5 MHz for the field orientation $\mathbf{B} \perp \mathbf{C_3}$ are shown in the upper panel in Fig. 3 for different temperatures. As the temperature decreases, each of the three NMR lines in the paramagnetic phase shifts toward higher fields and broadens as T_N is approached. Below the Néel temperature, each NMR line splits into two lines of different intensity. The more intense line shifts to lower fields, and the less intense one shifts to higher fields. The intensity ratio of the lines is equal to approximately 2 : 1. The temperature dependences of the corresponding NMR fields are shown in the same figure. The doubling of the NMR lines in the ordered state was observed for all commensurate phases. The examples of NMR spectra recorded at different frequencies for the $-1/2 \longleftrightarrow 1/2$ transitions at $T < T_N$ are shown in the

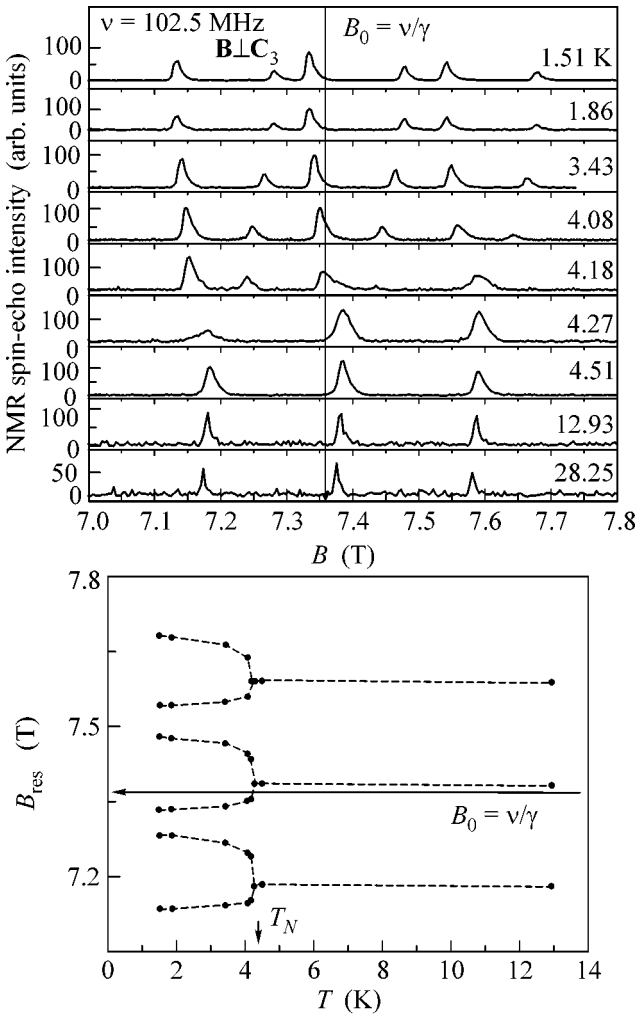

Fig. 3. Upper panel: the NMR spectra recorded at a frequency of 102.5 MHz and different temperatures for the magnetic-field orientation $\mathbf{B} \perp \mathbf{C_3}$. Lower panel: temperature dependences of the NMR fields.

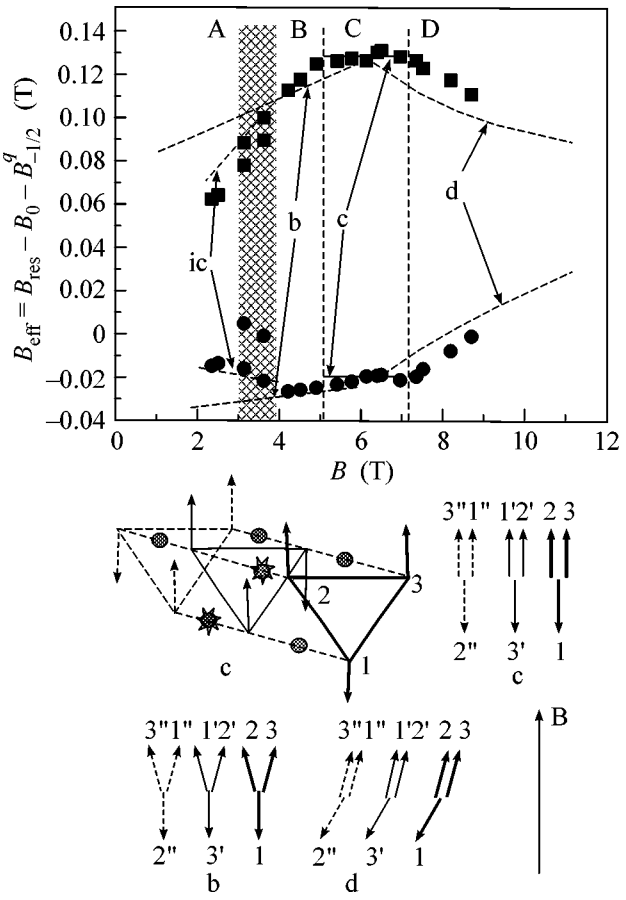

Fig. 4. Upper panel: dependences of the effective fields at the ^{87}Rb nuclei on the static magnetic field for $\mathbf{B} \perp \mathbf{C_3}$ and T = 1.6 K. The effective fields at the ^{87}Rb nuclei whose NMR signal is more intense are denoted by circles, and squares correspond to the nuclei whose signal is less intense. Lower panel: the schemes of magnetic structures for the commensurate phases *b*, *c*, and *d*.

lower panel in Fig. 2. The points in the phase diagram correspond to the B and T values for which these spectra were recorded. One can see that spectra I, II, III, and V recorded in the commensurate phases *B*, *C*, and *D* consist of two lines corresponding to two ^{87}Rb positions at which the effective fields are different. In compliance with the intensity ratio of the NMR lines, one can state that the number of the first positions is two times larger than the number of the second positions.

The NMR spectrum in the incommensurate phase *A* is different (Fig. 2, IV). The spin-echo signal was observed over a wide range of fields. Such a spectrum shape is evidence of a continuous distribution of effective fields at the ^{87}Rb nuclei in the *A* phase.

The field dependences of the effective fields at the ^{87}Rb nuclei for $\mathbf{B} \perp \mathbf{C_3}$ and T = 1.6 K are presented in Fig. 4. All points in the graph were obtained for the resonant fields corresponding to the $-1/2 \longleftrightarrow 1/2$ transition. The value of the parameter *b* determining the correction to the resonant field due to the quadrupole interaction was taken from the measurements carried out in the paramagnetic phase. The circles denote the effective fields at the ^{87}Rb nuclei whose signal is more intense, and the squares are for the nuclei giving a less intense signal. For the incommensurate *A* phase, the circles and squares indicate the positions of the echo-signal intensity maxima as a function of the field *B*. The region of fields corresponding to the phase transition from the incommensurate *A* phase to the commensurate *B* phase is darkened in Fig. 4. According to the results obtained in [5, 7], this transition has a hysteretic character. In this region, the NMR lines were observed for different phases *A* and *B* simultaneously, and their intensity ratio was found to depend on the directions of field and temperature scans.

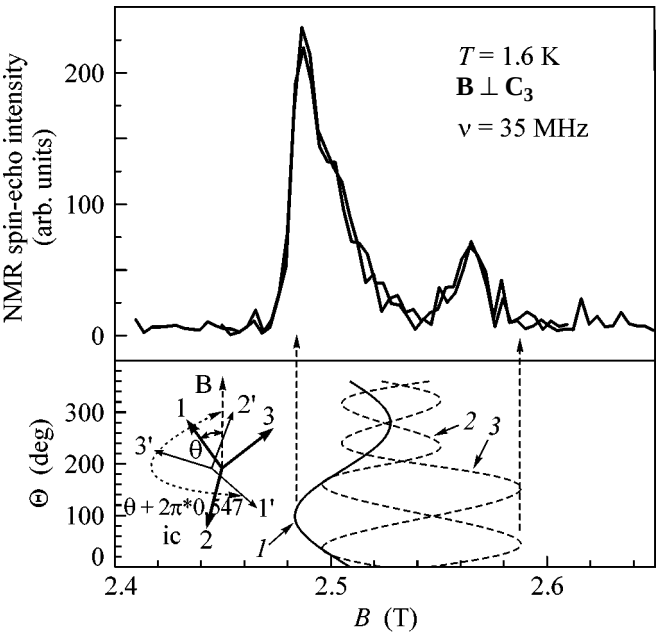

Fig. 5. Upper panel: the NMR spectra recorded at a temperature of 1.6 K and a frequency of 35 MHz for the magnetic-field orientation $\mathbf{B} \perp \mathbf{C_3}$. Lower panel: NMR fields for the three possible positions of the Rb^+ ion in a model structure, as calculated for different Θ angles between the direction of the magnetic moment of the first sublattice and the direction of the field **B**.

In the analysis of magnetic structures, we used the approach proposed in [8]. We assume that the choice of magnetic structures arising in the Fe^{3+}-containing planes is independent of the interplanar exchange, whereas the weak interplanar antiferromagnetic interaction defines the mutual arrangement of the triangular magnetic structures along the C_3 axis and only slightly changes the orientation of sublattices in the triangular structure. The schemes of magnetic structures in the commensurate *b*, *c*, and *d* phases are presented in the lower panel in Fig. 4. In the scheme of a magnetic unit cell of the magnetic structure *c*, the magnetic Fe^{3+} ions are at the vertices of triangles and the Rb^+ ions are denoted by circles and asterisks. For all phases, the schemes of magnetic structures are presented in the notation suggested in [8]. The positions of magnetic ions in the unit cell are denoted by the numerals 1, 2, and 3, differently primed according to their assignment to the different layers of the layered structure. The Rb^+ ions are situated between the Fe^{3+} ions that have identical numerical indices.

One can see from the figure that Rb^+ ions in the magnetic structures *c* and *d* occupy two nonequivalent positions with different magnetic surroundings. The positions of the Rb^+ ions between the $Fe^{3+}2$–$Fe^{3+}2'$ and $Fe^{3+}1'$–$Fe^{3+}1''$ ions are different from all other positions in the magnetic unit cell. In the first case, the magnetic moments of the nearest Fe^{3+} ions are co-directed, while, for the other positions, they are antiparallel. The number of first positions is half that of the second ones. The positions of the ions with co-directed nearest surroundings are asterisked in the scheme of a magnetic unit cell in Fig. 4.

Although there are three magnetically nonequivalent Rb^+ positions in the *B* phase with the magnetic structure *b*, the magnetic surroundings of two of them are mirror symmetric about the plane parallel to **B** and perpendicular to the crystal basal plane; for this reason, the projections of the effective magnetic fields onto the direction of the external magnetic field at the ^{87}Rb nuclei should be the same for these positions.

Therefore, the presence of two NMR lines with an intensity ratio of 1 : 2 can be explained within the framework of the magnetic phases considered above.

It is natural to expect that, as in the case of a paramagnetic phase, the field induced at the ^{87}Rb nuclei by the magnetic surroundings in the ordered phase is mainly determined by the dipole fields. The dipole fields at the ^{87}Rb nuclei have been calculated for the magnetic *b*, *c*, and *d* phases. The best agreement with the experimental values of effective fields observed in the collinear magnetic structure *c* has been obtained on the assumption that the magnetic moment of the Fe^{3+} ions is equal to $(0.87 \pm 0.01)g\mu_B S$. The values of dipole fields calculated for this magnetic moment are shown in Fig. 4 by the horizontal solid lines within the **C** phase. The reduction of magnetic moment measured [7] for the Fe^{3+} ion at low fields is equal to a value close to 0.75. In the calculation of the dipole fields in the *b*, *d*, and incommensurate (*ic*) phases, the magnetic moment of Fe^{3+} was assumed to be the same as in the *c* phase. The dipole fields have been calculated for the magnetic structures with periods of two and three interplanar spacings along the C^3 axis; for these cases, the calculated B_D values proved to be nearly identical.

To determine the angles in the magnetic *b* and *d* structures, the results of molecular field calculations [8] with the parameters $J'/J = 0.04$ and $B_{sat} = 18.5$ T [5] have been used. The calculated $B_D(B)$ curves are shown in Fig. 4 by the dashed lines. The discrepancy between the experimental and calculated dependences is likely caused by the fact that the thermal and quantum fluctuations were disregarded in the model. The calculations of the dipole fields at the Rb ions in the incommensurate *A* phase have been carried out for the model in which the magnetic moment of one of the sublattices (lattice 1 in the inset in Fig. 5) is turned by an angle of $2\pi \times 0.453$ upon the transition to the second plane, while the positions of the remaining two sublattices in each plane are determined by the in-plane exchange constant *J* in the triangular structure and the magnetic field **B**. Such a turn angle was chosen to ensure the value of an incommensurate wave vector obtained in [7] for the direction along the C_3 axis. In spite of the fact that the model used in this work is rather crude, it

accounts for the main features of the NMR spectrum observed in the range of fields corresponding to the *A* phase. In the lower panel in Fig. 5, the 35-MHz NMR fields are shown for the three possible positions of the Rb^+ ion in the model structure, as calculated for the different angles Θ between the direction of the magnetic moment of the first sublattice and the direction of the **B** field. One can see that the experimental and calculated ranges of fields for which the NMR signal is observed almost coincide with each other. The calculated boundaries of the regions where the NMR signal is observed in the incommensurate phase are shown in Fig. 4 by the dashed lines.

As is seen in Fig. 5, the number of Rb^+ ions whose NMR resonant field is at the edges of the NMR spectrum is greater than the number of ions having intermediate values of resonant field. This explains the intensity maxima observed in the experiment.

Thus, one can conclude that the commensurate magnetic structures *B*, *C*, and *D* in the quasi-two-dimensional $RbFe(MoO_4)_2$ correspond to the phases in a two-dimensional model of an antiferromagnet on the triangular lattice [1, 8].

We are grateful to S.E. Korshunov, V.I. Marchenko, A.I. Smirnov, H. Benner, A. Loidl, and H.-A. Krug von Nidda for discussions. This work was supported by the Russian Foundation for Basic Research (project no. 04-02-17294), the Council of the President of the Russian Federation for Support of Young Russian Scientists and Leading Scientific Schools, the Bundesministerium für Bildung und Forschung (contract no. VDI/EKM 13N6917-A), and the German Research Society Sonderforschungsbereich 484 (Augsburg). The work of L.E.S. is supported by an Alexander von Humboldt scholarship.

REFERENCES

1. S. E. Korshunov, J. Phys. C: Solid State Phys. **19**, 5927 (1986).
2. A. V. Chubukov and D. I. Golosov, J. Phys.: Condens. Matter **3**, 69 (1991).
3. E. Rastelli and A. Tassi, J. Phys.: Condens. Matter **8**, 1811 (1996).
4. R. F. Klevtsova and P. V. Klevtsov, Kristallografiya **15**, 953 (1970) [Sov. Phys. Crystallogr. **15**, 829 (1970)].
5. L. E. Svistov, A. I. Smirnov, L. A. Prozorova, *et al.*, Phys. Rev. B **67**, 094434 (2003).
6. G. C. Carter, L. H. Bennett, and D. J. Kahan, *Metallic Shifts in NMR* (Pergamon, Oxford, 1977), Part 1.
7. G. Gasparovich, M. Kenzelman, C. Broholm, *et al.*, in *Proceedings of March Meeting of APS* (2003), Session 31.
8. R. S. Gekht and I. N. Bondarenko, Zh. Éksp. Teor. Fiz. **111**, 627 (1997) [JETP **84**, 345 (1997)].

Translated by V. Sakun

JETP Letters, Vol. 81, No. 3, 2005, pp. 108–111. Translated from Pis'ma v Zhurnal Éksperimental'noĭ i Teoreticheskoĭ Fiziki, Vol. 81, No. 3, 2005, pp. 139–143.

Collective Behavior of a Spin-Aligned Gas of Interwell Excitons in Double Quantum Wells

A. V. Larionov[1], M. Bayer[2], J. Hvam[3], and K. Soerensen[3]

[1] *Institute of Solid-State Physics, Russian Academy of Sciences, Chernogolovka, Moscow region, 142432 Russia*

[2] *Experimentelle Physik II, Dortmund University, D-44221 Dortmund, Germany*

[3] *Microelectronic Center, DK 2800 Lyngby, Denmark*

Received December 20, 2004

The kinetics of a spin-aligned gas of interwell excitons in GaAs/AlGaAs double quantum wells (*n–i–n* heterostructure) is studied. The temperature dependence of the spin relaxation time for excitons, in which a photoexcited electron and hole are spatially separated between two adjacent quantum wells, is analyzed. For this purpose, use was made of pulsed circularly polarized resonant photoexcitation of intrawell 1*sHH* excitons by a femtosecond frequency-controlled laser. A sharp increase in the spin-relaxation rate is observed for interwell excitons upon a change in temperature from 2 to 3.6 K. This effect is associated with indirect evidence of the coherence of the collective phase of interwell excitons at temperatures below the critical value. © *2005 Pleiades Publishing, Inc.*

PACS numbers: 73.20.Mf, 73.21.Fg

1. Spin-aligned excitons excited by circularly polarized light have long been studied in bulk semiconductors. The main mechanisms of spin relaxation have been established in a wide temperature range for various types of semiconductors [1]. At the beginning of the last decade, the spin relaxation of electrons and holes was studied in detail experimentally and theoretically in connection with obtaining a new class of low-dimensional semiconducting heterostructures [2–5]. At present, interest in spin phenomena in semiconductors has been revived in light of their possible application in spintronic devices.

In quantum wells (QWs) of GaAs semiconducting heterostructures, the ground state 1*sHH* of a heavy-hole exciton is fourfold spin-degenerate. The state with angular momentum $m = \pm 1$ is optically active, while excitons with angular momentum $m = \pm 2$ are optically inactive. In GaAs/AlGaAs double quantum wells (DQWs) to which a bias voltage inclining the energy bands is applied, excitons can be excited with the electron and hole in different QWs separated by a tunnel-transparent barrier. Such excitons are referred to as spatially indirect or interwell excitons, in contrast to intrawell direct excitons, in which the electron and hole are in the same QW. In the case of photoexcitation, intrawell excitons are formed due to tunneling of electrons to the lowest quantum well and their coupling with holes in the adjacent quantum well. The ground state of intrawell excitons is also fourfold degenerate in spin. As compared to intrawell excitons, intrawell excitons are long-lived in light of the limited overlapping of the wave functions for the electron and the hole via the tunnel barrier; for this reason, such excitons can be easily accumulated and cooled to low temperatures.

It was found earlier [6–8] that a gas of interwell excitons (with a concentration on the order of 10^{10} cm^{-2}) at low temperatures (about 2 K) exhibits a collective behavior. This is manifested in a sharp narrowing of the photoluminescence line corresponding to radiative recombination of intrawell excitons, a superlinear increase in its intensity, and a shift to the long-wave spectral region. The intrawell-exciton lifetime becomes shorter, and the observed effect is critical in temperature ($T_c \leq 4$ K). It was found that this phenomenon occurs in domains, viz., large-scale fluctuations of the random potential in the plane of QWs playing the role of traps for intrawell excitons [9]. The question concerning the coherence of the collective exciton phase remains unanswered.

This study is aimed at analysis of the temperature dependence of the intrawell-exciton spin-relaxation rate under the conditions when the collective behavior of a dense intrawell-exciton gas is observed. The results of this study could help to draw conclusions on possible coherence of this intrawell-exciton state at temperatures below the critical value.

2. We studied *n–i–n* GaAs/AlGaAs heterostructures with a GaAs/AlAs/GaAs DQW and a narrow tunnel AlAs barrier between the wells (the width of the GaAs QW was approximately 120 Å, and the width of the four-monolayer AlAs barrier was ~11 Å). The entire structure was grown using molecular-beam epitaxy on a doped *n*-type GaAs substrate with the (001) crystallographic orientation and with a concentration of Si doping impurity of 10^{18} cm^{-3}. First, a 0.5-μm-thick GaAs

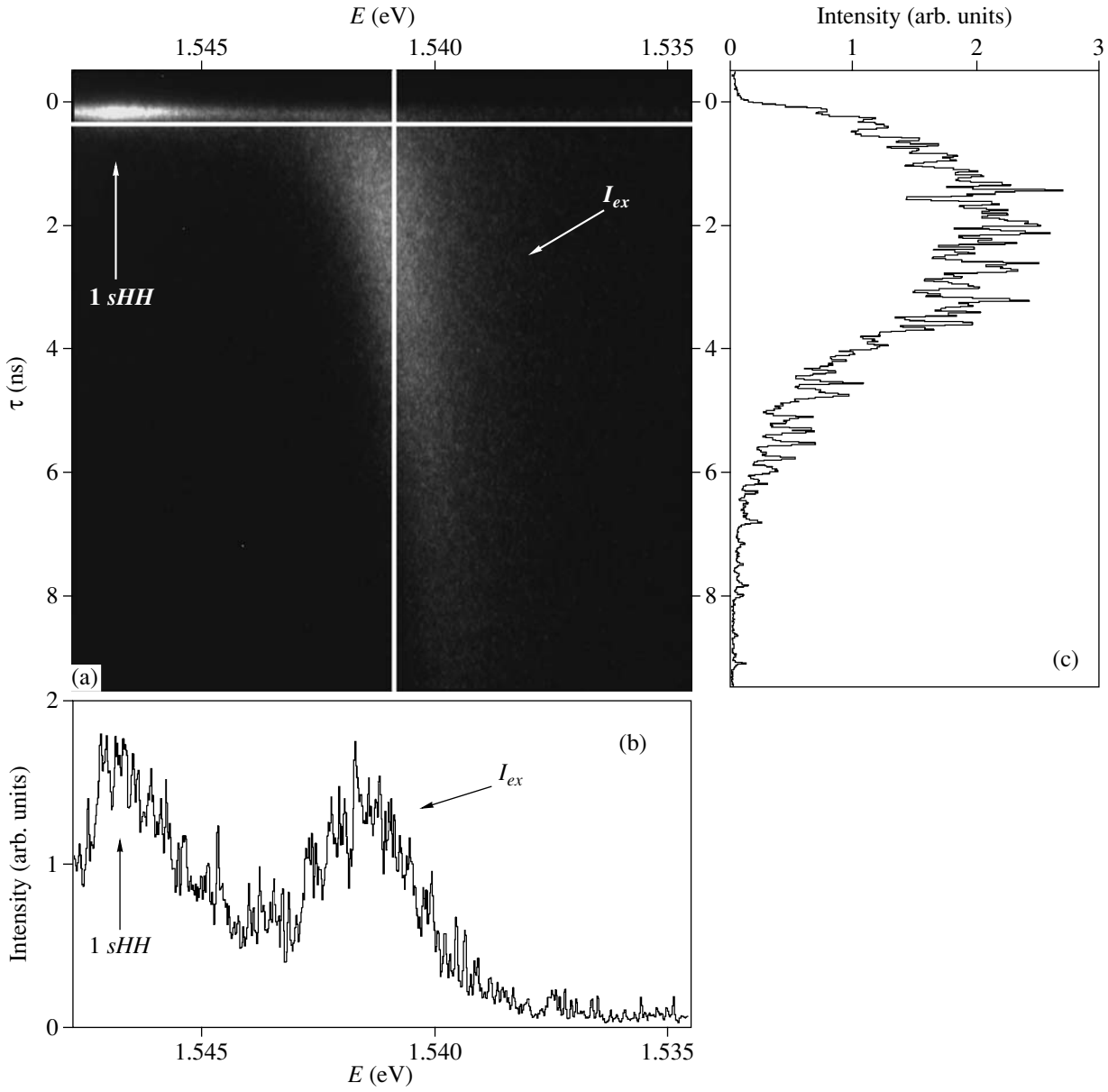

Fig. 1. (a) Image of a photoluminescence signal obtained with a streak camera as a result of the excitation of the sample by a short (about 1 ps) laser pulse. The brightness at a given point in the figure corresponds to the photoluminescence intensity. (b) Horizontal image cross section [the corresponding horizontal straight line in (a) is the photoluminescence spectrum at a fixed time]. (c) Vertical cross section [the corresponding vertical straight line in (a) is the photoluminescence decay curve at a fixed wavelength]. Arrows show the positions of an intrawell exciton (1*sHH*) and an intrawell exciton (I_{ex}). The image is obtained for a bias voltage $U = 0.65$ V and $T = 1.85$ K.

buffer layer doped with Si (10^{18} cm^{-3}) was grown on the substrate. Then, a 0.15-μm-thick insulating AlGaAs layer ($x = 0.33$) was grown, followed by the GaAs/AlAs/GaAs DQW. The heterojunction of each GaAs QW with an AlGaAs insulating layer was also separated by a narrow (four-monolayer) AlAs barrier. The narrow AlAs barriers were grown using the epitaxial stop growth technique. With such a growth technique, the fluctuations in the width of AlAs barriers are of the large-scale type. Above the DQW layer, there was a 0.15-μm-thick AlGaAs insulating layer, followed by a 0.1-μm-thick GaAs layer doped with Si (10^{18} cm^{-3}). The top of the structure was coated by a 100-Å GaAs layer. On the structure grown in this way, 1 × 1-mm mesas were prepared lithographically. Metal contacts made of an Au–Ge–Pt alloy were deposited in the form of a rectangular frame on the buffer layer in the upper part of the mesa.

To study the time evolution of a spin-aligned intrawell-exciton gas, we used a frequency-controlled

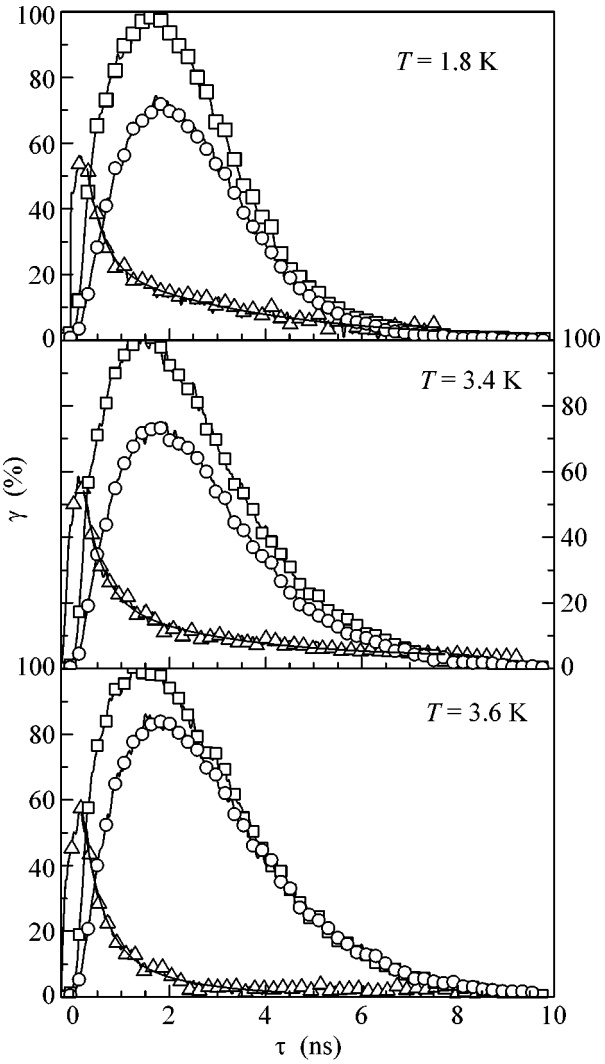

Fig. 2. Photoluminescence decay curves for intrawell excitons at different temperatures. Squares and circles show the photoluminescence decay curves corresponding to circular polarizations σ^+ and σ^-, respectively; triangles show the circular-polarization degree γ. Solid curves along γ are the least-squares fits using two-exponential decay. The curves correspond to an applied voltage $U = 0.55$ V.

pulsed femtosecond Ti–sapphire laser (Mira-900, Coherent). To obtain the required resonant photoexcitation, a laser pulse was preliminarily passed through a medium with positive dispersion (diffraction grating), which led to spectral narrowing of the pulse and to a change in its duration (from 140 fs to 1 ps). Optical orientation of the angular momentum of intrawell excitons was carried out using circularly polarized light obtained with the help of a quarter-wave plate. The photoluminescence signal passed through a single monochromator (Acton SP-500i) with a linear dispersion of 34 Å/mm and was detected by a 5680-24 Hamamatsu streak camera. Such a system made it possible to obtain simultaneously the time evolution of the entire photoluminescence spectrum with a time resolution of about 80 ps.

3. Figure 1a shows the typical shape (image) of a photoluminescence signal, obtained using the streak camera by excitation of the sample under study by a short (about 1 ps) laser pulse. This image is a 3D object in the energy–time–intensity coordinates (the intensity is shown in the form of the gradations of color or brightness in the case under consideration). Thus, the image contains complete information on the time evolution of the photoluminescence spectra. To analyze the information, cross sections (profiles) along the energy scale (the result is shown in Fig. 1b) and along the time scale (the result is shown in Fig. 1c) are used. In this study, we analyzed the photoluminescence decay curves corresponding to cross sections along the time scale.

Figure 1 was obtained for the resonant excitation of an intrawell 1*sHH* exciton by a laser pulse (with a wavelength of 1.549 eV) with a bias voltage $U = 0.65$ V at a temperature of 1.85 K. The excitation was carried out with circularly polarized light. The arrows show the line of intrawell (1*sHH*) and interwell (I_{ex}) excitons. The peak density of excitation power was approximately 30 kW/cm^2, which corresponds to the intrawell-exciton concentration $n_{ex} \sim 3 \times 10^{10}$ cm^{-2} according to our estimates.

In this study, we investigated the temperature variation of the intrawell-exciton spin-relaxation rate. For this purpose, intrawell-exciton photoluminescence was excited with the help of circularly polarized laser radiation (e.g., with the σ^+ polarization) in resonance with the ground state of an intrawell exciton and the time dependence of the degree of circular polarization of the photoluminescence signal was analyzed at various temperatures. Figure 2 shows an example of such a temperature dependence for $U = 0.6$ V. The decay curves were obtained for a photoluminescence signal image cross section of ±0.3 meV at the peak of the intrawell-exciton curve. Squares and circles correspond to the σ^+ and σ^- components, while triangles show the degree of circular polarization calculated by the formula $\gamma = (I_{\sigma^+} - I_{\sigma^-})/(I_{\sigma^+} + I_{\sigma^-})$. Bold solid curves plotted along the profile of the curves corresponding to the degree of circular polarization are the results of fitting to the two-exponential decay with the help of the least-squares technique. It can be seen from these curves that, with increasing temperature, the initial decay time (τ_1) varies with temperature insignificantly and amounts to approximately 0.35 ns. On the other hand, the decay time τ_2, which is longer than τ_1 by almost an order of magnitude, decreases sharply by a factor of 1.5–2 at temperatures above 3.5 K. At higher temperatures (up to 15 K), the degree of circular polarization exhibits no substantial variations in its time dynamics. An analogous behavior was also observed under other bias voltages, as is seen in Fig. 3.

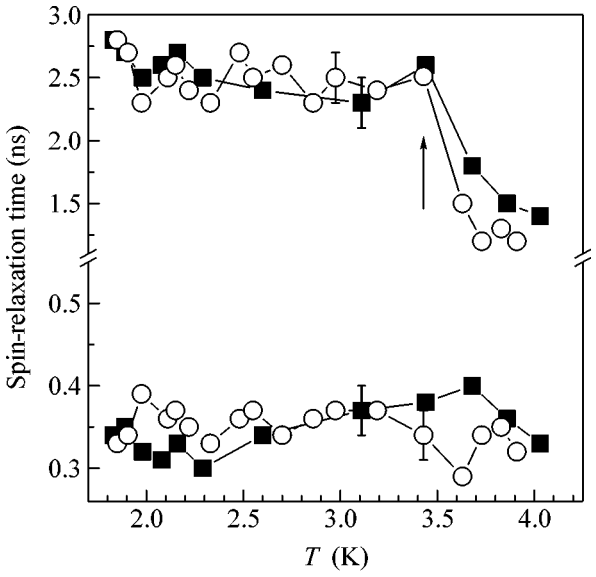

Fig. 3. Summary plot of the temperature dependence of small τ_1 and large τ_2 spin-relaxation time for applied voltage U = (circles) 0.6 and (squares) 0.55 V. The arrow indicates the temperature region where the spin-relaxation time changes abruptly.

For comparison, we measured the temperature dependence of the degree of circular polarization of an intrawell 1*sHH* exciton. In the temperature range from 2 to 15 K, the spin relaxation time remains nearly unchanged to within 15% and is equal to about 180 ps. The decay curve for the degree of circular polarization is single-exponential. These results are in good agreement with those obtained in [2], where the spin-relaxation dynamics was studied in detail for excitons in single QWs at low temperatures. According to the results obtained in [2], the electron–hole exchange interaction is the mechanism responsible for spin relaxation of 1*sHH* excitons at low temperatures. In our case, the dynamics of charge carriers is more complicated. After the arrival of a laser pulse, a part of the electrons tunnel to the adjacent QW, and energy and spin-relaxation processes, as well as the process of intrawell-exciton formation, come into play. This takes about 2 ns. After this, traditional emission of interwell excitons takes place. We believe that the time τ_1 is associated with one of the one-particle relaxation mechanisms [5], while τ_2 is due to peculiarities of spin relaxation inherent in excitons. The exchange interaction plays a major role in this case, but this time for intrawell excitons is an order of magnitude longer than τ_1 in light of the smallness of the overlap integral for the wave functions of electrons and holes.

4. In our opinion, the experimental results reported above indicate the coherence of the collective phase for intrawell excitons at low temperatures. The grounds for such a statement can be found in the work by Kagan *et al.* [10], who studied, among other things, the spin-relaxation rate for the Bose-condensed state in atomic traps. They proved that the rate of spin relaxation for the condensed phase is lower by a factor of $N!$ than for the phase above the condensate (N is the number of particles forming a boson). The results obtained in [10] were confirmed in [11, 12], where, in particular, the spin dynamics of atoms in a Bose condensate was studied. In our case, the time τ_2, which reflects the intrawell-exciton relaxation process, changes by a factor of 1.5–2. This is in good qualitative agreement with the results obtained in [10].

Thus, we have studied the temperature dependence of the spin-relaxation time for interwell excitons in GaAs/AlGaAs QWs. A sharp (by a factor of 1.5–2) increase in the intrawell-exciton spin-relaxation rate was detected for $T > T_c = 3.5$ K. This phenomenon is attributed to the coherence of the collective phase of intrawell excitons at temperatures below the critical point.

We are grateful to V.B. Timofeev for valuable remarks and suggestions and to Yu.M. Kagan for fruitful and interesting discussions. This work was supported by Deutsche Forschungsgemeinschaft (grant no. 436 RUS 17/95/03) and the Russian Foundation for Basic Research (project no. 04-02-17348).

REFERENCES

1. *Optical Orientation*, *Modern Problems in Condensed Matter Science*, Ed. by F. Meier and B. P. Zakharchenya (North-Holland, Amsterdam, 1984; Nauka, Leningrad, 1989).
2. A. Vinattieri, J. Shah, T. C. Damen, *et al.*, Phys. Rev. B **50**, 10868 (1994).
3. A. Frommer, A. Ron, E. Cohen, *et al.*, Phys. Rev. B **50**, 11833 (1994).
4. M. Z. Maialle, E. A. de Andrada e Silva, and L. J. Sham, Phys. Rev. B **47**, 15776 (1993).
5. N. S. Averkiev, L. E. Golub, and M. Willander, J. Phys.: Condens. Matter **14**, R271 (2002).
6. A. V. Larionov, V. B. Timofeev, J. Hvam, and C. Soerensen, Pis'ma Zh. Éksp. Teor. Fiz. **71**, 174 (2000) [JETP Lett. **71**, 117 (2000)].
7. A. V. Larionov, V. B. Timofeev, J. M. Hvam, and C. Soerensen, Zh. Éksp. Teor. Fiz. **117**, 1255 (2000) [JETP **90**, 1093 (2000)].
8. A. V. Larionov and V. B. Timofeev, Pis'ma Zh. Éksp. Teor. Fiz. **73**, 342 (2001) [JETP Lett. **73**, 301 (2001)].
9. A. V. Larionov, V. B. Timofeev, J. M. Hvam, and C. Soerensen, Pis'ma Zh. Éksp. Teor. Fiz. **75**, 699 (2002) [JETP Lett. **75**, 570 (2002)].
10. Yu. Kagan, V. A. Kashurnikov, A. V. Krasavin, *et al.*, Phys. Rev. A **61**, 043 608 (2000).
11. E. A. Burt, R. W. Ghrist, C. J. Myatt, *et al.*, Phys. Rev. Lett. **79**, 337 (1997).
12. C. J. Myatt, E. A. Burt, R. W. Ghrist, *et al.*, Phys. Rev. Lett. **78**, 586 (1997).

Translated by N. Wadhwa

JETP Letters, Vol. 81, No. 3, 2005, pp. 112–116. From Pis'ma v Zhurnal Éksperimental'noĭ i Teoreticheskoĭ Fiziki, Vol. 81, No. 3, 2005, pp. 144–148.

Bound States in a Quantized Hall Ferromagnet¶

S. Dickmann

Institute for Solid State Physics, Russian Academy of Sciences, Chernogolovka, Moscow region, 142432 Russia

Received December 21, 2004

We report on a study of the quasielectron–quasihole and skyrmion–antiskyrmion bound states in the $\nu = 1$ quantum Hall regime. The short-range attraction potential is assumed to be determined by a point magnetic impurity. The calculations are performed within the strong-field approximation when the binding energy and the characteristic electron–electron interaction energy are smaller than the Landau level spacing. The excitonic representation technique is used in that case. © *2005 Pleiades Publishing, Inc.*

PACS numbers: 73.43.–f, 75.70.Cn

1. The unique properties of a two-dimensional electron gas (2DEG) in strong magnetic fields attract much attention to its spectrum. In particular, the interaction of 2DEG with neutral short-range impurities exhibits unusual features in comparison with its 3D prototype [1, 2]. In this paper, we study the bound fermion states appearing in the *quantum Hall "ferromagnet"* (QHF) regime; i.e., the filling factor is $\nu = \mathcal{N}/N_\phi \simeq 2n + 1$, where $\mathcal{N}$ and $N_\phi = L^2/2\pi l_B^2$ are the numbers of electrons and magnetic flux quanta (L^2 is the 2DEG area; l_B is the magnetic length). In the high magnetic field limit, which really represents the case in which the solution to the first order in the ratio $r_c = (e^2/\varepsilon l_B)/\hbar\omega_c$ is considered to be small (ω_c is the cyclotron frequency; ε is the dielectric constant), we get the ground state, with the zeroth, first, second, … and $(n-1)$th Landau levels (LLs) fully occupied and with the nth level filled only by spin-up electrons aligned along **B**.

In the clean limit, fermion excitations are classified by their spin numbers $|\Delta S_z| = K + 1/2$ (K is an integer) [3], ranging from the simplest $|\Delta S_z| = 1/2$ case of quasielectrons or quasiholes to the $K \longrightarrow \infty$ limit, which corresponds to the so-called skyrmions. Certainly, the total energy of excitations incorporates the Zeeman energy $|\epsilon_Z \Delta S_z|$, and the spin number of lowest lying fermions is thus determined by the actual value of the gap $\epsilon_Z = |g\mu_B B|$. With regard to the Coulomb exchange energy of the fermions, in the $\nu = 1$ case this part of the total energy decreases monotonically with the K number [3]. For example, to the first order in r_c, the exchange energies are $-\frac{1}{4}\sqrt{\pi/2}\, e^2/\varepsilon l_B$ and $\frac{3}{4}\sqrt{\pi/2}\, e^2/\varepsilon l_B$ (in the strict 2D limit) for electron-like and hole-like skyrmions, respectively [4–8]. For comparison, in the $K = 0$ case, these are 0 (electrons) and $\sqrt{\pi/2}\, e^2/\varepsilon l_B$ (holes).

We calculate the bound-state energies in the presence of point impurities. In the single-electron approximation (i.e., in the $\nu \ll 1$ case), this problem was studied in [2] for an arbitrary strength of the perpendicular magnetic field. In [9, 10], the authors investigated the genesis of the impurity potential in the 2D channel and gave a proof for the short-range approach. The latter in terms of the "envelope" wavefunction method means that the impurity Hamiltonian can be modeled by the δ function:

$$\hat{H}_{\text{imp}} = 2\pi\left(W\hat{\mathbf{1}} + \frac{D}{2}\hat{\sigma}_z\right)\delta(\mathbf{r}) \qquad (1)$$

(here and in the following, $\hat{\sigma}_x$, $\hat{\sigma}_y$, and $\hat{\sigma}_z$ are the Pauli matrices). The $D \neq 0$ case corresponds to a paramagnetic impurity with its own magnetic moment aligned parallel to the magnetic field. (We consider that $\mathbf{B} \parallel \hat{z}$.) At a negative g factor, the positive value of D provides for the capture of the spin wave (spin exciton) by an impurity in the QHF case [9].

We will solve the problem in the "shallow" impurity approximation,

$$|W_\sigma| \ll \hbar^2/m_e^* \quad (\sigma = \uparrow, \downarrow), \qquad (2)$$

where $W_{\uparrow,\downarrow} = W \pm D/2$. Actually, we will see that this condition enables one to employ the high magnetic field approach:

$$E_b \ll \hbar\omega_c, \qquad (3)$$

where E_b is the desired binding energy and ω_c is the cyclotron frequency. Condition (3) allows us to employ the projection onto a single LL approach when calculating E_b in the leading approximation. At the same time, we still assume that the point-impurity approximation

¶ This article was submitted by the author in English.

is not disturbed, i.e., that the impurity localization radius ρ_b is much smaller than the magnetic length: $\rho_b \ll l_B$.

2. Any single-electron state may be presented in the form of the expansion

$$\chi = \sum_{ap} c_{ap}\phi_{ap}, \tag{4}$$

where we choose the Landau-gauge functions ϕ_{ap} as the basis set. The subscript p distinguishes between different states belonging to a continuously degenerate Landau level, and the label a is a binary index $a = (n_a, \sigma_a)$, which represents both LL index and spin index. We thus have $\phi_{ap}(\mathbf{r}, \sigma) = \delta_{\sigma, \sigma_a}(l_B L)^{-1/2} e^{ipy}\varphi_{n_a}(pl_B + x/l_B)$, where

$$\varphi_n(x) = (2^n n!\sqrt{\pi})^{-1/2} e^{-x^2/2} H_n(x) \tag{5}$$

[$H_n(x)$ is the Hermite polynomial]. In the following, we employ the notation a_p, b_p, … for the electron annihilation operator corresponding to the sublevel a, b, … and also use the intra-LL "displacement" operators $\mathcal{A}_\mathbf{q}^+$, $\mathcal{B}_\mathbf{q}^+$, …, where

$$\mathcal{A}_\mathbf{q}^+ = N_\phi^{-1}\sum_p e^{-iq_x p l_B^2} a^+_{p+\frac{q_y}{2}} a_{p-\frac{q_y}{2}}, \qquad \mathcal{B}_\mathbf{q}^+ = (a \longrightarrow b), \ldots \tag{6}$$

($\mathcal{A}_\mathbf{q}^+ = \mathcal{A}_{-\mathbf{q}}$). Considering the quantity χ as an annihilation operator in the Schrödinger representation, we can substitute Eq. (4) into $\langle\chi|\hat{\mathcal{H}}_{\text{imp}}|\chi\rangle$ to obtain the secondary quantized representation of the Hamiltonian $\mathcal{H}_{\text{imp}}$, namely,

$$\hat{\mathcal{H}}_{\text{imp}} \approx l_B^{-2}\sum_\mathbf{q} e^{-q^2 l_B^2/4}(W_\uparrow \mathcal{A}_\mathbf{q}^+ + W_\downarrow \mathcal{B}_\mathbf{q}^+). \tag{7}$$

Here, the sign of approximate equality means that we have omitted the terms corresponding to the LL mixing and have kept only those relevant to the projection onto the nth LL. Therefore, specifically, we have in Eq. (7) that the labels a and b correspond to the $a = (n, \uparrow)$ and $b = (n, \downarrow)$ sublevels. At $\nu = 2n + 1$, the "clean" ground state $|0\rangle$ is completely determined by the equations $\mathcal{A}_\mathbf{q}|0\rangle = \delta_{\mathbf{q}, 0}|0\rangle$ and $\mathcal{B}_\mathbf{q}|0\rangle = 0$, while an electron and a hole are defined as the

$$|f_e\rangle = \sum_p f_e(p) b_p^+|0\rangle, \quad |f_h\rangle = \sum_p f_h(p) a_p|0\rangle \tag{8}$$

states, respectively. Here, the envelope functions are normalized as $\sum_p |f_{e,h}|^2 = 1$.

Quasiparticle states (8) satisfy the "clean" equations $\hat{\mathcal{H}}_0|f_{e,h}\rangle = (E_0 + E_{e,h})|f_{e,h}\rangle$, where $E_e = \epsilon_Z$ and $E_h = E_C$. Here, E_C is the characteristic Coulomb energy: $E_C = \int e^{-q^2 l_B^2/2} V(\mathbf{q}) d\mathbf{q}$, where $2\pi V(\mathbf{q})$ is the 2D Fourier component of the averaged Coulomb potential (in the ideal 2D case, $V = e^2/\kappa q$ and $E_C = \sqrt{\pi/2}\, e^2/\kappa l_B$). To obtain this result, it is convenient to employ the expression for the Coulomb interaction Hamiltonian in terms of the excitonic representation (see, e.g., [8]) and the commutation rules

$$[\mathcal{A}_\mathbf{q}^+, a_p] \equiv -\frac{1}{N_\phi} e^{-iq_x l_B^2(p - q_y/2)} a_{p-q_y}, \qquad [\mathcal{B}_\mathbf{q}^+, b_p^+] \equiv \frac{1}{N_\phi} e^{-iq_x l_B^2(p + q_y/2)} b^+_{p-q_y} \tag{9}$$

and $[\mathcal{A}_\mathbf{q}^+, b_p^+] = [\mathcal{B}_\mathbf{q}^+, a_p] \equiv 0$.

First, we obtain the correction to the ground-state energy in the case of a single impurity. Substituting expression (7) for $\hat{\mathcal{H}}_{\text{imp}}$ into the equation $(\hat{\mathcal{H}}_0 + \hat{\mathcal{H}}_{\text{imp}})|0\rangle = (E_0 + \Delta E_0)|0\rangle$ (where $\hat{\mathcal{H}}_0$ is the "clean" QHF Hamiltonian including the *Zeeman and Coulomb interaction part*), we obtain the correction to the "clean" ground state: $\Delta E_0 = W_\uparrow/l_B^2$.

Finally, to calculate the bound electron state, we solve the equation $\hat{\mathcal{H}}_{\text{imp}}|f_e\rangle = E_e'|f_e\rangle$, which, with the help of Eqs. (7)–(9), is reduced to the integral equation

$$\frac{W_\downarrow}{l_B\sqrt{\pi}}\int_{-\infty}^{+\infty} ds\, f_e(s) e^{-(s^2 + p^2)l_B^2/2} = E_e' f(p). \tag{10}$$

The latter has the solution $f_e(p) = (\pi N_\phi)^{-1/4} e^{-p^2 l_B^2/2}$ at $E_e' = W_\downarrow/l_B^2$ ($(\pi N_\phi)^{-1/4}$ is the normalization factor). Hence, the electron binding energy is

$$E_b^{(e)} = -W_\downarrow/l_B^2. \tag{11}$$

Naturally, this state is realized if $W_\downarrow < 0$. Let us note that, in the leading approximation, the obtained $E_b^{(e)}$ value is equal to the binding energy in the single-electron problem [2]. In a similar way, we find that the equation $\hat{\mathcal{H}}_{\text{imp}}|f_h\rangle = E_h'|f_h\rangle$ has the solution $f_h(p) = (\pi N_\phi)^{-1/4} e^{-p^2 l_B^2/2}$ at $E_h' = -W_\uparrow/l_B^2$. Thus, the total energy of the $|f_h\rangle$ bound state is $E_0 + E_C$; i.e., it is the same as in the "clean" hole state. The bound energy of the hole is

$$E_b^{(h)} = W_\uparrow/l_B^2. \tag{12}$$

This state exists under the condition $W_\uparrow > 0$.

The physical meaning of the envelope functions $f_{e,h}$ obtained above becomes evident if we change the Lan-

dau gauge to the symmetric gauge. In the latter case, we have to change the vector potential $\mathbf{A} = (0, Bx, 0)$ to $\mathbf{A} = (-By/2, Bx/2, 0)$. Then, the single-electron states of the n's LL are described by the basis spatial function

$$\phi_{nm} = l_B^{-1}\left[\frac{n!}{2^{m+1}(m+n)!\pi}\right]^{1/2} \times (ir/l_B)^m L_n^m(r^2/2l_B^2)e^{-im\varphi - r^2/4l_B^2} \quad (n+m \geq 0), \tag{13}$$

where $\mathbf{r} = (r\cos\varphi, r\sin\varphi)$, L_n^m is the Laguerre polynomial, and m runs over N_ϕ integer numbers: $m = -n, 1-n, 2-n, \ldots, N_\phi - n - 1$. All these states now have the same cyclotron energy, and the Fermi creation and annihilation operators acquire the index m (instead of p in the Landau gauge). For example, one can find the expression for the old Landau gauge operator a_p in terms of the new operators a_m:

$$a_p = N_\phi^{-1/2}\sum_{m=0}^{\mathcal{N}-1} i^{m-n}\varphi_m(pl_B)a_{m-n} \tag{14}$$

where φ_m is oscillatory function (5). Now, if we substitute this expression (and the analogous one for b_p^+) into Eqs. (8) with the above functions, we obtain that only the $m = 0$ harmonic of Eq. (13) contributes to the $|f_{e,h}\rangle$ bound states. Indeed, the summation over p in expansion (8) turns out to be proportional to the integral $\int_{-\infty}^{\infty} e^{-p^2} H_m(p)$. The latter vanishes at any m except for $m = 0$. Certainly, this feature reflects the well-known fact that the point-impurity Hamiltonian is diagonal exactly in symmetric basis (13). Besides, only the zero (axially symmetric) harmonic contributes to the bound-state energy calculated within the single LL approximation.

3. To study a bound skyrmionic excitation, we present it in accordance with [7, 8] as a smooth rotation in the 3D spin space:

$$\boldsymbol{\psi}(\mathbf{r}) = \hat{U}(\mathbf{r})\boldsymbol{\chi}(\mathbf{r}), \quad \mathbf{r} = (x, y). \tag{15}$$

Here, $\boldsymbol{\psi}$ is a spinor given in the stationary coordinate system and $\boldsymbol{\chi}$ is a new spinor in the local coordinate system following this rotation. The rotation matrix $\hat{U}(\mathbf{r})$ ($\hat{U}^\dagger\hat{U} = 1$) is parameterized by three Eulerian angles [11]:

$$\hat{U} = \begin{pmatrix} \cos\frac{\theta}{2}e^{-i(\varphi+\eta)/2} & \sin\frac{\theta}{2}e^{i(\eta-\varphi)/2} \\ -\sin\frac{\theta}{2}e^{i(\varphi-\eta)/2} & \cos\frac{\theta}{2}e^{i(\varphi+\eta)/2} \end{pmatrix}. \tag{16}$$

These angles $\theta(\mathbf{r})$, $\varphi(\mathbf{r})$, and $\eta(\mathbf{r})$ present continuum field functions. The skyrmion state is thus determined by the continuum matrix $\hat{U}(\mathbf{r})$ and by the local quantum state $\boldsymbol{\chi}$ determined in terms of small gradient ($l_B\nabla\hat{U}$) corrections to the local QHF, where all electron spins are parallel $\left[\boldsymbol{\chi} \propto \begin{pmatrix} 1 \\ 0 \end{pmatrix}\right]$.

The solution may be found from the reformulated variational principle. Namely, we divide the 2DEG area into a large number G_i of domains that are much smaller than the total 2DEG area but that still remain much larger than the magnetic flux quantum area $2\pi l_B^2$. The energy of excitations of this type may be found through the minimization procedure in the following way:

$$E = \min_U\left[\sum_i \min_\psi\left(\frac{\langle\psi|H_i|\psi\rangle_{G_i}}{\langle\psi|\psi\rangle_{G_i}}\right)\right]. \tag{17}$$

Here, averaging is performed over the domain G_i. All the G_i areas add up to the total 2DEG area. H_i is the Hamiltonian corresponding to the G_i domain. The state $|\psi\rangle$ presents here a many-electron quantum state built by single electron spinors (15). Thus, the state $|\psi\rangle$ is parametrized by $\hat{U}$ and by the derivatives of $\hat{U}$ (generally, up to any order) considered as external parameters for every G_i. The procedure of the inner minimization in Eq. (17) is equivalent to the solution of the Schrödinger equation within the area $\Delta x\Delta y = G_i$.

In our case, the local Hamiltonians are the same as in the clean case, except for the Hamiltonian $H_{i=0}$ corresponding to the one domain G_0 that involves the point impurity. Procedure of minimization (17) only differs from the clean case by the addition of the energy

$$\Delta E_{\text{imp}}^{(U)} = \frac{\langle\chi|\hat{U}^+\hat{H}_{\text{imp}}\hat{U}|\chi\rangle_{G_i}}{\langle\chi|\chi\rangle_{G_i}} \tag{18}$$

to the sum within the square brackets in Eq. (17). Here, we have used Eq. (15) and should then substitute

$$\hat{U}^+\hat{H}_{\text{imp}}\hat{U} = \begin{pmatrix} W + \frac{D}{2}\cos\theta & -\frac{D}{2}\sin\theta e^{-i\varphi} \\ -\frac{D}{2}\sin\theta e^{i\varphi} & W - \frac{D}{2}\cos\theta \end{pmatrix}\delta(\mathbf{r}) \tag{19}$$

into Eq. (18). (We have set $\eta = \varphi$ without any loss of generality.) Under conditions (2), (3), it is sufficient to use as $|\chi\rangle$ the unperturbed QHF state determined in the local coordinate system of domain G_0. That is, in our case, $|\chi\rangle = \hat{\boldsymbol{\chi}}^+|0\rangle$, where $\hat{\boldsymbol{\chi}}$ is the annihilation operator. If we again employ the expansion of Eq. (4), then, with the help of the equation

$$\hat{\mathcal{H}}_{\text{imp}} = \int\limits_{\text{over}\,G_0} d\mathbf{r}\hat{\boldsymbol{\chi}}^+\hat{U}^+\hat{H}_{\text{imp}}\hat{U}\hat{\boldsymbol{\chi}}, \tag{20}$$

we can obtain the impurity Hamiltonian in terms of the secondary quantized representation. We will study only the $\nu = 1$ case. Substituting Eqs. (19) and (4) into Eq. (20) and assuming that $a = (0, \uparrow)$ and $b = (0, \downarrow)$, we find, within the single LL approximation,

$$\hat{\mathcal{H}}_{\text{imp}} = l_B^{-2}\sum_{\mathbf{q}} e^{-q^2 l_B^2/4}$$

$$\times\left[\left(W + \frac{D}{2}\cos\theta_0\right)\mathcal{A}_{\mathbf{q}}^{+} + \left(W - \frac{D}{2}\cos\theta_0\right)\mathcal{B}_{\mathbf{q}}^{+}\right. \quad (21)$$

$$\left. - \frac{D}{2}\sin\theta_0 e^{-i\varphi_0} N_\phi^{-1/2}\mathcal{Q}_{\mathbf{q}} - \frac{D}{2}\sin\theta_0 e^{i\varphi_0} N_\phi^{-1/2}\mathcal{Q}_{\mathbf{q}}^{+}\right].$$

The definitions of the operators $\mathcal{A}_{\mathbf{q}}^{+}$ and $\mathcal{B}_{\mathbf{q}}^{+}$ are identical to those given by Eq. (6), with the number of magnetic flux quanta $N_\phi = \Delta x \Delta y/2\pi l_B^2$ being nonzero only for the domain G_0. The notation of the spin-exciton creation $\mathcal{Q}_{\mathbf{q}}^{+} = N_\phi^{-1/2}\sum_p e^{-iq_x p l_B^2} b^{+}_{p+\frac{q_y}{2}} a_{p-\frac{q_y}{2}}$ and annihilation $\mathcal{Q}_{\mathbf{q}} = (\mathcal{Q}_{\mathbf{q}}^{+})^{+}$ operators have also been used in Eq. (21). θ_0 and φ_0 are the Hermitian angles (determined by the given $\hat{U}$ matrix) corresponding to the domain G_0. Now, in accordance with Eq. (18), we get

$$\Delta E_{\text{imp}}^{(U)} = \langle 0|\hat{\mathcal{H}}_{\text{imp}}|0\rangle = \left(W + \frac{D}{2}\cos\theta_0\right)/l_B^2. \quad (22)$$

(Only the $\sim\mathcal{A}_0^{+}$ term contributes to this result.)

The outer minimization in Eq. (17) is thereby presented as $\min_U(E_U + \Delta E_{\text{imp}}^{(U)})$, where E_U is the "clean" energy obtained for a given function $\hat{U}(\mathbf{r})$ after summation over all G_i in Eq. (17). Meanwhile, the minimization of E_U and $\Delta E_{\text{imp}}^{(U)}$ may be fulfilled independently. Indeed, the clean skyrmion state is degenerate; it has an energy that does not depend on the "skyrmion center" position. The latter is the point of the total 2DEG area where $\theta = \pi$; i.e., the local electron spins are aligned in the direction opposite to the direction at infinity (where $\theta = 0$). In contrast to this, the energy $\Delta E_{\text{imp}}^{(U)}$ depends only on the relative positions of the impurity site (the $\mathbf{r} = 0$ point in our coordinate system) and the skyrmion center site. Thus, the impurity lifts the degeneracy, and, hence, by varying the position of the skyrmion center site, we find that $\min_U[\Delta E_{\text{imp}}^{(U)}] = (W - |D|/2)/l_B^2$. If $D < 0$, this value is reached at $\theta_0 = 0$; i.e., the skyrmion center is located at the infinity. Evidently, in this case, the skyrmion does not form a bound state. At $D > 0$, the minimum energy is realized for $\theta_0 = \pi$, i.e., where the impurity site and the skyrmion center coincide (of course, to within a length smaller than the characteristic skyrmion radius R^* but perhaps larger than l_B). This means that the bound skyrmion state takes place. The binding energy should be obtained by subtraction of the minimum energy from the $\theta_0 = 0$ energy $(W + D/2)l_B^2$, i.e.,

$$E_b^{\text{sk}} = D/l_B^2. \quad (23)$$

Thus, in the adopted approximation, only the magnetic impurity with $D > 0$ captures the skyrmion (cf. [9], where a similar result is obtained in the case of the bound spin exciton). It is worth noting that result (23) does not depend on the skyrmion charge [12]: electron-like and hole-like skyrmions have the same bound energy (23).

An analysis reveals that the charge dependence arises only in the second-order approximation in terms of $l_B\nabla$; it is determined by the relative correction $(l_B/R^*)^2$. This can be easily found by means of the renormalization procedure for the magnetic length $l_B \longrightarrow \tilde{l}_B$. Indeed, the effective local magnetic length is determined by the effective magnetic field, including the additional part proportional to the second-order spatial derivatives of the field $\hat{U}$ [8]:

$$\frac{1}{\tilde{l}_B^2} = \frac{1}{l_B^2} + \nabla\times\mathbf{\Omega}^z. \quad (24)$$

Here,

$$\mathbf{\Omega}^z = \frac{1}{2}(1 + \cos\theta)\nabla\varphi \quad (25)$$

(see [7, 8]), and l_B is the magnetic length at infinity (far from the skyrmion center). Let us assume that the impurity is nonmagnetic, i.e., that $D = 0$. The binding energy (if the bound state were to be realized) should be determined exactly by the desired correction. We substitute for the angles Eqs. (24) and (25) their expressions in terms of functions of $\mathbf{r}$ [13]:

$$\cos\theta = \frac{R^{*2} - r^2}{R^{*2} + r^2}, \quad \varphi = -q\arctan(y/x)$$

(where $q = \pm$ is the skyrmion charge). Eventually, by comparing the skyrmion energy at $\mathbf{r} = 0$ with the energy at infinity, we find the impurity correction: $\Delta E_{\text{imp}} = W\nabla\times\mathbf{\Omega}^z|_{\mathbf{r}=0} = 2qW/R^{*2}$. The binding energy is thus

$$E_b^{\text{sk}} = -2qW/R^{*2} \text{ if } D = 0.$$

Therefore, the bound electron/hole-like skyrmion arises when W is positive/negative.

In reality, the concentration of point impurities in the 2D channel can be considerable. It seems to have the values at which the mean distance between impurities is shorter than the effective skyrmion radius (the

latter is determined by the small but still nonzero Zeeman gap ϵ_Z^*). In this case, the impurity contribution to the total energy is equal to $\int d\mathbf{r}\lambda l_B^{-2}\left[W + \frac{D}{2}\cos\theta(\mathbf{r})\right]$, where $\lambda(\mathbf{r})$ is the concentration of impurities. It also involves the correction to the ground-state energy $l_B^{-2}\left(W + \frac{D}{2}\right)\int d\mathbf{r}\lambda$, which should be subtracted. The impurity correction to the proper skyrmion energy is thereby

$$\Delta E_{\text{imp}}^{\text{sk}} = \frac{D}{2l_B^2}\int[\cos\theta(\mathbf{r}) - 1]\lambda d\mathbf{r}.$$

If we compare this value with the skyrmion Zeeman energy

$$\frac{\epsilon_Z^*}{2}\int(1 - \cos\theta)d\mathbf{r}/2\pi l_B^2,$$

it becomes evident that the magnetic impurities dispersed in the 2D channel lead to a correction to the Zeeman gap:

$$\epsilon_Z^* \longrightarrow \epsilon_Z^* - 2\pi\lambda D$$

(assuming a homogeneous concentration λ). Due to the supposed smallness of ϵ_Z^*, this can be substantial. Under certain conditions, it could change the sign of the effective *g* factor in the 2DEG.

I acknowledge support from the Russian Foundation for Basic Research and thank V. Fleurov, S.V. Iordanskii, and K. Kikoin for useful discussions.

REFERENCES

1. T. Ando, A. B. Fowler, and F. Stern, Rev. Mod. Phys. **54**, 437 (1982).
2. Y. Avishai, M. Ya. Azbel, and S. A. Gredeskul, Phys. Rev. B **48**, 17 280 (1993).
3. J. J. Palacios, D. Yoshioka, and A. H. MacDonald, Phys. Rev. B **54**, R2296 (1996).
4. S. L. Sondhi, A. Karlhede, S. A. Kivelson, and E. H. Rezayi, Phys. Rev. B **47**, 16 419 (1993).
5. H. A. Fertig, L. Brey, R. Côté, and A. H. MacDonald, Phys. Rev. B **50**, 11018 (1994).
6. Yu. A. Bychkov, T. Maniv, and I. D. Vagner, Phys. Rev. B **53**, 10148 (1996).
7. S. V. Iordanskii, S. G. Plyasunov, and V. I. Falko, Zh. Éksp. Teor. Fiz. **115**, 716 (1999) [JETP **88**, 392 (1999)].
8. S. M. Dickmann, Phys. Rev. B **65**, 195310 (2002).
9. V. Fleurov and K. Kikoin, Low Temp. Phys. **27**, 1083 (2001).
10. P. Dahan, V. Fleurov, K. Kikoin, and I. D. Vagner, Phys. Rev. B **65**, 165313 (2002).
11. L. D. Landau and E. M. Lifshitz, *Course of Theoretical Physics*, Vol. 3: *Quantum Mechanics: Non-Relativistic Theory*, 4th ed. (Nauka, Moscow, 1989; Butterworth, Oxford, 1991).
12. The skyrmion electric charge is equal to the so-called topological charge. We do not distinguish these two meanings here.
13. A. A. Belavin and A. M. Polyakov, Pis'ma Zh. Éksp. Teor. Fiz. **22**, 503 (1975) [JETP Lett. **22**, 245 (1975)]; R. Rajaraman, *Solitons and Instantons: An Introduction to Solitons and Instantons in Quantum Field Theory* (North-Holland, Amsterdam, 1982; Mir, Moscow, 1985).

JETP Letters, Vol. 81, No. 3, 2005, pp. 117–121. Translated from Pis'ma v Zhurnal Éksperimental'noĭ i Teoreticheskoĭ Fiziki, Vol. 81, No. 3, 2005, pp. 149–153.

Instability of the Distribution of Atomic Steps on Si(111) upon Submonolayer Gold Adsorption at High Temperatures

S. S. Kosolobov[1], S. A. Song[2], L. I. Fedina[1], A. K. Gutakovskiĭ[1], and A. V. Latyshev[1,3]

[1] *Institute of Semiconductor Physics, Siberian Division, Russian Academy of Sciences, Novosibirsk, 630090 Russia*
e-mail: kosolobov@thermo.isp.nsc.ru

[2] *Samsung Advanced Institute of Technology, P.O. Box 111 Suwon, 440-600, Korea*

[3] *Novosibirsk State University, Novosibirsk, 630090 Russia*

Received December 21, 2004

The gold adsorption effect on the distribution of monatomic steps on the (111) silicon surface is studied *in situ* by ultrahigh vacuum reflection electron microscopy at temperatures of 850–1260°C. A new effect of the instability of silicon surface morphology has been detected. This effect leads to the redistribution of regular steps (RSs) to step bunches (STs) and vice versa on a surface covered with a gold submonolayer. For the crystal heated by directly passing an electric current, the behavior of the RS ⇔ SB morphological transitions on the silicon surface is investigated as a function of the gold coverage and the direction of the heating current. Thus, isothermal annealing at 900°C is accompanied by the following transitions on the silicon surface with predeposited 0.75 monolayer gold coverage: RS (0.72) ⇒ SB (0.42) ⇒ RS (0.24) ⇒ SB (0.07) RS ⇒ (0). The numbers given in parentheses are estimated values of the critical gold coverage measured in the monolayers at which the morphological transitions are observed. A change in the direction of the electric current used to heat the crystal leads to the reversible changes RS ⇒ SB and SB ⇒ RS at the same values of the critical gold coverage.

PACS numbers: 68.37.–d, 68.43.Jk, 68.47.Fg

The morphology of vicinal crystal surfaces is mainly determined by the distribution of atomic steps. The initial uniform distribution of atomic steps can be unstable and can transform into regions with high and low densities of atomic steps, for example, in the processes of sublimation [1, 2], thermal annealing [3], epitaxial growth [4], phase transitions [5], and the formation of a clean surface [6]. The physical mechanisms underlying the redistribution of atomic steps on crystal surfaces are being studied intensively, because an understanding of them will allow the surface morphology and the interface to be controllably regulated.

It is important to elucidate the effect of foreign atoms changing the crystal surface properties (such as the activation energy of adatom migration, the incorporation and detachment energies of atoms, etc.) on the stability of the distribution of atomic steps on the surface. An example is surfactant epitaxy, at which epitaxial growth mechanisms are changed under the action of surfactants [7]. Another example of the instability of atomic steps on the (111) silicon surface during sublimation is the formation of step bunches under the action of a direct electric current used for the resistive heating of the crystal [8]. Depending on the direction of the electric current heating the crystal, either a system of regularly arranged atomic steps (RSs) or a system of step bunches (SBs) is formed on the surface at temperatures above 850°C. The aforementioned points to the necessity of studying structural rearrangements on the silicon surface under conditions of simultaneous adsorption of surfactants and electromigration. Their effect is pronounced in the case of significant mass transfer on the crystal surface, that is, at high temperatures.

In contrast to other investigations, this work deals with the surfactant effect on the distribution of atomic steps on the silicon (111) surface at temperatures above 850°C. In other words, the behavior of monatomic steps is analyzed in the case of sublimation on the silicon surface containing an adsorption layer of impurity atoms (surfactants) of less than one monolayer (ML). Gold was selected as the impurity modifying the silicon surface properties. First, the structural and electronic properties of the gold–silicon system are well understood. Second, gold is a surfactant for silicon in homo- and heteroepitaxial growth [9]. Third, gold is characterized by a relatively high melting point in comparison with other surfactants such as antimony, tin, indium, and others, which suggests that the lifetime of gold atoms adsorbed on the silicon surface at temperatures higher than 850°C is longer.

0021-3640/05/8103-0117$26.00 © 2005 Pleiades Publishing, Inc.

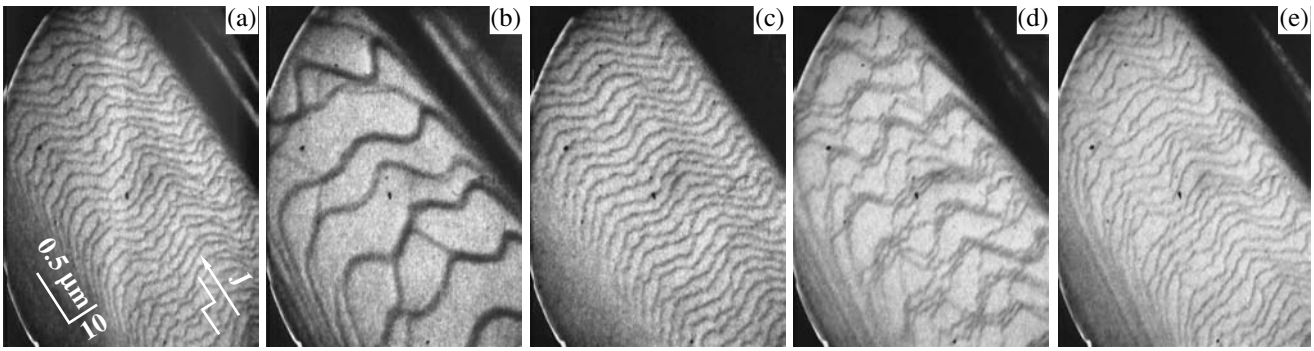

Fig. 1. REM images of the Si(111) surface area (a) after the deposition of ~0.75 ML gold and (b), (c), (d), and (e) upon subsequent thermal annealing at 900°C for 4, 20, 43, and 50 min, respectively. The arrow shows the electric current direction.

Experimental studies of morphological rearrangements on the silicon (111) surface caused by the adsorption of gold atoms were performed *in situ* by ultrahigh vacuum reflection electron microscopy (UHV-REM) [10]. Samples $10 \times 2 \times 0.5$ mm in size were cut from a standard silicon wafer in such a way that atomic steps were perpendicular to the long side of the sample. After a standard procedure of chemical cleaning, the silicon sample was fixed in a tantalum holder and was transferred to the UHV chamber of a microscope. The further cleaning of the substrate was performed by high-temperature annealing in an ultrahigh vacuum. The heating of the sample was carried out by passing an electric current through the sample.

The thermal annealing of the sample in the ultrahigh vacuum chamber at a temperature of ~1280°C for several minutes led to the removal of the natural oxide layer and impurities. The disappearance of the additional reflections in the microdiffraction pattern corresponding to silicon carbide particles and the occurrence of the reversible superstructural $(7 \times 7) \Leftrightarrow (1 \times 1)$ phase transition, which proceeds on atomically clean silicon (111) surfaces at a temperature of 830°C [10], indicated that the degree of surface cleaning was sufficiently high. After thermal annealing, regular atomic steps one interplanar spacing (3.1 Å) in height were observed in the REM image of the silicon surface as thin dark lines spaced by 100 nm on the average (Fig. 1a). The absence of pinning centers for the motion of atomic steps in the process of sublimation additionally indicated that the degree of surface cleaning from impurities was high.

In the process of sublimation, it was observed that the steps moved in the direction toward higher situated terraces as a result of the detachment of atoms from step kinks and their desorption from a terrace. The rate of step movement depended on the mean distance between them and the crystal temperature [11]. In accordance with [8], it was observed that the system of monatomic steps was unstable with respect to fluctuations of the distance between them, which led to the formation of step bunches. The RS $\Leftrightarrow$ SB transition was reversible upon a change in the polarity of the applied voltage required for the Joule heating of the crystal. Thus, the system of regular steps was stable at a temperature of 900°C and heating with a direct current directed toward higher situated terraces, and the formation of step bunches whose width and the distance between which increased over the annealing time was observed upon a change in the current direction.

The deposition of gold atoms on the silicon surface was carried out from a small-volume evaporator representing a crucible of a tungsten wire through which an electric current was passed. The amount of gold deposited on the surface was determined from the product of the deposition rate by the deposition time. The deposition rate of gold atoms was precisely determined by the time it took to fill the entire surface with the Si(111)–(5×2)Au superstructure at a substrate temperature of 500°C, which corresponded to a 0.42-ML gold coverage [12]. Note that the adsorption of metals on the silicon surface can initiate surface reconstruction [13, 14] or facet formation [15, 16]. For this reason, the temperature and the amount of the adsorbed gold in the experimental studies were selected so that the effects of faceting or reconstruction initiated by the deposited gold were not observed. The surface infilling degree by superstructural domains was monitored by their direct visualization in an electron microscope. The superstructure type was identified by microdiffraction patterns obtained from the chosen surface area.

Consider the behavior of monatomic steps upon gold adsorption at a temperature of 900°C under conditions of heating with a direct current directed toward upper terraces. Under these conditions, atomic steps retained a regular distribution for a long time, for example, several hours. A typical sequence of REM images of the same silicon surface area selected from fragments of video recording during gold deposition and the subsequent thermal annealing is shown in Fig. 1. After the deposition of ~0.75 ML gold on the silicon surface, the heating of the gold source was switched off and the crystal was isothermally annealed at 900°C. In

the process of gold deposition, the intensity of the main diffraction reflections decreased. However, the occurrence of additional reflections pointing to a change in surface reconstruction was not observed at a given temperature, in agreement with the phase diagrams of superstructural reconstructions upon gold adsorption [17, 18]. A substantial change in the shape of steps or their distribution in comparison with the initial surface was not detected in the REM images (Fig. 1a). Taking into account that the surface before and after gold deposition was completely identical, the REM image of the (111) silicon surface immediately after gold deposition is not shown in Fig. 1. The amount of deposited gold, ~0.75 ML, was selected from the condition of a maximum coverage at which three-dimensional gold islands did not form at a given temperature.

To prove the existence of gold deposited on the surface (which could fully dissolve in the substrate crystal bulk or re-evaporate), the substrate temperature was sharply decreased to 500°C immediately after adsorption. At this temperature, a Si(111)–($\sqrt{3} \times \sqrt{3}$)Au superstructure formed on the surface. This superstructure covered the entire surface (5×200 μm in size) visualized in REM. The formation of superstructure ($\sqrt{3} \times \sqrt{3}$) domains at this temperature started when the gold coverage of the silicon surface was larger than 0.68 ML [12]. The occurrence of this superstructure indicated that ~0.7 ML gold was retained on the silicon surface despite the high substrate temperature (900°C). At a lower amount of gold, a partial coverage of the surface with the ($\sqrt{3} \times \sqrt{3}$) superstructure was observed at 500°C.

Despite the occurrence of ~0.7 ML gold on the surface, the distribution of steps was not changed immediately after deposition. However, in the process of thermal annealing at a temperature of 900°C, the surface concentration of gold decreased because of its partial dissolution the crystal bulk or desorption. After 4-min annealing, it was observed that atomic steps on the silicon surface were redistributed by means of the formation of surface areas with an increased density of atomic steps (bunches) and broad (≈0.5 μm and, in some cases, to several micrometers) singular terraces (Fig. 1b).

Note that the formation of step bunches on the silicon surface with an adsorbate of gold differed from the formation of bunches during sublimation initiated by electromigration [8]. In the first case, the rearrangement of steps proceeded because of a change in the relative velocities of steps moving toward overlying terraces. In the second case, bunches formed through the movement of some atomic steps toward overlying terraces (generation of adatoms by a step), whereas other steps moved in the opposite direction (incorporation of adatoms into a step). Moreover, some fragments of the same monatomic step could move in both the direction corresponding to the process of sublimation and the direction corresponding to epitaxial growth, forming bridges between neighboring bunches. This behavior of steps can be explained by changes in the incorporation or generation coefficient of silicon atoms upon gold adsorption on steps. However, an analysis of the diffraction contrast of electron-microscope images did not reveal features associated with a change in the local deformation of a step that would give evidence of the incorporation of gold atoms into the step edge [19].

The morphology of the silicon surface with bunches changed, and the system of train steps again transformed into a system of regular steps. An image of the same silicon surface area after 16-min annealing at 900°C is given in Fig. 1c. The decomposition of bunches was accompanied by the movement of steps in both the direction of higher situated terraces and the opposite direction. This observation allows the conclusion to be made that the surface contains an increased density of silicon adatoms, which initiates the displacement of a step toward lower terraces. A possible source of the excessive density of silicon adatoms on the surface can be the generation of interstitial silicon atoms in the subsurface layer during the diffusion of gold atoms from the surface to the silicon bulk. It is known that the diffusion of gold into silicon proceeds through the mechanism of gold substitution at a silicon site position. This must lead to the generation of interstitial atoms in the subsurface region, which can also go out to the surface [20].

To estimate the density of gold atoms on the surface, the crystal temperature was decreased to 500°C. In this case, additional reflections corresponding to a superstructure Si(111)–(5×2)Au reconstruction were detected in the diffraction pattern, whereas the reflections from the ($\sqrt{3} \times \sqrt{3}$) superstructure were absent. In accordance with the phase diagram, this indicated that the gold coverage decreased down to ~0.44 ML.

The subsequent isothermal annealing at a temperature of 900°C again led to a change in the character of the distribution of atomic steps. Within 40 min after the source of gold was switched off, step bunches again formed on the surface (Fig. 1d). It should be noted that the mechanisms of train formation on the clean surface and on the surface with adsorbed gold were completely identical, which was in agreement with the results obtained in [21] for the adsorption of less than 0.005 ML gold. As the crystal temperature decreased to room temperature, no additional reflections due to gold deposition were observed in the diffraction pattern except for the reflections from the (7×7) superstructure.

Finally, the formation of regularly arranged steps, characteristic of the atomically clean silicon surface (Fig. 1a), was detected at the given temperature after 47-min annealing of the crystal (Fig. 1e). Additional

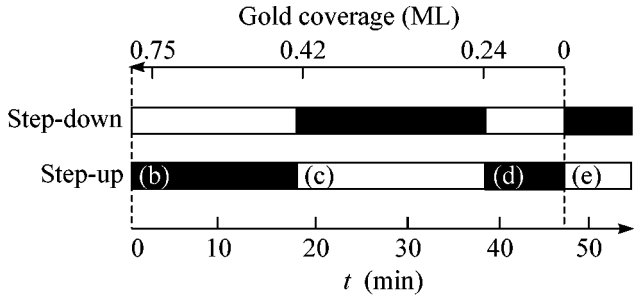

Fig. 2. Schematic diagram of morphological transitions initiated by gold on the Si(111) surface in the process of annealing at 900°C: bunches (black field) ⇔ regular steps (white field). The current is directed toward the upper (lower panel) and lower (upper panel) terraces, respectively.

annealing for several hours did not reveal a change in the distribution of steps. This allows the conclusion to be made that the 0.7 ML gold adsorbed on the silicon surface was completely dissolved in the crystal bulk or evaporated during thermal annealing at 900°C in approximately 47 min.

Based on the facts presented above, estimates were obtained for the critical concentrations of gold adatoms on the silicon surface at which a change in the surface morphology occurs. At a temperature of 900°C, these concentrations were 0.42 (Fig. 1b), 0.24 (Fig. 1c), and 0.07 ML (Fig. 1d), respectively, as shown schematically in the lower panel of Fig. 2. The variation of the crystal temperature in the deposition and thermal annealing of the substrata crystal led to a change in the critical concentrations for the transformations of the surface morphology, though the sequence of transformations shown at 900°C were retained. The behavior of monatomic steps observed down to 1260°C was qualitatively similar.

It was found that the behavior of monatomic steps on the (111) silicon surface in the presence of adsorbed gold atoms depends on the direction of the heating electric current (Fig. 2). The morphological RS ⇔ SB transitions reversibly changed upon a change in the direction of the electric current. It should be noted that several temperature intervals in which RS ⇔ SB transitions were observed were also found on the clean silicon surface. The physical nature of such transitions was not determined unambiguously. It was related to the occurrence of an effective charge on silicon adatoms [22]. The drift of adatoms in the applied electric field upon heating the crystal changes the flux of atoms on a step from the upper and lower terraces, which can result in the kinetic instability of the uniform distribution of steps [23]. To explain the morphological transitions observed on the surface in the presence of adsorbed gold atoms, it should be suggested that the effective charge of adatoms changes, as its sign depends on the density of gold adatoms [24]. At present, the physical reasons for the change in the effective charge of adatoms are not clear and additional experimental and theoretical investigations are necessary.

In this work, the effect of gold adsorption on the silicon surface morphology was comprehensively studied *in situ* by the UHV-REM technique in the temperature range 850–1260°C. It was found that the morphology of the stepped silicon (111) surface changed periodically in the process of the thermal annealing of the substrate crystal with preadsorbed gold in an amount of less than one monolayer. Two types of morphology formed, depending on the gold coverage of the surface: regularly arranged atomic steps or bunches of atomic steps. A change in the surface morphology occurred at gold-coverage values of 0.42, 0.24, and 0.07 ML. The electromigration effect was observed upon a change in the polarity of the applied electric current heating the crystal under study. This effect changed the surface relief.

This work was supported in part by the Russian Foundation for Basic Research, project no. 04-02-16693, and by the Ministry of Education and Science of the Russian Federation. The work of A.V.L. was supported by the Public Charity Foundation for the Support of National Science.

REFERENCES

1. L. V. Litvin, A. B. Krasilnikov, and A. V. Latyshev, Surf. Sci. Lett. **244**, L121 (1991).
2. K. Yagi, H. Minoda, and M. Degawa, Surf. Sci. Rep. **43**, 45 (2001).
3. H.-C. Jeong and E. D. Williams, Surf. Sci. Rep. **34**, 171 (1999).
4. C. Schelling, G. Springholz, and F. Schaffler, Phys. Rev. Lett. **83**, 995 (1999).
5. A. B. Krasilnikov, A. V. Latyshev, and A. L. Aseev, Surf. Sci. **290**, 232 (1993).
6. B. S. Swartzentruber, Y.-W. Mo, M. B. Webb, and M. G. Lagally, J. Vac. Sci. Technol. A **7**, 2901 (1989).
7. M. Copel, M. C. Reuter, E. Kaxiras, and R. M. Tromp, Phys. Rev. Lett. **63**, 632 (1989).
8. A. V. Latyshev, A. L. Aseev, A. B. Krasilnikov, and S. I. Stenin, Surf. Sci. **213**, 157 (1989).
9. H. Minoda and K. Yagi, Ultramicroscopy **48**, 371 (1993).
10. A. V. Latyshev, A. B. Krasilnikov, and A. L. Aseev, Microsc. Res. Tech. **20**, 341 (1992).
11. A. V. Latyshev, A. L. Aseev, A. B. Krasilnikov, and S. I. Stenin, Surf. Sci. **227**, 24 (1990).
12. D. Grozea, E. Bengu, and L. D. Marks, Surf. Sci. **461**, 23 (2000).
13. C. Seifert, R. Hild, M. Horn-von-Hoegen, *et al.*, Surf. Sci. **488**, 233 (2001).
14. T. Nagao, S. Hasegawa, K. Tsuchiem, *et al.*, Phys. Rev. B **57**, 10100 (1998).

15. M. Horn-von-Hoegen, F.-J. Meyer zu Heringdorf, R. Hild, *et al.*, Surf. Sci. **433**, 475 (1999).
16. K. Aoki, H. Minoda, Y. Tanishiro, and K. Yagi, Surf. Rev. Lett. **5**, 653 (1998).
17. W. Swiech, E. Bauer, and M. Mundschau, Surf. Sci. **253**, 283 (1991).
18. T. Kamino, T. Yaguchi, M. Tomita, and H. Saka, Philos. Mag. A **75**, 105 (1997).
19. A. V. Latyshev, D. A. Nasimov, V. N. Savenko, and A. L. Aseev, Thin Solid Films **367**, 142 (2000).
20. U. Goesele, W. Grank, and A. Seeger, Appl. Phys. **23**, 361 (1980).
21. A. V. Latyshev, H. Minoda, Y. Tanishiro, and K. Yagi, Surf. Sci. **401**, 22 (1998).
22. S. Stoyanov, J. J. Metois, and V. Tonchev, Surf. Sci. **465**, 227 (2000).
23. R. L. Schwoebel and E. J. Shipsey, J. Appl. Phys. **37**, 3682 (1966).
24. A. V. Latyshev, H. Minoda, Y. Tanishiro, and K. Yagi, Appl. Surf. Sci. **130–132**, 60 (1998).

Translated by A. Bagatur'yants

JETP Letters, Vol. 81, No. 3, 2005, pp. 122–124. Translated from Pis'ma v Zhurnal Éksperimental'noĭ i Teoreticheskoĭ Fiziki, Vol. 81, No. 3, 2005, pp. 154–156.

Short-Range Order in Irradiated Diamonds

S. S. Agafonov, V. P. Glazkov, V. A. Nikolaenko, and V. A. Somenkov

Russian Research Center Kurchatov Institute, pl. Kurchatova 1, Moscow, 123182 Russia

e-mail: somenkov@isssph.kiae.ru

Received December 22, 2004

Using the neutron-diffraction method, it has been established that, when density in irradiated diamonds varies, a transition from a diamond-like amorphous structure to a graphite-like structure occurs. The transition occurs at a density $\rho \approx 2.7$–2.9 g/cm^3 and is accompanied by a sharp change in resistivity. *© 2005 Pleiades Publishing, Inc.*

PACS numbers: 61.43.Er, 61.82.–d

Investigation of structural changes and phase transitions that occur in glasses and fluids upon changing volume is of great current interest [1]. These changes have been observed in various systems, such as GeO_2, SiO_2, H_2O, etc. [2–8]. They are manifested as a change in the radial distribution function due to high pressures and are associated with an increase in the coordination number in the first coordination spheres (from four to six in GeO_2) in systems where it is small. A similar phenomenon, which is manifested in the existence of different structural forms of a disordered state and is called polyamorphism, can be expected for other methods of volume change, in particular, upon the irradiation of crystals after its radiation amorphization. An increase in volume upon reactor irradiation is large and can reach several tens of percent for sufficiently high neutron fluences [9], which is equivalent to a "negative" pressure of several tens or even hundred of gigapascals.

In light of this circumstance, the aim of this work is to apply the neutron diffraction method in order to determine which structural changes occur in an irradiated diamond upon density change. As samples, we used natural-diamond powders with a mean particle size 14–20 μm to 0.5 mm that are irradiated in a beryllium block of an MR reactor, which is cooled in running water, up to a fluence of 1.51×10^{21} (175 days in a neutron flux of about 10^{14} cm^{-2} s^{-1} with energies higher than 0.18 MeV). The irradiated powders turned out to be strongly density inhomogeneous and were divided into ten fractions in Clerici solution with distilled water in the density range from 3.24 to 2.05 g/cm^3 (with an accuracy of no worse than 2%) [10]. The diffraction experiments were carried out with a DISK diffractometer [11] at the 4.5-MW IR-8 reactor. The wavelength of monochromatic neutrons was equal to 1.667 Å. Samples of various fractions with masses 50–100 mg were investigated [12].

According to the results presented in Fig. 1, as density decreases, the diffraction lines of diamond are broadened, the "tails" of diffraction lines overlap, and a "halo" corresponding to the formation of a fine-crystalline ("amorphous") material of the diamond-like type is formed. With a further decrease in density, the diffraction pattern exhibits a new halo, whose intensity increases gradually and whose position corresponds to the position of the first maximum on the defect pattern of irradiated graphite [13] or amorphous carbon (activated charcoal) (Fig. 2a). The absence of small-angle scattering (for $q > 2 \times 10^{-2}$) from all samples indicates that they are homogeneous in scales of 2–3 nm. The results can be treated as evidence of a polyamorphic transition from diamond-like to graphite-like glass, which occurs when density decreases and which is likely associated with a decrease in the number of nearest neighbors in the first coordination sphere from four to three (in contrast to its increase at high pressures).

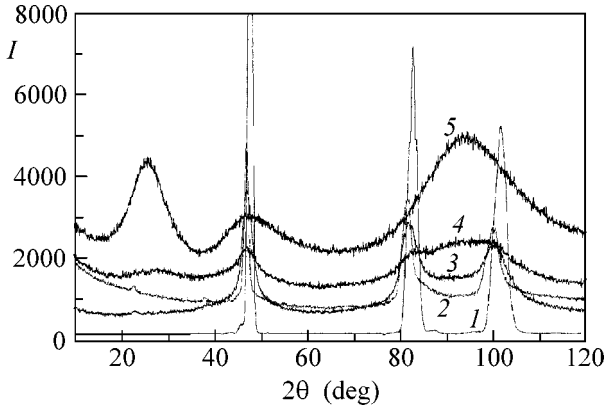

Fig. 1. Diffraction patterns upon the transition from a diamond-like glass to a graphite-like structure upon change in density: (*1*) initial diamond, (*2*) 3.38, (*3*) 3.10, (*4*) 2.68, and (*5*) 2.11 g/cm^3.

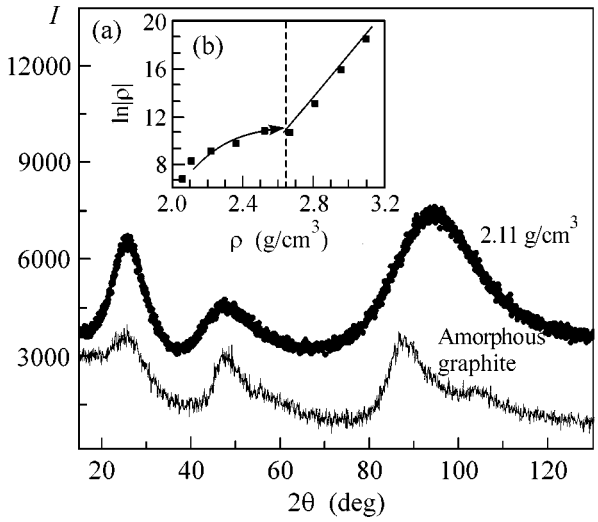

Fig. 2. (a) Diffraction patterns for low-density irradiated diamond (2.11 g/cm^3) and amorphous graphite and (b) resistivity vs. density.

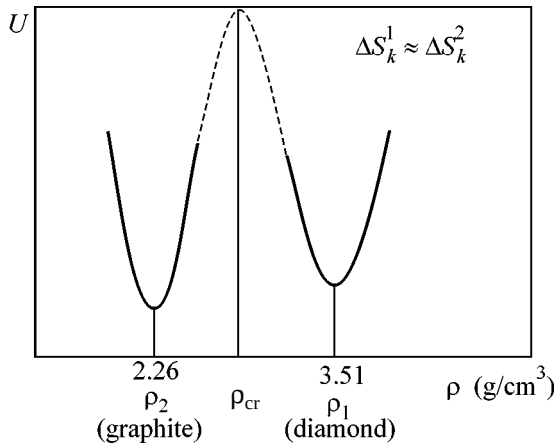

Fig. 3. Internal energy U vs. density for a polyamorphic transition at $\rho_{cr} \approx 2.7$ g/cm^3; ΔS_k is the configuration entropy.

This transition is accompanied by a change in the resistivity of powders, which is measured by means of pressure contacts (Fig. 2b). The total change in resistivity is equal to six orders of magnitude in the density range under investigation and corresponds to a transition from the dielectric state to the metal one. The critical density, i.e., the density at which the transition occurs, is equal to $\rho \cong 2.7$–2.9 g/cm^3 according both to diffraction measurements and to electric-resistivity measurements.

Since the polyamorphic transition occurs between disordered phases at low temperatures, the role of entropy is not as large as in polymorphic transitions in a crystalline state, and the transition occurs due to a change in the internal energy, as is shown schematically in Fig. 3. According to Fig. 3, the transition between amorphous phases (diamond-like and graphite-like) is attributed to the existence of their crystalline analogs, which differ both in density and in the coordination number, so that polyamorphism is closely associated with polymorphism and the critical density of the transition corresponds to a saddle point and is approximately equal to the average density of crystalline analogues. A similar phenomenon likely occurs in high-pressure amorphous phases (SiO_2, H_2O, etc.). Transitions with a change in the coordination number (tetra–octa) are characteristic of a "lattice fluid"—solutions of hydrogen in metals [14]—where they occur upon change in temperature, pressure, and incorporated-atom concentration [15, 16]. Finally, a similar phenomenon was recently observed upon the annealing of radiation-amorphized fullerene hydrides [17]. Therefore, it is not excluded that polyamorphic transitions are not rare upon sufficiently large change in density. In this case, the effect of pressure ($\Delta V < 0$) and irradiation ($\Delta V > 0$) makes it possible to change density over a wide range (to a factor of 2–4).

Further experiments with irradiated diamonds at high pressures and temperatures must show whether the observed transition is reversible upon decreasing volume or amorphous phases are crystallized into stable or metastable structures.

This work was supported by the Russian Foundation for Basic Research (project no. 03-02-17387) and Program "Neutron Investigations of Condensed Media."

REFERENCES

1. C. Benmore and J. Siewenie, Neutron News **15**, 16 (2004).
2. M. A. Floriano, Y. P. Handa, D. D. Klug, and E. Whalley, J. Chem. Phys. **91**, 7187 (1989).
3. O. J. Mishima, J. Chem. Phys. **100**, 5910 (1994).
4. A. M. Balagurov, O. I. Barkalov, A. I. Kolesnikov, *et al.*, JETP Lett. **53**, 30 (1991).
5. E. G. Ponyatovsky, High Press. Res. **17**, 157 (2000).
6. S. Sampath, C. J. Benmore, K. M. Lantzky, *et al.*, Phys. Rev. Lett. **90**, 115502 (2003).
7. C. A. Tulk, C. J. Benmore, J. Urquidi, *et al.*, Science **297**, 1320 (2002).
8. E. V. Antonov, O. I. Barkalov, V. K. Fedotov, *et al.*, Phys. Rev. B **62**, 3130 (2000).
9. E. R. Vance, J. Phys. C: Solid State Phys. **4**, 257 (1971).
10. M. Ya. Kats, *New Methods in Studies of Minerals in Gravitational Field* (Nauka, Moscow, 1966), p. 162 [in Russian].

11. V. P. Glazkov, I. V. Naumov, V. A. Somenkov, *et al.*, Nucl. Instrum. Methods Phys. Res. A **264**, 367 (1988).
12. V. A. Nikolaenko, O. O. Zabusov, S. S. Agafonov, *et al.*, in *Abstracts of XVIII Meeting on Use of Neutron Scattering in Studies of Condensed State* (Zarechnyĭ, Russia, 2004), p. 93.
13. P. A. Platonov, O. K. Chugunov, S. I. Alekseev, *et al.*, Preprint IAÉ-2266 (Inst. of Atomic Energy, Moscow, 1973).
14. V. A. Somenkov and S. Sh. Shilstein, Prog. Mater. Sci. **24**, 267 (1979).
15. V. A. Somenkov, A. V. Irodova, and S. Sh. Shil'shteĭn, Fiz. Tverd. Tela (Leningrad) **28**, 3200 (1986) [Sov. Phys. Solid State **28**, 1804 (1986)].
16. Y. Fukai, J. Alloys Compd. **231**, 35 (1995).
17. V. I. Voronin, V. P. Glazkov, B. N. Goshchitskiĭ, *et al.*, in *Abstracts of XVII Meeting on Use of Neutron Scattering in Studies of Condensed State* (Gatchina, Russia, 2002), p. 169.

Translated by R. Tyapaev

JETP Letters, Vol. 81, No. 3, 2005, pp. 125–130. From Pis'ma v Zhurnal Éksperimental'noĭ i Teoreticheskoĭ Fiziki, Vol. 81, No. 3, 2005, pp. 157–161.

Effective Conductivity of 2D Isotropic Two-Phase Systems in a Magnetic Field¶

S. A. Bulgadaev[1] and F. V. Kusmartsev[2]

[1] *Landau Institute for Theoretical Physics, Russian Academy of Sciences, Chernogolovka, Moscow region, 142432 Russia*
e-mail: bulgad@itp.ac.ru

[2] *Department of Physics, Loughborough University, Loughborough, LE11 3TU, UK*
e-mail: F.Kusmartsev@lboro.ac.uk

Received December 21, 2004

Using the linear fractional transformation, which connects the effective conductivities $\hat{\sigma}_e$ of isotropic two-phase systems with and without magnetic field, explicit approximate expressions for $\hat{\sigma}_e$ in a magnetic field are obtained. They allow one to describe $\hat{\sigma}_e$ of various inhomogeneous media at arbitrary phase concentrations x and magnetic fields. The x-dependence plots of $\hat{\sigma}_e$ at some values of inhomogeneity and magnetic field are constructed. Their behavior is qualitatively compatible with the existing experimental data. The obtained results are applicable to different two-phase systems (regular and irregular as well as random), which satisfy the symmetry and self-duality conditions, and admit direct experimental checking. © *2005 Pleiades Publishing, Inc.*

PACS numbers: 72.80.Ng, 72.80.Tm, 73.61.–r, 75.70.Ak

1. INTRODUCTION

During investigations of the magnetoresistive properties of new materials, which are connected with the high-temperature superconductivity (such as oxide materials with the perovskite-type structure), it was established that they often have unusual transport properties. For example, the magnetoresistance becomes very large (the so-called colossal magnetoresistance in such materials as manganites) [1] or grows approximately linearly with magnetic field up to very high fields (in silver chalcogenides) [2]. There is an opinion that these properties take place due to phase inhomogeneities in these materials [2]. For this reason, a calculation of the effective conductivity σ_e of inhomogeneous heterophase systems without and with magnetic field at arbitrary partial conductivities and phase concentrations is a very important problem. Unfortunately, the existing effective medium approximations (EMA) cannot give explicit simple formulas for magnetoresistivity that are convenient for a description of the experimental results in a wide range of partial parameters even for two-phase random systems [3]. Such formulas can be obtained for some systems only in a high magnetic field [3, 4].

The situation is much better for 2D inhomogeneous systems in a perpendicular magnetic field. Here, due to their exact duality properties, not only a few exact results have been obtained for the effective conductivity of random inhomogeneous systems [5–10], but transformations connecting the effective conductivities of isotropic two-phase inhomogeneous systems with and without magnetic field have also been constructed [9, 11]. This transformation, in principle, permits one to obtain explicit expressions for σ_e in a magnetic field if the corresponding expressions are known for σ_e without magnetic field. Such explicit approximate expressions for σ_e have been obtained earlier in some limiting cases, for example, at a small concentration of one phase, for weakly inhomogeneous media [11], or for inclusions of super- or nonconducting phases [6–8, 11]. In this letter, we will present the explicit approximate expressions for $\hat{\sigma}_e$ at arbitrary phase concentrations and in a wide region of partial conductivities, using the full dual transformation recently constructed in [10] and the corresponding expressions for σ_e at $\mathbf{H} = 0$ from [12]. We will also give the x-dependence plots of $\hat{\sigma}_e$ at some characteristic values of magnetic field $\mathbf{H}$, which show a very interesting behavior that is compatible with experimental results from [1, 2].

2. DUAL TRANSFORMATION BETWEEN SYSTEMS WITH $\mathbf{H} \neq 0$ AND $\mathbf{H} = 0$

The effective conductivity of two-phase isotropic systems in a magnetic field has the following form:

¶ This article was submitted by the authors in English.

$$\hat{\sigma} = \sigma_{ik} = \sigma_d\delta_{ik} + \sigma_t\epsilon_{ik}, \quad \sigma_d(\mathbf{H}) = \sigma_d(-\mathbf{H}), \quad \sigma_t(\mathbf{H}) = -\sigma_t(-\mathbf{H}), \tag{1}$$

here, δ_{ik} is the Kronecker symbol and ϵ_{ik} is the unit antisymmetric tensor. The effective conductivity $\hat{\sigma}_e$ of two-phase self-dual (random or regular symmetric) systems with the partial conductivities σ_{id}, σ_{it} ($i = 1, 2$) (we assume that $\sigma_{id} \geq 0$) and concentrations x_i must be a symmetric function of pairs of arguments $(\hat{\sigma}_i, x_i)$ and a homogeneous (degree 1) function of $\sigma_{di,\,ti}$. For this reason, it is invariant under permutation of pairs of partial parameters:

$$\hat{\sigma}_e(\hat{\sigma}_1, x_1|\hat{\sigma}_2, x_2) = \hat{\sigma}_e(\hat{\sigma}_2, x_2|\hat{\sigma}_1, x_1). \tag{2}$$

The effective conductivity of two-phase systems must also reduce to some partial $\hat{\sigma}_i$ if $x_i = 1$ ($i = 1, 2$).

Below, it will be more convenient to use the complex representation for coordinates and vector fields [13]:

$$z = x + iy, \quad j = j_x + ij_y,$$
$$e = e_x + ie_y, \quad \sigma = \sigma_d + i\sigma_t.$$

The complex conductivity transforms as [5]

$$\sigma' = T(\sigma) = \frac{c\sigma - ib}{-id\sigma + a}, \tag{3}$$

where a, b, c, d are real numbers. This transformation generalizes the inversion transformations of systems without magnetic field. Thus, the dual transformations (DT) in systems with magnetic field have a richer structure due to the fact that they are connected with some subgroup of a group of linear fractional transformations, conserving the imaginary axis in the complex conductivity plane [5, 7, 9]. The transformation T depends on three real parameters (since one of four parameters can be factored due to the fractional structure of T). There are various ways to choose these three parameters. In our treatment, it will be convenient to factor d. This gives the three parameters $\bar{a} = a/d$, $\bar{b} = b/d$, and $\bar{c} = c/d$ determining the transformation T.

Transformation (3) has the following form in terms of conductivity components σ_d and σ_t:

$$\sigma'_d = \sigma_d\frac{ac + bd}{(d\sigma_d)^2 + (a + d\sigma_t)^2} = \bar{c}\sigma_d\frac{\bar{a} + \bar{b}/\bar{c}}{(\sigma_d)^2 + (\bar{a} + \sigma_t)^2},$$

$$\sigma'_t = \frac{cd\sigma_d^2 + (a + d\sigma_t)(c\sigma_t - b)}{(d\sigma_d)^2 + (a + d\sigma_t)^2} \tag{4}$$

$$= \bar{c}\frac{\sigma_d^2 + (\bar{a} + \sigma_t)(\sigma_t - b/c)}{(\sigma_d)^2 + (\bar{a} + \sigma_t)^2}.$$

These DT allow one to construct the transformation, connecting effective conductivities of two-phase systems with magnetic field and without it. Analogous connections have been found firstly on a basis of solutions of the corresponding Laplace and boundary equations [11], but there are some ambiguity problems with the determination of the parameters of the intermediate artificial system. Later, this transformation was constructed directly from the DT under two simplifying conjectures in [9]. Recently, in [10], it was constructed in the full form, using all three parameters and explicitly reproducing the known exact values for σ_e. The parameters of such a transformation (let us call it T_h; we will also omit the bars over its parameters), a, $b' = b/c$, and c, depend on the partial conductivities and have the following form:

$$a_\pm = \frac{|\sigma_2|^2 - |\sigma_1|^2 \pm \sqrt{B}}{2(\sigma_{1t} - \sigma_{2t})},$$

$$b'_\pm = \frac{|\sigma_1|^2 - |\sigma_2|^2 \pm \sqrt{B}}{2(\sigma_{1t} - \sigma_{2t})}, \quad c = -a, \tag{5}$$

$$B = [(\sigma_{1t} - \sigma_{2t})^2 + (\sigma_{1d} - \sigma_{2d})^2]$$

$$\times [(\sigma_{1t} - \sigma_{2t})^2 + (\sigma_{1d} + \sigma_{2d})^2],$$

where $|\sigma_i|^2 = \sigma_{id}^2 + \sigma_{it}^2$, and, evidently, $B \geq 0$. The diagonal (or real) parts of σ_i transform under T_h as

$$\sigma'_{id} = \sigma_{id}\frac{c(a + b')}{(\sigma_{id})^2 + (a + \sigma_{it})^2} = \frac{c\sigma_{id}}{\sigma_{ai}}, \tag{6}$$
$$\sigma_{ai} = a + \sigma_{it}.$$

The parameters a, b, and c satisfy also the additional relations [10]

$$A = \left[1 + \left(\frac{\sigma_{1t} - \sigma_{2t}}{\sigma_{1d} + \sigma_{2d}}\right)^2\right]^{1/2} = \frac{(a + b')(\sigma_{a1}\sigma_{a2})^{1/2}}{\sigma_{1d}\sigma_{2d} + \sigma_{a1}\sigma_{a2}}, \tag{7}$$

$$\frac{\sigma_{1d}\sigma_{2t} + \sigma_{2d}\sigma_{1t}}{\sigma_{1d} + \sigma_{2d}} = c\frac{\sigma_e'^2 - ab'}{\sigma_e'^2 + a^2}$$
$$= c\frac{\sigma_{1d}\sigma_{2d} - (b'/a)\sigma_{a1}\sigma_{a2}}{\sigma_{1d}\sigma_{2d} + \sigma_{a1}\sigma_{a2}}, \tag{8}$$

which ensure the reproduction of the exact results for σ_e at the equal phase concentrations $x_1 = x_2 = 1/2$. Relations (7) and (8) give us a highly nontrivial check of the self-consistency of the transformation. The direct check them is a rather complicated task. Fortunately, as was conjectured in [9] and shown in [10], T_h transforms a circumference (see Fig. 1) with a radius R, centered on

the imaginary axis at iz_0 and passing through the two points σ_1 and σ_2, where

$$R = \frac{|a+b|}{2} = \frac{\sqrt{B}}{2|\sigma_{1t}-\sigma_{2t}|}, \qquad z_0 = \frac{-a+b'}{2} = \frac{|\sigma_1|^2-|\sigma_2|^2}{2(\sigma_{1t}-\sigma_{2t})}, \tag{9}$$

into the real axis and the real axis into this circumference. All equalities necessary for fulfillment of (7) and (8) correspond to the known equalities between lengths of various chords, their projections on a diameter, and the radius of the circles. For example, equality (7) takes the form

$$A = \frac{2R\sigma_a}{\sigma_a^2+\sigma_{1d}\sigma_{2d}} = 1/(1-\delta/2R\sigma_a), \qquad \sigma_a^2 = \sigma_{a1}\sigma_{a2}, \tag{10}$$

where σ_a^2 is the squared geometrical average of σ_{ai} (i = 1, 2) (this interpretation is possible due to the fact that the σ_{ai} always have the same sign [9]), and δ defines the difference between $\sigma_x^2 = 2R\sigma_a - \sigma_a^2$, a squared real projection of the chord, having an imaginary projection σ_a, and a squared geometric average of σ_{id},

$$\delta = \sigma_x^2 - \sigma_{1d}\sigma_{2d}. \tag{11}$$

3. INHOMOGENEOUS SYSTEMS WITH COMPACT INCLUSIONS

Now, having all formulas for the transformation, one can construct the explicit expressions for σ_e of an inhomogeneous system in a magnetic field. Below, in order to simplify the subsequent formulas, we will omit the subindex d in the partial diagonal parts σ_{id} (i = 1, 2). First, we consider the case of compact inclusions of one phase into another. The corresponding effective conductivity σ_e has the form ($x_1 = x$, $x_2 = 1 - x$) [12]

$$\sigma_e(\{\sigma\},\{x\}) = \sigma_1^x\sigma_2^{1-x}. \tag{12}$$

Substituting the primed partial conductivities into (12), one obtains the diagonal primed effective conductivity

$$\sigma'_{ed}(\{\sigma\},\{x\}) = c\left(\frac{\sigma_1}{\sigma_{a1}}\right)^x\left(\frac{\sigma_2}{\sigma_{a2}}\right)^{1-x}. \tag{13}$$

Then, substituting σ'_{ed} into (4) and remembering that the primed transverse effective conductivity $\sigma'_{et} = 0$, one obtains for the diagonal part σ_{ed} of the effective

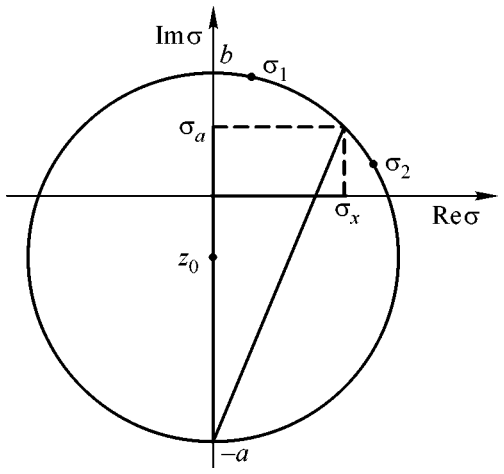

Fig. 1. A schematic picture of the chord defining a geometrical sense of the factor A from the expression for the real part of the exact σ_e.

conductivity of these systems in a magnetic field the following expression:

$$\sigma_{ed}(\{\sigma\},\{x\}) = \frac{\sigma'_{ed}(ac+b)}{(\sigma'_{ed})^2+a^2} = \frac{(a+b')\left(\frac{\sigma_1}{\sigma_{a1}}\right)^{x_1}\left(\frac{\sigma_2}{\sigma_{a2}}\right)^{x_2}}{1+\left(\frac{\sigma_1}{\sigma_{a1}}\right)^{2x_1}\left(\frac{\sigma_2}{\sigma_{a2}}\right)^{2x_2}}. \tag{14}$$

One can check, using relation (7), that (14) correctly reduces to σ_i when x_i = 1 and to the exact formula for σ_e at $x_1 = x_2 = 1/2$. For example, at $x_1 = 1$, $x_2 = 0$, Eq. (14) reduces to

$$\sigma_{ed}(\{\sigma\}, x_1 = 1) = \frac{\sigma_1}{\sigma_{a1}}\frac{(a+b')}{1+\left(\frac{\sigma_1}{\sigma_{a1}}\right)^2} = \sigma_1,$$

where, at the last step, we have used relation (7) at $\sigma_1 = \sigma_2$.

Analogously, for the transverse part σ_{et} one obtains

$$\sigma_{et}(\{\sigma\},\{x\}) = c\frac{(\sigma'_{ed})^2-ab'}{(\sigma'_{ed})^2+a^2} = \frac{b'-a\left(\frac{\sigma_1}{\sigma_{a1}}\right)^{2x_1}\left(\frac{\sigma_2}{\sigma_{a2}}\right)^{2x_2}}{1+\left(\frac{\sigma_1}{\sigma_{a1}}\right)^{2x_1}\left(\frac{\sigma_2}{\sigma_{a2}}\right)^{2x_2}}. \tag{15}$$

Again, now using relation (8), one can check that (15) correctly reproduces the boundary values at $x_i = 1$ ($i = 1, 2$) as well as the exact value at equal concentrations $x_1 = x_2 = 1/2$.

4. INHOMOGENEOUS SYSTEMS WITH A "RANDOM PARQUET" STRUCTURE

In this section, we present analogous formulas for 2D isotropic inhomogeneous systems with inhomogeneity structures of the "random parquet" type [12]. The effective conductivity of such systems without a magnetic field is [12]

$$\sigma_e(\{\sigma\}, \{x\}) = \sqrt{\langle\sigma\rangle/\langle\sigma^{-1}\rangle} = \sqrt{\sigma_1\sigma_2}\left(\frac{x_1\sigma_1 + x_2\sigma_2}{x_1\sigma_2 + x_2\sigma_1}\right)^{1/2}. \quad (16)$$

Then, the diagonal part of the primed effective conductivity σ'_e has the form

$$\sigma'_{ed}(\{\sigma\}, \{x\}) = c\left(\frac{\sigma_1}{\sigma_{a1}}\frac{\sigma_2}{\sigma_{a2}}\right)^{1/2}\left(\frac{x_1\left(\frac{\sigma_1}{\sigma_{a1}}\right) + x_2\left(\frac{\sigma_2}{\sigma_{a2}}\right)}{x_1\left(\frac{\sigma_2}{\sigma_{a2}}\right) + x_2\left(\frac{\sigma_1}{\sigma_{a1}}\right)}\right)^{1/2}. \quad (17)$$

Its substitution into (4) gives, for the diagonal part of the effective conductivity σ_{ed},

$$\sigma_{ed}(\{\sigma\}, \{x\}) = (a + b')\frac{\left(\frac{\sigma_1}{\sigma_{a1}}\frac{\sigma_2}{\sigma_{a2}}\right)^{1/2}\left(\frac{x_1\left(\frac{\sigma_1}{\sigma_{a1}}\right) + x_2\left(\frac{\sigma_2}{\sigma_{a2}}\right)}{x_1\left(\frac{\sigma_2}{\sigma_{a2}}\right) + x_2\left(\frac{\sigma_1}{\sigma_{a1}}\right)}\right)^{1/2}}{1 + \frac{\sigma_1}{\sigma_{a1}}\frac{\sigma_2}{\sigma_{a2}}\left(\frac{x_1\left(\frac{\sigma_1}{\sigma_{a1}}\right) + x_2\left(\frac{\sigma_2}{\sigma_{a2}}\right)}{x_1\left(\frac{\sigma_2}{\sigma_{a2}}\right) + x_2\left(\frac{\sigma_1}{\sigma_{a1}}\right)}\right)}. \quad (18)$$

One can check, using relation (7), that (18) reduces to the right values at $x_i = 1$, ($i = 1, 2$), as well as for $x_1 = x_2 = 1/2$. For the transverse part σ_{et}, one obtains

$$\sigma_{et}(\{\sigma\}, \{x\}) = \frac{b' - a\left(\frac{\sigma_1}{\sigma_{a1}}\frac{\sigma_2}{\sigma_{a2}}\right)\left(\frac{x_1\left(\frac{\sigma_1}{\sigma_{a1}}\right) + x_2\left(\frac{\sigma_2}{\sigma_{a2}}\right)}{x_1\left(\frac{\sigma_2}{\sigma_{a2}}\right) + x_2\left(\frac{\sigma_1}{\sigma_{a1}}\right)}\right)}{1 + \left(\frac{\sigma_1}{\sigma_{a1}}\frac{\sigma_2}{\sigma_{a2}}\right)\left(\frac{x_1\left(\frac{\sigma_1}{\sigma_{a1}}\right) + x_2\left(\frac{\sigma_2}{\sigma_{a2}}\right)}{x_1\left(\frac{\sigma_2}{\sigma_{a2}}\right) + x_2\left(\frac{\sigma_1}{\sigma_{a1}}\right)}\right)}. \quad (19)$$

Again, now using relation (8), one can check that (19) correctly reproduces the boundary values as well as the exact value at equal concentrations.

5. EFFECTIVE MEDIUM APPROXIMATION IN A MAGNETIC FIELD

In this section, we find, for completeness, a "magnetic" transformation for the traditional effective medium approximation (EMA) for the effective conductivity. The EMA for σ_e in inhomogeneous two-phase self-dual systems without a magnetic field has the form [14]

$$\sigma_e(\{\sigma\}, \{x\}) = \left(x - \frac{1}{2}\right)\sigma_- + \sqrt{\left(x - \frac{1}{2}\right)^2\sigma_-^2 + \sigma_1\sigma_2}, \quad (20)$$

where $\sigma_- = (\sigma_1 - \sigma_2)$. Then, the primed effective conductivity will be

$$\sigma'_{ed}(\{\sigma\}, \{x\}) = c\left(\left(x - \frac{1}{2}\right)\sigma_{a-} + \sqrt{\left(x - \frac{1}{2}\right)^2\sigma_{a-}^2 + \frac{\sigma_1}{\sigma_{a1}}\frac{\sigma_2}{\sigma_{a2}}}\right), \quad (21)$$

here, $\sigma_{a-} = \sigma_1/\sigma_{a1} - \sigma_2/\sigma_{a2}$. Substituting (21) into (4), one obtains, for the diagonal part σ_{ed}, the expression

$$\sigma_{ed}(\{\sigma\}, \{x\}) = \frac{(a + b')\left(\left(x - \frac{1}{2}\right)\sigma_{a-} + \sqrt{\left(x - \frac{1}{2}\right)^2\sigma_{a-}^2 + \frac{\sigma_1}{\sigma_{a1}}\frac{\sigma_2}{\sigma_{a2}}}\right)}{1 + \left(\left(x - \frac{1}{2}\right)\sigma_{a-} + \sqrt{\left(x - \frac{1}{2}\right)^2\sigma_{a-}^2 + \frac{\sigma_1}{\sigma_{a1}}\frac{\sigma_2}{\sigma_{a2}}}\right)^2}. \quad (22)$$

One can check, using relation (7), that (22) correctly reduces to σ_i when $x_i = 1$ and to the exact formula for σ_e at $x_1 = x_2 = 1/2$. For example, at $x_1 = 1$, $x_2 = 0$, Eq. (22) reduces to

$$\sigma_{ed}(\{\sigma\}, x_1 = 1) = \frac{(a + b')\sigma_1\sigma_{a1}}{\sigma_{a1}^2 + \sigma_1^2} = \sigma_1.$$

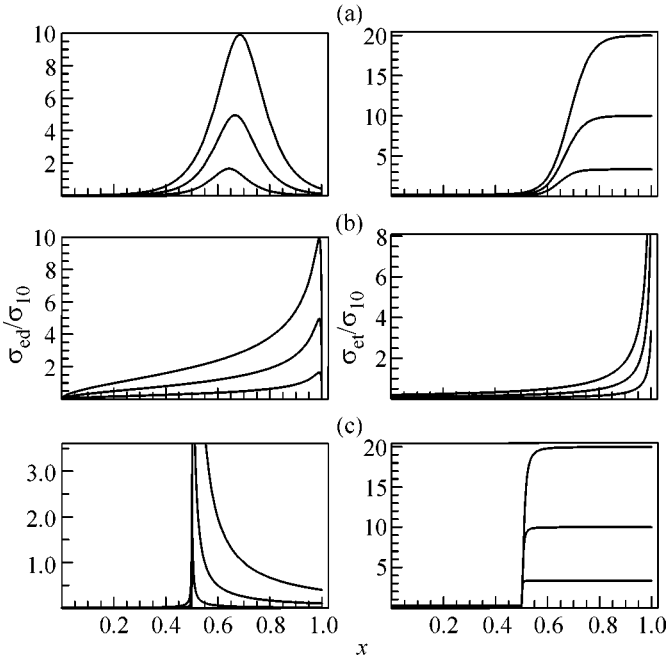

Fig. 2. The plots of the x dependence of the normalized diagonal σ_{ed}/σ_{10} and transverse σ_{et}/σ_{10} parts (magnified in 1000 times) for the three explicit expressions obtained above (respectively, (a)–(c)) at the inhomogeneity parameter $\sigma_{20}/\sigma_{10} = 0.01$, and at three different (dimensionless) values of magnetic field H: (*1*) 50, (*2*) 100, and (*3*) 300 (the corresponding plots go from the upper to the lower ones).

Analogously, substituting (21) into (4), one obtains, for the transverse part of the effective conductivity,

$$\sigma_{et}(\{\sigma\},\{x\}) = \frac{b' - a\left(\left(x-\frac{1}{2}\right)\sigma_{a-} + \sqrt{\left(x-\frac{1}{2}\right)^2\sigma_{a-}^2 + \frac{\sigma_1}{\sigma_{a1}}\frac{\sigma_2}{\sigma_{a2}}}\right)^2}{1 + \left(\left(x-\frac{1}{2}\right)\sigma_{a-} + \sqrt{\left(x-\frac{1}{2}\right)^2\sigma_{a-}^2 + \frac{\sigma_1}{\sigma_{a1}}\frac{\sigma_2}{\sigma_{a2}}}\right)^2}. \quad (23)$$

Again, now using relation (8), one can check that (23) correctly reproduces the boundary values as well as the exact value at equal concentrations.

It follows from the property of the transformation T_h that σ_e belongs to circumference (9) for all phase concentrations $x \in [0, 1]$ [9, 10]. The effective conductivity maps the concentration segment [0, 1] into the corresponding arc of this circumference, connecting the points σ_1 and σ_2. The different expressions for σ_e correspond to the different mappings. A comparison of these mappings is presented in [15].

6. EFFECTIVE CONDUCTIVITY IN MAGNETIC FIELD

Thus, we have found the desired formulas. Substituting into (14), (15), (18), (19), (22), and (23) the known functions $\sigma_{id}(\mathbf{H})$, $\sigma_{it}(\mathbf{H})$, ($i = 1, 2$), one obtains explicit expressions for the diagonal $\sigma_{ed}(\mathbf{H})$ and transverse $\sigma_{et}(\mathbf{H})$ parts of the effective conductivity of inhomogeneous systems in a magnetic field. We give here (see Fig. 2) their x-dependence plots for two-phase systems, whose partial conductivities in a magnetic field can be approximated by the standard (metallic type) formulas [5, 3]

$$\sigma_{id}(\mathbf{H}) = \frac{\sigma_{i0}}{1+\beta_i^2}, \quad \sigma_{it}(\mathbf{H}) = \frac{\sigma_{i0}\beta_i}{1+\beta_i^2}, \quad \beta_i = \mu_i H, \quad i = 1, 2, \quad (24)$$

where μ_i are the corresponding mobilities. We will assume here, for simplicity, that $\mu_1 \sim \mu_2 \sim 1$. One can see from Fig. 2 that the behavior of the effective conductivities, though different for various expressions, has two common characteristic features: (1) the absolute values of σ_{ed} are very small, even at high peaks; (2) all values in the regions with noticeable values of σ_e decrease with an increase in H at relatively large H approximately linearly. Since σ_{id} decrease $\sim H^{-2}$, the second feature effectively induces a narrowing of the peaks, which are rather asymmetric and dependent on the structure of inhomogeneities (i.e., on the form of the explicit expressions). Both of these properties are qualitatively compatible with the experimental results from [1, 2], which show a large magnetoresistivity and its approximately linear growth with an increase in H. More detailed analysis and comparisons with experimental results will be presented in subsequent papers.

7. CONCLUSIONS

Using the exact duality transformation, we have found three explicit approximate expressions for the effective conductivity of 2D isotropic two-phase systems in a magnetic field. The three plots of the dependence of $\sigma_{ed,\,et}$ on the phase concentration at the inhomogeneity parameter $\sigma_{20}/\sigma_{10} = 0.01$ and at different values of magnetic field are constructed. They show the very interesting behavior of $\sigma_{ed}(\mathbf{H})$ and $\sigma_{et}(\mathbf{H})$, which is qualitatively compatible with the experimental data from [1, 2]. The obtained results can be applied for a description of σ_e of various two-phase systems (regular and irregular, as well as random), satisfying the symmetry and self-duality conditions, in a wide range of partial conductivities and at arbitrary concentrations and magnetic fields. All of these results permit direct experimental checking.

The authors are thankful to Prof. A.P. Veselov for very useful discussions of some mathematical questions. This work was supported by the Russian Foundation for Basic Research (project nos. 00-15-96579, 02-02-16403) and by the Royal Society (UK) (grant no. 2004/R4-EF).

REFERENCES

1. G. Allodi *et al.*, Phys. Rev. B **56**, 6036 (1997); M. Hennion *et al.*, Phys. Rev. Lett. **81**, 1957 (1998); Y. Moritomo *et al.*, Phys. Rev. B **60**, 9220 (1999).
2. R. Xu *et al.*, Nature **390**, 57 (1997).
3. D. J. Bergmann and D. Stroud, Phys. Rev. B **62**, 6603 (2000).
4. Yu. A. Dreizin and A. M. Dykhne, Zh. Éksp. Teor. Fiz. **63**, 242 (1972) [Sov. Phys. JETP **36**, 127 (1973)]; I. M. Kaganova and M. I. Kaganov, cond-mat/0402426 (2004).
5. A. M. Dykhne, Zh. Éksp. Teor. Fiz. **59**, 641 (1970) [Sov. Phys. JETP **32**, 348 (1970)].
6. A. L. Efros and B. I. Shklovskii, Phys. Status Solidi B **76**, 475 (1976).
7. B. I. Shklovskii, Zh. Éksp. Teor. Fiz. **72**, 288 (1977) [Sov. Phys. JETP **45**, 152 (1977)].
8. D. G. Stroud and D. J. Bergmann, Phys. Rev. B **30**, 447 (1984).
9. G. W. Milton, Phys. Rev. B **38**, 11296 (1988).
10. S. A. Bulgadaev and F. V. Kusmartsev, Phys. Lett. A **336**, 223 (2005).
11. B. Ya. Balagurov, Zh. Éksp. Teor. Fiz. **82**, 1333 (1982) [Sov. Phys. JETP **55**, 774 (1982)].
12. S. A. Bulgadaev, Pis'ma Zh. Éksp. Teor. Fiz. **77**, 615 (2003) [JETP Lett. **77**, 516 (2003)]; Europhys. Lett. **64**, 482 (2003); cond-mat/0410058.
13. L. D. Landau and E. M. Lifshitz, *Course of Theoretical Physics*, Vol. 8: *Electrodynamics of Continuous Media* (Nauka, Moscow, 1982; Pergamon, New York, 1984).
14. S. Kirkpatrick, Rev. Mod. Phys. **45**, 574 (1973).
15. S. A. Bulgadaev and F. V. Kusmartsev, Phys. Lett. A (in press).

JETP Letters, Vol. 81, No. 3, 2005, pp. 131–134. Translated from Pis'ma v Zhurnal Éksperimental'noĭ i Teoreticheskoĭ Fiziki, Vol. 81, No. 3, 2005, pp. 162–165.

Magnetoresistance of the Quasi-One-Dimensional Conductor $NbSe_3$ with a Charge Density Wave in Magnetic Fields of Different Orientations

A. A. Sinchenko[1], Yu. I. Latyshev[2], and P. Monceau[3]

[1] *Moscow Engineering Physics Institute, Kashirskoe sh. 31, Moscow, 115409 Russia*
[2] *Institute of Radio Engineering and Electronics, Russian Academy of Sciences, Moscow, 103907 Russia*
[3] *Centre de Recherches sur les tres Basses Temperatures, BP 166, 38042 Grenoble, France*

Received December 27, 2004

The magnetoresistance of $NbSe_3$ single crystals is measured as a function of magnetic field for different field orientations. A possibility of studying the Fermi surface by using the dependence of the Shubnikov–de Haas oscillation phase on the rotation angle of the magnetic field is demonstrated. The results of the study show that the quasi-momenta of carriers that are not condensed in the charge density wave are predominantly oriented along the conducting chains. © *2005 Pleiades Publishing, Inc.*

PACS numbers: 71.45.Lr, 73.40.Ns, 74.80.Fp

Among numerous quasi-one-dimensional compounds with charge density waves (CDWs), $NbSe_3$ occupies a special place. This material undergoes two Peierls transitions at the temperatures T_{p1} = 145 K and T_{p2} = 59 K, below which energy gaps appear at the Fermi level in the single-particle excitation spectrum. However, unlike most materials with CDWs, the electronic spectrum of $NbSe_3$ does not become completely dielectric and the metal properties of $NbSe_3$ persist down to the lowest temperatures. As a result of incomplete nesting, normal carriers are retained in small "pockets" at the Fermi level [1].

Recent studies of electron transport across the conducting layers of $NbSe_3$ (along the a^* axis of the crystal) revealed an unusual effect: the current–voltage characteristics of $NbSe_3$-based mesoscopic overlap structures exhibited an anomalously strong peak of dynamic conductivity at zero bias voltage. In addition, despite the fact that a typical mesoscopic structure contains several tens of conducting layers, an increase in the bias voltage was accompanied by the appearance of dynamic conductivity peaks corresponding to twice the first and second Peierls energy gaps of $NbSe_3$ [2, 3]. This phenomenon was explained by assuming the coherent interlayer tunneling of normal carriers that are not condensed in CDWs. Coherent tunneling means tunneling with carrier-momentum conservation. This brings up the question: Why is the momentum conserved in the case under discussion? To answer it, one must study more closely the state of the carriers localized in the pockets. The situation may also be clarified by studying the behavior of magnetoresistance in this material. It should be noted that the magnetoresistance of $NbSe_3$ had been measured in many experiments. For example, the Shubnikov–de Haas (SdH) oscillation frequency was measured and the shape of the pockets of the Fermi surface was determined in [4–7]. According to [5], the Fermi surface areas that are not covered by the gap have shapes close to ellipsoids with an axial ratio of about 7 and with their major axes parallel (or almost parallel) to the c axis of the crystal. Note that, in the aforementioned studies, the measurements were performed using the modulation technique, which cuts off the constant (nonoscillating) component of magnetoresistance.

The magnetoresistance measurements in a constant magnetic field were reported in [8–12]. However, the emphasis there was on the study of the effect of the CDW state on the Fermi surface (deformation or CDW slip state). At the same time, many aspects of the magnetoresistance behavior remain unclear. For example, the effect of the magnetic field orientation on the magnetoresistance of $NbSe_3$ has never been investigated. The study of this effect is reported in this paper.

For our measurements, we chose high-quality $NbSe_3$ single crystals thinner than 5 μm with the ratio R(300 K)/R(4.2 K) > 100. Resistance was measured by the standard four-terminal technique with a current from 1 to 100 μm, depending on the cross section of the sample. In all cases, the current was two or three orders of magnitude lower than the current corresponding to the CDW slip onset. A magnetic field up to 8.5 T was produced by a superconducting solenoid. The samples were oriented so that the magnetic field was parallel to the conducting layers of the crystal (the b–c plane). The sample could be rotated about the a^* axis of the crystal by a rotating mechanism, which provided the angle set-

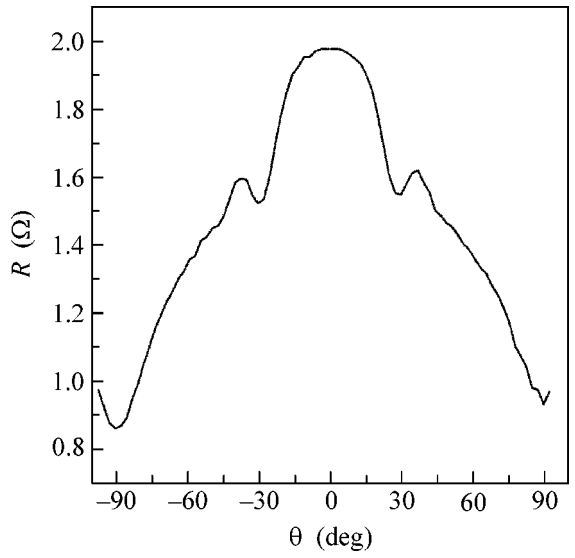

Fig. 1. Magnetoresistance R of one of the samples under study in a magnetic field $B = 8.5$ T vs. the angle θ between the field direction and the c axis of the crystal.

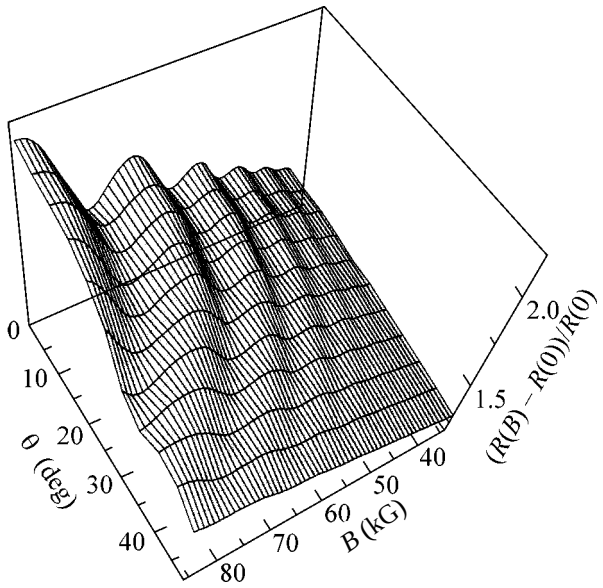

Fig. 2. Three-dimensional pattern of SdH oscillations for the magnetic field rotation in the b–c plane of the crystal. The angle θ is measured with respect to the c axis. The sample is the same as in Fig. 1.

ting with an accuracy of about 1°. All measurements were performed at liquid-helium temperature.

For all magnetic field orientations studied, in the region $B > 1$ T, the nonoscillating component of magnetoresistance increased linearly with the magnetic field. This result agrees well with previous publications [4–7]. In [13], it was shown that such a behavior may be a quantum phenomenon, where the quantum linear magnetoresistance is determined by the formula

$$\rho_\alpha(\mathbf{n}) = \frac{f_\alpha(\mathbf{n}) N_i H}{\pi (n_e - n_h)^2 ec}. \quad (1)$$

Here, $\rho_\alpha(\mathbf{n})$ is the basic part of the resistivity tensor in the plane perpendicular to the vector $\mathbf{n} = \mathbf{H}/H$, N_i is the defect concentration, and $f_\alpha(\mathbf{n})$ is a function of the order of unity. The linear magnetoresistance as a quantum phenomenon is inherent in semimetals with low carrier concentrations and small effective masses. Note that $NbSe_3$ satisfies these conditions. According to [14], the carrier concentration in $NbSe_3$ is $\sim 10^{18}$ cm^{-3} and the effective mass is $m^* = 0.24 m_e$ [7].

Figure 1 shows the magnetoresistance R of one of the samples under investigation in a magnetic field of $B = 8.5$ T versus the angle θ between the field direction and the c axis of the crystal. One can see a minimum of magnetoresistance at $\theta \approx 30°$. To clarify the nature of this anomaly, we measured the dependences of magnetoresistance on the magnetic field for different orientations of the latter. The results of these measurements are shown in Fig. 2. In magnetic fields $B > 3.5$ T, one can clearly distinguish the SdH oscillations. The amplitude of these oscillations is maximal at $B \parallel c$, decreases rapidly as the field deviates from the c axis, and almost vanishes at $\theta \approx 40°$.

The space–time structure of the SdH oscillations has the form of waves. Evidently, each wave corresponds to the same quantum number n. The magnetic field magnitude corresponding to a given n increases with θ. The phase of the oscillations varies accordingly. One can see that, at $\theta \approx 30°$ and $B = 8.5$ T, the phase of the oscillations changes by π and becomes opposite to the phase observed at $\theta = 0$. This behavior explains the presence of the minimum in the dependence $R_n(\theta)$ shown in Fig. 1. Such a considerable phase change cannot be attributed to a change in the SdH oscillation frequency, because, according to [4, 5], the rotation of the magnetic field about the a^* axis in the angular range under study leads to only a small change in the SdH oscillation frequency (from 0.28 to 0.30 MHz).

As is known, SdH oscillations are attributable to the variations of the density of states at the Fermi surface due to the intersection of the latter with the Landau levels with an increase in the magnetic field. The change observed in the magnetic field magnitude corresponding to the coincidence of a given nth level with the Fermi surface may be interpreted as either a change in the Fermi energy, which is impossible in our case, or a situation where the quantization is governed not by the whole value of B but by part of it.

In the case under consideration, there are reasons to believe that the electron spectrum is axisymmetric. Indeed, according to [4, 5], the Fermi surface pockets

are shaped like ellipsoids elongated along the *c* axis. Then, for the electron energy, we have

$$\varepsilon = \frac{p_x^2 + p_y^2}{2m_x} + \frac{p_z^2}{2m_z}. \quad (2)$$

In our case, the *z* axis is parallel to the *c* axis of the crystal, and the *x* axis, to the *b* axis of the crystal. Then, the Landau energy levels are determined by the expression

$$\varepsilon(p_z) = \frac{e\hbar H q^{1/2}(\theta)}{m_x c}\left(n + \frac{1}{2}\right) + \frac{p_z^2}{2m_z q(\theta)}, \quad (3)$$

where θ is the angle between the field direction and the *z* axis and

$$q(\theta) = \cos^2\theta + (m_x/m_z)\sin^2\theta. \quad (4)$$

Figure 3 shows the magnetic field B_m corresponding to the maximum of the SdH oscillations for a given quantum number versus the angle θ between the magnetic field direction and the *c* axis. The solid curve represents the function

$$\frac{B_m(\theta = 0)}{(\cos^2\theta + (m_x/m_z)\sin^2\theta)^{1/2}},$$

where the cyclotron mass ratio m_x/m_z is used as the fitting parameter. The best agreement of experimental data with the calculated curve is achieved at $m_x/m_z = 0.10$. The same ratio should occur between the axes of the ellipsoids of the Fermi surface. Note that the value obtained here is almost 1.5 times smaller than the value $m_x/m_z = 0.14$ obtained in [5]; i.e., according to our data, the ellipsoid of the Fermi surface is more elongated along the *c* axis. Actually, this means that the momenta of the normal carriers that are not condensed in CDWs are mainly oriented along the *b* axis and that the quantization of orbital motion is determined by the magnetic field component perpendicular to this axis.

The result obtained suggests a fairly simple explanation for the presence of coherent (with momentum conservation) tunneling in $NbSe_3$ in the direction perpendicular to its conducting layers [2, 3]. Namely, the results of our study show that the momenta of the majority of carriers that are not condensed in CDWs are oriented along a certain direction (parallel to the *b* axis). Then, interlayer tunneling is only possible if the tunneling occurs without any changes in the direction and magnitude of the momentum. The first of these conditions follows from the fact that the momenta of most carriers are oriented along a certain direction and, hence, the density of states for this direction in the momentum space should be much higher than that for other directions. The second condition follows from the first one and from the fact that the carriers localized in the pockets are on the Fermi surface. At this point, the question arises: Does the fact that the carriers that are not condensed in CDWs are mainly oriented along the *b* axis mean that the energy gap in this direction is absent?

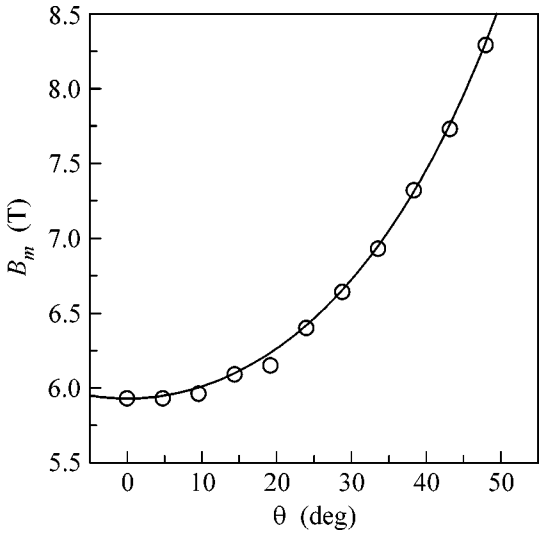

Fig. 3. Magnetic field corresponding to a fixed quantum number vs. the angle between the field direction and the *c* axis of the crystal. The solid curve is the function $B_m(\theta_m = 0)/(\cos^2\theta + (m_x/m_z)\sin^2\theta)^{1/2}$ at $(m_x/m_z) = 0.10$.

According to the data reported in [15], the point-contact experiments with $NbSe_3$ revealed the energy gap singularities for orientations along all three main crystallographic axes, including the *b* axis. The presence of normal carriers in this case can be explained by "imperfect" nesting, when a small indirect gap appears in addition to the direct CDW gap. Depending on the degree of this "imperfection," the indirect gap may be equal to zero, and the material will be in a semimetal state [16]. Possibly, this is the case for $NbSe_3$.

Another explanation is based on the assumption that the order parameter in $NbSe_3$ has an unusual symmetry. In this case, the presence of normal carriers localized in the pockets is a consequence of the fact that the order parameter is equal to zero in a certain direction (along the *b* axis), and the momenta of normal carriers should be strictly oriented in the given direction. Such a situation is known to occur in high-temperature oxide superconductors. Then, the observation of the energy gap singularity in this direction in [15] should be attributed to the contribution due to the injection of carriers in other directions, because the point contacts used in the cited study were not strictly oriented. As was shown in [17], when the magnetic field is oriented along the conducting planes, the magnetoresistance should be minimal in the direction parallel to that of the momenta of normal carriers. A similar situation is observed in our study in the magnetoresistance measurements along the *b* axis and also when the current is oriented along the *a** axis. Note that CDWs with an unusual symmetry of the order parameter were observed in other experiments,

and their properties are the object of active investigation [18, 19].

Thus, using $NbSe_3$ as an example, we have demonstrated the possibility of determining the properties of the Fermi surface from measurements of the phase of SdH oscillations. The data obtained show that the quasi-momenta of carriers that are not condensed in CDWs are predominantly oriented along the *b* axis. This result gives an insight into the origin of the coherent interlayer tunneling observed in [2, 3].

This work was supported by the Russian Foundation for Basic Research (project nos. 02-02-17263 and 00-02-22000 CNRS) and the INTAS (grant no. 01-0474).

REFERENCES

1. *Charge Density Waves in Solids*, Ed. by L. Gor'kov and G. Grüner (Elsevier, Amsterdam, 1989); G. Grüner, in *Density Waves in Solids* (Addison-Wesley, Reading, Mass., 1994).
2. Yu. I. Latyshev, A. A. Sinchenko, L. N. Bulaevskiĭ, *et al.*, Pis'ma Zh. Éksp. Teor. Fiz. **75**, 103 (2002) [JETP Lett. **75**, 93 (2002)].
3. Yu. I. Latyshev, P. Monceau, A. A. Sinchenko, *et al.*, J. Phys. A: Math. Gen. **36**, 9323 (2003).
4. R. M. Fleming, J. A. Polo, Jr., and R. V. Coleman, Phys. Rev. B **17**, 1634 (1978).
5. P. Monceau and A. Briggs, J. Phys. C: Solid State Phys. **11**, L465 (1978).
6. O. Laborde, A. Briggs, J. Richard, and P. Monceau, Europhys. Lett. **3**, 1019 (1987).
7. R. V. Coleman, M. P. Everson, Hao-Au-Lu, *et al.*, Phys. Rev. B **41**, 460 (1990).
8. R. V. Coleman, M. P. Everson, G. Eiserman, and A. Johnson, Phys. Rev. B **32**, 537 (1985).
9. J. Richard, P. Monceau, and M. Renard, Phys. Rev. B **35**, 4533 (1987).
10. M. P. Everson, A. Johnson, Hao-Au-Lu, and R. V. Coleman, Phys. Rev. B **36**, 6953 (1987).
11. T. M. Tritt, D. J. Gillespie, and A. C. Ehrlich, Phys. Rev. B **37**, 5552 (1988).
12. P. Monceau and J. Richard, Phys. Rev. B **37**, 7982 (1988).
13. A. A. Abrikosov, J. Phys. A: Math. Gen. **36**, 9119 (2003).
14. N. P. Ong and J. W. Brill, Phys. Rev. B **18**, 5265 (1978).
15. A. A. Sinchenko and P. Monceau, Phys. Rev. B **67**, 125117 (2003).
16. C. A. Balseiro and L. M. Falicov, Phys. Rev. B **34**, 863 (1986).
17. L. N. Bulaevskii, M. J. Graf, and M. P. Maley, Phys. Rev. Lett. **83**, 388 (1999).
18. S. Chakraverty, R. B. Laughlin, D. K. Morr, and C. Nayak, Phys. Rev. B **63**, 94 503 (2001).
19. B. Dora, A. Virosztek, and K. Maki, Phys. Rev. B **66**, 115112 (2002).

Translated by E. Golyamina

JETP Letters, Vol. 81, No. 3, 2005, pp. 85–89. Translated from Pis'ma v Zhurnal Éksperimental'noĭ i Teoreticheskoĭ Fiziki, Vol. 81, No. 3, 2005, pp. 115–119.

Absorption of Dark Matter by a Supermassive Black Hole at the Galactic Center: Role of Boundary Conditions

M. I. Zelnikov and E. A. Vasiliev

Lebedev Physical Institute, Russian Academy of Sciences, Leninskiĭ pr. 53, Moscow, 117333 Russia

e-mail: zelnikov@lpi.ru, eugvas@lpi.ru

Received December 15, 2004

The evolution of the dark matter distribution at the Galactic center is analyzed. It is caused by the combination of gravitational scattering by stars in the Galactic nucleus (bulge) and absorption by a supermassive black hole at the center of the bulge. Attention is focused on the boundary condition on the black hole. It is shown that its form depends on the energy of dark matter particles. The modified flux of dark matter particles onto the black hole is calculated. Estimates of the amount of absorbed dark matter show that the fraction of dark matter in the total mass of the black hole may be significant. The density of dark matter at the central part of the bulge is calculated. It is shown that recently observed γ radiation from the Galactic center can be attributed to the annihilation of dark matter with this density. © *2005 Pleiades Publishing, Inc.*

PACS numbers: 95.35.+d, 95.85.Pw, 98.35.–a, 98.62.Jc

1. INTRODUCTION

Investigations of the distribution of dark matter in the nuclei of galaxies currently attract the interest of many researchers in view of both the effect of dark matter on the growth of supermassive black holes and the search for its possible annihilation radiation. In this work, we analyze the evolution of the distribution of dark matter at the Galactic center under the effect of scattering by stars at the Galactic center and absorption by the central black hole. We assume that dark matter consists of particles that undergo only gravitational interaction and possibly slightly annihilate (so-called weakly interacting massive particles, WIMPs) [1].

The interaction of the central black hole with its environment, including dark matter at the Galactic center (bulge), was analyzed in [2–6] and elsewhere. An approach in which the distribution function of the dark matter is written in terms of invariants of motion seems to be most consistent. In the case of spherically symmetric, sufficiently slow evolution (compared to dynamical time), such variables are the orbital angular momentum m, its projection m_z onto the z axis, and the radial action (adiabatic invariant)

$$I = \frac{1}{\pi}\int_{r_-}^{r_+} v(r)dr.$$

We use a model of the formation of the dark matter halo in which its spatial density profile before the formation of the Galaxy and baryonic compression had the form $\rho(r) \sim r^{-12/7}$ and the initial distribution function in terms of the variables I, m, and m_z has the form [7]

$$f(I, m, m_z) = f_0 I^{1/8}\delta(m^2 - l_0^2 I^2), \quad (1)$$

where $l_0 \sim 0.1$ is a small parameter. We emphasize that it is convenient to choose the radial action I rather than particle energy E as the basic variable when analyzing evolution in a slowly varying potential.

1.1. Kinetic equation. In the zeroth approximation, the distribution function of dark matter in the chosen variables does not change upon baryonic compression. Under the assumption that the black hole is formed at the coordinate origin, the increase in the black hole mass M_{bh} causes the absorption of particles whose angular momenta m are less than the critical value $m_g = 4GM_{bh}/c$, but the number of such particles turns out to be negligibly small [4]. However, the situation is significantly changed due to effects associated with the gravitational scattering of dark matter particles on bulge stars. These effects lead to the diffusion of particles in phase space [4, 6].

In the first approximation, the evolution of the distribution function is governed by the kinetic equation

$$\frac{\partial f(\{I_i\}, t)}{\partial t} = \frac{\partial}{\partial I_k}\left[R_{kl}\frac{\partial f}{\partial I_l}\right], \quad (2)$$

where $\{I_i\} = \{I, m, m_z\}$ and R_{kl} are the corresponding diffusion coefficients. Owing to the spherical symmetry of the evolution, m_z does not enter into the equations. In addition, I can be approximated as $I(E, m) \approx J(E) - \beta m$ [2], where $\beta = 1$ for the Coulomb potential of the black hole and $\beta \simeq 0.6$ for the isothermal potential of the bulge. Hereinafter, we will use J instead of I, because

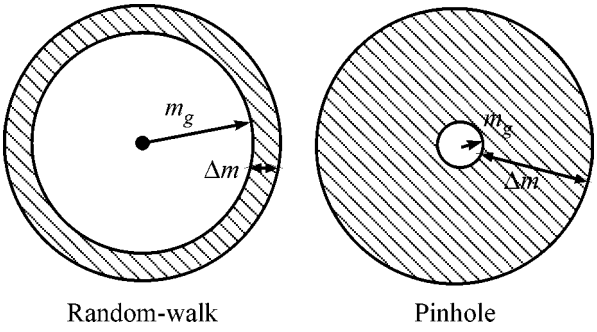

Two absorption regimes.

we are interested in the region of low angular momenta. Since the parameter l_0 is small, I can also be changed to J in initial distribution (1). It can be shown that the cross terms R_{12} are small in the region of interest [8]. Finally, the kinetic equation takes the form

$$\frac{\partial f(J, m, t)}{\partial t} = \frac{\partial}{\partial J}\left(R_{11}\frac{\partial f}{\partial J}\right) + \frac{1}{m}\frac{\partial}{\partial m}\left(mR_{22}\frac{\partial f}{\partial m}\right). \quad (3)$$

The diffusion coefficients were calculated in [8]. One-dimensional diffusion along the m axis is most substantial. It is responsible for the particle flux to the region of small orbital angular momenta and to their absorption by the black hole for $m \le m_g$. This process was analyzed in detail in [4, 8]. The effect considered there is as follows. Let us write Eq. (3) in the one-dimensional form

$$\frac{\partial f(J, m, t)}{\partial t} = \frac{1}{m}\frac{\partial}{\partial m}\left(mR_{22}\frac{\partial f}{\partial m}\right). \quad (4)$$

The initial condition is taken in the form of Eq. (1), and the boundary condition on the black hole corresponds to absorption: $f(J, m = m_g, t) = 0$. The diffusion coefficient R_{22} calculated for the isothermal bulge has the form

$$R_{22} = 0.46GM_sL_c\sigma_0, \quad (5)$$

where σ_0 is the velocity dispersion of stars in the bulge, M_s is the mass of a star (for simplicity, we assume that all stars have the same mass equal to $M_\odot$), and $L_c \simeq 10$ is the Coulomb logarithm.

In this formulation, the solution of the diffusion equation yields the following expression for the dark matter flux onto the black hole:

$$S(t) = 2(2\pi)^3\int_0^\infty f_0 J^{1/8} S_J(t) \propto R_{22}^{9/16} t^{-7/16}. \quad (6)$$

Here,

$$S_J(t) = \frac{0.18}{\ln\dfrac{l_0 J}{2m_g}}\frac{1}{t}\exp\left(-\frac{l_0^2 J^2}{5R_{22}t}\right) \quad (7)$$

is the flux in one-dimensional diffusion equation (4) with the initial condition $f(t = 0) = \delta(m^2 - (l_0J)^2)$.

However, the condition of the absorbing boundary is valid only for $\overline{\Delta m^2} \ll m_g^2$, where

$$\Delta m = \sqrt{2T(J)R_{22}} \simeq \frac{\sqrt{2\pi R_{22}J}}{\sigma_0} \quad (8)$$

is the rms change in the orbital angular momentum per orbital period $T(J)$. It is easy to show that this condition is violated even at rather low energies of the particle. In this work, we obtain a more accurate expression for the boundary condition and investigate its effect on the absorption rate of the dark matter. We start with the presentation of the Milky Way bulge model.

1.2. Bulge model. We assume that the star distribution in the bulge is isothermal, i.e., spherically symmetric and isotropic, and has the power-low density profile

$$\rho_{s(out)}(r) = \rho_0(r/R_0)^{-2}, \quad \rho_0R_0^2 = \sigma_0^2/2\pi G, \quad (9)$$

where σ_0 is the star velocity dispersion, which is independent of the distance from the center. In the inner part of the bulge—the region of the influence of the black hole—the density profile has a lower exponent [9]:

$$\rho_{s(in)}(r) = \rho_0(r/R_0)^{-3/2}, \quad (10)$$

where ρ_0 and R_0 are the same parameters as in Eq. (9), which assures the continuity of the star density at the boundary of the black hole influence region. We define the radius of the influence region such that the total mass of stars inside the region is equal to the mass of the black hole:

$$M_{\text{in}} = \int_0^{R_0}\rho_{s,\,in}(r')4\pi r'^2 dr' = \frac{8\pi}{3}\rho_0R_0^{3/2} = M_{bh}, \quad (11)$$

$$\frac{GM_{bh}}{R_0} = \frac{4}{3}\sigma_0^2.$$

In Milky Way, $\sigma_0 = 85$–90 km/s, and the current value $R_0 = 1.3$ pc corresponds to the observed mass of the black hole, $M_{bh} = 3 \times 10^6 M_\odot$ [9]. These values also give the observation-consistent normalization for the star density profile at the center [see Eq. (10)].

2. ABSORPTION OF PARTICLES BY THE BLACK HOLE AND BOUNDARY CONDITIONS

Thus, as was mentioned above, the absorbing-boundary approximation $f(m_g, J, t) = 0$ is valid only when $\Delta m \ll m_g$; i.e., change in the orbital angular momentum of the particle per period is small compared to the characteristic problem scale—the boundary orbital angular momentum. At the same time, as is easily seen from Eqs. (7) and (8), this condition is violated

at present, because the maximum of the flux comes from J values for which $\Delta m \gg m_g$.

To correctly describe the absorption of particles by the black hole, we consider two limiting cases (see figure): the random-walk approximation (absorption for $\Delta m \ll m_g$) and the pinhole approximation for $\Delta m \gg m_g$ (the names are taken from [10], where this process was considered in application to stars).

The absorption models are different in the random-walk and pinhole approximations. In the former case, the distribution function $f(m, J, t) \longrightarrow 0$ for $m \longrightarrow m_g$, and its derivative at the absorption boundary $m = m_g$ determines the flux. In the latter case, $f(m) \longrightarrow f_g$, where f_g is the nonzero boundary limit, and the absorption rate is determined as follows. There is a nonzero probability that the orbital angular momentum m of a particle increases by δm per orbital period such that $m + \delta m < m_g$ and, hence, the particle is captured by the black hole. Flux onto the black hole is determined as the sum of the absorption probabilities for all particles per period. At the same time, it is equal to the diffusion flux from higher m values, where the diffusion approximation is valid ($\Delta m < m$).

2.1. Boundary condition. Different absorption regimes can be described by the following modification of the boundary condition:

$$\left(f - m_g\alpha\frac{\partial f}{\partial m}\right)\Big|_{m = m_g} = 0. \quad (12)$$

Values $\alpha \ll 1$ correspond to the random-walk approximation, and $\alpha \gg 1$, to the pinhole approximation. Therefore, if the distribution function at the boundary is given as $f(m = m_g) = f_g$ and the flux is continuous and varies slightly for low m values, the distribution function near the boundary has the form

$$f(m) = f_g\left(1 + \frac{1}{\alpha}\ln\frac{m}{m_g}\right). \quad (13)$$

Our aim is to obtain expressions for α in the limit $\alpha \gg 1$ and for modified flux $S_J(t)$ of particles with the radial action J onto the black hole in this limit. To this end, we calculate the number of particles that diffuse into the region $m < m_g$ and are absorbed by the black hole during one orbital period. We assume that the probability distribution for obtaining a given increment δm of the orbital angular momentum of the particle is Gaussian with the variance $\overline{\delta m^2} = \Delta m^2$ and mean value $\overline{\delta m} \ll \Delta m$ [10]:

$$p(m, \delta m) = \frac{1}{\sqrt{2\pi}\Delta m}\exp\left(-\frac{\delta m^2}{2\Delta m^2}\right) \times \frac{1 + \delta m/m}{\frac{1}{2}\left[1 + \mathrm{erf}\left(\frac{m}{\sqrt{2}\Delta m}\right)\right] + \frac{\Delta m}{\sqrt{2\pi}}\exp\left(-\frac{m^2}{2\Delta m^2}\right)}. \quad (14)$$

The normalization is taken such that $\int_{-m}^{\infty} p(m, \delta m)d\delta m = 1$. The total number of particles absorbed per period is given by the expression

$$Q = \int_{m_g}^{\infty} 2m dm f(m) \int_{-m}^{-(m - m_g)} p(\delta m)d\delta m = S_J T(J). \quad (15)$$

At the same time, it is equal to the flux from larger m values per period:

$$Q = S_J T(J) = mR\frac{\partial f}{\partial m}T = \frac{f_g}{\alpha}RT = \frac{f_g\Delta m^2}{2\alpha}. \quad (16)$$

In the limit $\Delta m \gg m_g$, we obtain

$$\alpha = 2.8\left(\frac{\Delta m}{m_g}\right)^2, \quad (17)$$

which agrees with the results obtained in [10].

2.2. Dark matter absorption. To determine the expression for the particle flux onto the black hole, $S_J(t)$, we use the same procedure as for the pinhole limit considered in [6]. Namely, knowing the general form of the expression $S_J(t) \propto (1/t)\exp(-m_0^2/5Rt)$, we combine the solution $f(m, t)$ given by Eq. (13) and the Gaussian diffusion solution for the initial condition $f(t = 0) = \delta(m^2 - m_0^2)$. Thus, we obtain

$$S_J(t) = \frac{0.18}{\alpha + \ln\frac{m_0}{2m_g}}\frac{1}{t}\exp\left(-\frac{l_0^2 J^2}{5Rt}\right). \quad (18)$$

This expression for flux differs from the above expression by an additional term α in the denominator. As was pointed out, at present $\alpha(J) \gg 1$ for J values from which flux is maximal and, therefore, the total flux is much lower than the value obtained without corrections. Indeed, the total flux is given by the expression

$$S(t) = 2(2\pi)^3\int_0^{\infty} dJ f_0 J^{1/8} S_J(t) \approx 9.5 f_0\left(\frac{5R_{22}t}{l_0^2}\right)^{9/16} t^{-1}(\beta + 1)^{-8/9}, \quad (19)$$

where the quantity

$$\beta = \frac{\sqrt{5R_{22}t}2\pi R_{22}}{20 l_0\sigma_0^2 m_g^2} \approx 7\left(\frac{t}{10^{10}\ \mathrm{yr}}\right)^{1/2}\left(\frac{M_{bh}}{3\times 10^6 M_\odot}\right)^{-2} \quad (20)$$

presents to a correction due to the modification of boundary condition (12). If the correction is disregarded ($\beta = 0$), expression (19) yields a power-low increase in the black hole mass $M_{bh}(t) \propto t^{9/16}$ [6]. The estimate for the mass directly depends on the parameters f_0 and l_0 of the initial distribution of dark matter. Accepting $f_0 =$

6×10^9 g $(\text{cm}^2/\text{s})^{-9/8}$ and $l_0 = 0.1$ for Milky Way according to [6], we estimate the mass as $M_{bh} \simeq 11 \times 10^6 M_\odot$ for the present time ($t = 10^{10}$ yr $= 3 \times 10^{17}$ s) and for a negligibly low initial mass of the black hole (under the assumption that mass increases due exclusively to the absorption of dark matter; i.e., it is a lower estimate for the mass).

The inclusion of the flux modification significantly changes the situation. As follows from Eq. (20), when the black hole mass is low, $\beta \gg 1$ and, hence, the dark matter flux is also low. This is an evidence of the baryonic nature of a seed black hole. An upper estimate for the absorbed dark matter mass M_d can be obtained as the difference $M_d = M_0 - M_{bh}(0)$ between the final mass $M_{bh}(t_0 = 3 \times 10^{17}\ \text{s}) = M_0 = 3 \times 10^6 M_\odot$ and the initial mass $M_{bh}(0)$ obtained by solving the equation $dM_{bh}/dt = S(t)$. For the f_0 and l_0 values accepted above, we obtain $M_d = 0.67 M_0 = 2 \times 10^6 M_\odot$. If the f_0 value is one tenth of the previous value, $M_d = 0.11 M_0$. Another estimate can be obtained the supposition that the growth of the black hole due to the absorption of both dark and baryon matter has the power-low form $M_{bh}(t) = M_0 (t/t_0)^\gamma$. In this case, the mass of absorbed dark matter is given by the expression $M_d = \int_0^{t_0} S(t, M_{bh}(t))dt$. For the growth law with an exponent of $\gamma = 1/2$ (which was obtained in [5] from analysis of the absorption of stars), $M_d = 0.36 M_0$. The mass of dark matter absorbed by the black hole is proportional to the normalization constant f_0 of the dark matter distribution.

Thus, the correct formulation of the boundary condition considerably (approximately by an order of magnitude) reduces the estimate for the mass of dark matter absorbed by the black hole. The absorbed mass comprises up to one-third to one-half of the current black hole mass for the chosen normalization of the dark matter density. We emphasize that a similar consideration for the absorption of stars shows that the modification of the boundary condition is insignificant [5]. This difference results from the fact that dark matter particles initially have low orbital angular momenta and sooner reach the absorption boundary. Hence, flux at a given time comes from larger J values than those for stars. Hence, the boundary condition for dark matter changes its form at large J values more considerably.

3. DENSITY PROFILE OF DARK MATTER AND ITS ANNIHILATION

We consider the detection of γ radiation from the Galactic center, which is likely due to the annihilation of weakly interacting particles of dark matter (WIMPs), as a possible observational test of the current dark matter distribution. Photons of energies of several TeVs have been detected on the H.E.S.S. telescope, whose angular resolution of 3′–5.8′ corresponds to a region of radius of about 10 pc (the distance from the Galactic center is taken to be 8.5 pc). As was shown in [11], the observed photon flux can be attributed to the annihilation of supersymmetric particles with a mass of about 12 TeV whose density has a power-low profile and a mean value of about $\sim 10^3 M_\odot/\text{pc}^3$ in the central region 10 pc in size.

Knowing the distribution function of dark matter in phase space, it is easy to calculate its density profile as a function of the distance from the coordinate origin:

$$\rho(r) = \frac{2\pi}{r^2}\int_{J_{min}}^{\infty} dJ \frac{\partial E}{\partial J}\int_{m_g}^{m_{max}} 2m dm \frac{f(J, m, t)}{\sqrt{2(E - \Psi(r)) - \dfrac{m^2}{r^2}}}. \quad (21)$$

Let us calculate the dark matter density in the central region 10 pc in size. For simplicity, we assume that the potential in this region is determined by the central star cluster with a density of $\rho_s(r) = \sigma_0^2/2\pi G r^2$, where σ_0 is the star velocity dispersion. As follows from Eqs. (13) and (18),

$$\begin{aligned} f(J, m, t) &= f_0 J^{1/8} \frac{S_J(t)}{R}\left(\alpha + \ln\frac{m}{m_g}\right) \\ &= f_0 J^{1/8} \frac{\alpha + \ln\dfrac{m}{m_g}}{\alpha + \ln\dfrac{l_0 J}{2m_g}} \frac{0.18}{Rt} \exp\left(-\frac{l_0^2 J^2}{5Rt}\right). \end{aligned} \quad (22)$$

For $r \sim 10$ pc, $\alpha \sim 100$; therefore, the first fraction in Eq. (22) is close to unity. The quantity m_{max} in Eq. (21) is determined from the condition of zero denominator: $m_{max} = 2\sigma_0 r\sqrt{\ln[\sqrt{\pi} J/\sigma_0 r]} \simeq 2\sigma_0 r$ for $J > J_{min} = \sigma_0 r/\sqrt{\pi}$. However, approximation (22) is applicable only for low m values and, in particular, the total integral $\int_0^{m_{max}} f(J, m, t) 2m dm$ cannot be larger than $f_0 J^{1/8}$ according to the normalization condition. This gives the restriction $m \le m_0 = \sqrt{5Rt}$, which becomes important for $r > r_* \simeq 2$ pc. Thus, the internal integral in Eq. (21) is given by the expression

$$\begin{aligned} &\int_{m_g}^{\min(m_{max}, m_0)} \frac{2m dm r}{\sqrt{m_{max}^2 - m^2}} \frac{0.18 f_0 J^{1/8}}{Rt} \exp\left(-\frac{l_0^2 J^2}{5Rt}\right) \\ &= 2r \frac{0.18 f_0 J^{1/8}}{Rt} \exp\left(-\frac{l_0^2 J^2}{5Rt}\right) \\ &\times \begin{cases} m_{max} = 2\sigma_0 r, & r < r_* \\ 2\sigma_0 (r - \sqrt{r^2 - r_*^2}), & r > r_* \end{cases}. \end{aligned}$$

Since $\partial E/\partial J = 2\pi/T(J) = 2\sigma_0^2/J$, we have

$$\rho(r) = 16\pi\sigma_0^3 \min\left[1, 1 - \sqrt{1 - \left(\frac{r_*}{r}\right)^2}\right] \times \frac{0.18}{Rt}\int\limits_{J_{min}}^{\infty} dJ \frac{f_0 J^{1/8}}{J}\exp\left(-\frac{l_0^2 J^2}{5Rt}\right)$$

$$\simeq \frac{15\sigma_0^3}{Rt} f_0 \left(\frac{5Rt}{l_0^2}\right)^{1/16} \min\left[1, 1 - \sqrt{1 - \left(\frac{r_*}{r}\right)^2}\right] \simeq 10^3 \frac{M_\odot}{\text{pc}^3}\left(\frac{r}{10\text{ pc}}\right)^{-2}.$$

Thus, the estimate for the density agrees in order of magnitude with observations. In any case, the dark matter density does not exceed the star density, which is estimated as $\rho_s(r) = 1.2 \times 10^6\ (r/0.4\text{ pc})^\beta M_\odot/\text{pc}^3$, where $\beta \simeq 1.5$ and 2 for $r < 0.4$ pc and $r > 0.4$ pc, respectively [9]. For a more accurate determination of the dark matter density profile, it is necessary to take into account the diffusion along the J axis and a more exact expression for $f(J, m, t)$ in the limit $m \gg m_g$.

4. CONCLUSIONS

In this work, the diffusion of dark matter at the Galactic center has been considered. This diffusion is caused by scattering dark matter particles on bulge stars and is considered in the $\{J, m, m_z\}$ phase space, where J is the modified radial action. Diffusion along the axis of the orbital angular momentum m plays the main role in the absorption of dark matter. The presence of the black hole determines the boundary condition at $m = m_g$ that has different forms for small and large J values. The dark matter flux $S(t)$ calculated using the modified boundary condition is much smaller than the value obtained in previous works, where this modification was disregarded (i.e., the absorbing boundary approximation is applied). The amount of dark matter absorbed by the black hole may at present compose a significant fraction of the black hole mass. The dark matter density profile induced by diffusion within the central region 10 pc in size can be responsible for the observed γ radiation from the Galactic center, which arises upon the annihilation of dark matter particles.

We are grateful to A.S. Ilyin and V. I. Sirota for stimulating discussions. This work was supported by the Russian Foundation for Basic Research (project nos. 01-02-17829 and 03-02-06745) and Landau Foundation (Forschungszentrum Jülich).

REFERENCES

1. G. Bertone, D. Hooper, and J. Silk, hep-ph/0404175.
2. P. Gondolo and J. Silk, Phys. Rev. Lett. **83**, 1719 (1999).
3. D. Merritt, Phys. Rev. Lett. **92**, 201304 (2004).
4. A. S. Ilyin, K. P. Zybin, and A. V. Gurevich, JETP **98**, 1 (2004); astro-ph/0306490.
5. V. A. Sirota, A. S. Ilyin, K. P. Zybin, and A. V. Gurevich, astro-ph/0403023.
6. M. I. Zel'nikov and E. A. Vasil'ev, Kratk. Soobshch. Fiz. **9**, 9 (2003).
7. A. V. Gurevich and K. P. Zybin, Usp. Fiz. Nauk **165**, 723 (1995) [Phys. Usp. **38**, 687 (1995)].
8. M. Zelnikov and E. Vasiliev, Int. J. Mod. Phys. A (in press); astro-ph/0307524.
9. R. Genzel *et al.*, Astrophys. J. **594**, 812 (2003).
10. A. Lightman and S. Shapiro, Astrophys. J. **211**, 244 (1977).
11. D. Horns, submitted to Phys. Lett. B; astro-ph/0408192.

Translated by R. Tyapaev

JETP Letters, Vol. 81, No. 3, 2005, pp. 90–94. Translated from Pis'ma v Zhurnal Éksperimental'noĭ i Teoreticheskoĭ Fiziki, Vol. 81, No. 3, 2005, pp. 120–124.

Influence of the Orientation of a Crystal on Thermal Polarization Effects in High-Power Solid-State Lasers

I. B. Mukhin[1], O. V. Palashov[1], E. A. Khazanov[1], and I. A. Ivanov[2]

[1] *Institute of Applied Physics, Russian Academy of Sciences, ul. Ul'yanova 46, Nizhni Novgorod, 603950 Russia*
e-mail: khazanov@appl.sci-nnov.ru

[2] *Institute of Materials Science, Zelenograd, Moscow region, 103460 Russia*

Received November 5, 2004; in final form, December 14, 2004

The polarization thermal self-action of laser radiation propagating in an isotropic crystal has been studied experimentally. New nonlinear effects have been observed for the first time. These effects include a change in the symmetry of the depolarized-field distribution and the qualitative dependence of the degree of the self-induced depolarization on the geometry of the beam and crystal. The classical problem of self-induced depolarization has been analytically solved in the general form for an arbitrary orientation of any cubic crystal. The theoretical results agree well with the experimental data. The optimum orientation of the laser crystal has been determined, which can be effectively used in lasers with high average power. © *2005 Pleiades Publishing, Inc.*

PACS numbers: 42.60.Da, 42.25.Lc

The creation of simple and reliable sub-megawatt lasers with diffraction divergence is one of the most interesting physical tasks for the next decade. A recent increase in the average power of solid-state lasers was so large that they can now compete with chemical and molecular lasers, which are the traditional leaders in power. Rapid advances in single-mode solid-state lasers make it possible to expect that the 100-kW limit will soon be overcome, and their small sizes and reliability ensure a number of new scientific, technological, and special applications. The inevitable heat release in the active elements is one of the fundamental problems limiting the power of a laser. This release leads to a photoelastic-effect-induced change in radiation polarization from point to point of the cross section, i.e., to the thermally induced depolarization of radiation [1, 2].

Thermally induced depolarization in cubic crystals with the [111] orientation was investigated in [3–6]. The problem of the effect of the crystal orientation and choice of the best orientation (the orientation for which depolarization is minimal) was formulated as early as in 1971 [7]. However, the results obtained by Koechner and Rice [7] are correct only for the [111] orientation, because they made a mistake that was pointed out in [1, 8]. Koechner and Rice [7] supposed that the directions of eigen polarizations coincided with the radial and tangential directions. The same erroneous statement was present in a classical book [2] that has gone through five editions. This circumstance required the development of a new approach to the theoretical analysis of this problem. This new approach is reported in this work. In the general form, we have analytically solved the classical problem of thermally induced depolarization for an arbitrary orientation of any cubic crystal. A number of theorems on the physical distinguishability of the [001], [111], and [110] orientations have been proved, and the problem of the best and worst orientations has been solved. We present the experimental results for the thermal self-action of laser radiation that corroborate the theoretical conclusions.

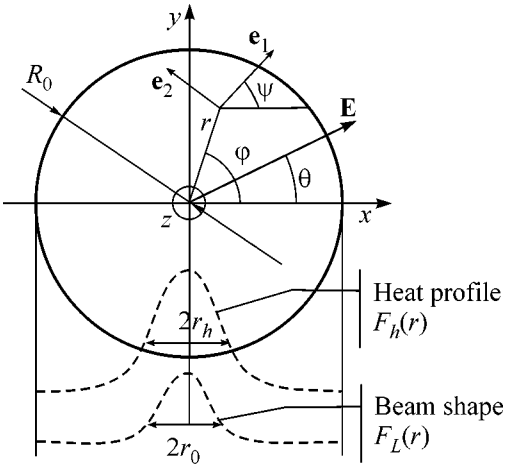

Fig. 1. Cross section of the cylindrical active element, where $\mathbf{e}_1$ and $\mathbf{e}_2$ are the eigen polarizations at the point (r, φ) and **E** is the radiation polarization.

Thermally induced birefringence at each point (r, φ) of a cross section is determined by the slope of eigen polarization Ψ with respect to the x axis (Fig. 1) and the phase difference δ between eigen polarizations:

$$\delta = \frac{\pi L n_0^3}{\lambda}\sqrt{(\Delta B_{11} - \Delta B_{22})^2 + 4\Delta B_{12}^2},$$
$$\tan(2\Psi) = \frac{2\Delta B_{12}}{\Delta B_{11} - \Delta B_{22}}. \quad (1)$$

Here, n_0 is the "cold" index of refraction; λ is the wavelength; L is the crystal length; and $\mathbf{\Delta B}$ is the dielectric impermeability tensor, whose elements depend on the temperature distribution and crystal orientation, i.e., on the mutual arrangement of the crystallographic axis (for a cubic crystal, it is immaterial which one) and the z axis. In the simplest case, the crystallographic axes coincide with the x, y, and z axes, which corresponds to the [001] orientation. Expressions for the tensor $\mathbf{\Delta B}$ were obtained in [1, 8, 9] for the [001] orientation, and it was shown that depolarization for this orientation may be lower than in the [111] orientation. An arbitrary position of the crystallographic axes can be specified by two successive rotations of the coordinate system xyz with the crystal lattice by the Euler angle α about the z axis and then by the Euler angle β about the y axis [7]. Thus, varying the α and β values, one can obtain any orientation of the crystal.

The following expressions for the elements of the tensor $\mathbf{\Delta B}$ were derived in [10] for an arbitrarily oriented cylindrical crystal with a length L that is much larger than its radius R_0:

$$\Delta B_{11} - \Delta B_{22} = \frac{\lambda}{\pi n_0^3 L} p\{g a_1(1-\xi) + h\cos(2\varphi)(a_2(1-\xi)+\xi) + h\sin(2\varphi)a_3(1-\xi)\},$$
$$2\Delta B_{21} = \frac{\lambda}{\pi n_0^3 L} p\{g b_1(1-\xi) + h\cos(2\varphi)b_2(1-\xi) + h\sin(2\varphi)(b_3(1-\xi)+\xi)\}, \quad (2)$$

where

$$a_1 = -\sin^2\beta\{\cos^2\beta - \cos^2\alpha\sin^2\alpha(\cos^2\beta + 1)\},$$
$$b_1 = 0.25\sin 4\alpha\cos\beta\sin^2\beta,$$
$$a_2 = 1 - \sin^2\beta\cos^2\beta - \cos^2\alpha\sin^2\alpha(\cos^2\beta + 1)^2,$$
$$b_2 = a_3,$$
$$a_3 = -0.25\sin 4\alpha\cos\beta(\cos^2\beta + 1),$$
$$b_3 = \sin^2 2\alpha\cos^2\beta;$$

$$g(u_h, R_h) = \frac{1}{R_h}\int_0^{R_h} dz\int_0^z F_h(u)du - \int_{u_h}^{R_h}\frac{dz}{z}\int_0^z F_h(u)du,$$
$$h(u_h) = \frac{1}{u_h}\int_0^{u_h} dz\int_0^z F_h(u)du,$$
$$\xi = \frac{2p_{44}}{p_{11} - p_{12}}, \quad p = \frac{P_h}{\lambda\kappa}\alpha_T\frac{n_0^3}{4}\frac{1+\nu}{1-\nu}(p_{11} - p_{12}),$$
$$u_h = (r/r_h)^2, \quad R_h = (R_0/r_h)^2,$$

P_h is the heat release power over the entire crystal volume; r_h and F_h are the radius and profile of pumping, respectively; and κ, ν, α_T, and p_{ij} are the thermal diffusivity, Poisson's ratio, the thermal expansion coefficient, and the photoelastic coefficients of active elements, respectively. Note that all material constants of active elements enter only into the parameter p, which is the normalized heat release power, and into the parameter ξ. Although expressions (1) and (2) are lengthy, they make it possible not only to obtain results for depolarization that can be easily analyzed (see below) but also to rigorously prove several general theorems valid for any crystals (ξ) and any pumping (p, R_h, F_h).

(i) There are only two orientations, namely, [001] ($\alpha = \beta = 0$) and [111] ($\alpha = \pi/4$, $\tan^2\beta = 2$), for which both $\delta(r = r^*)$ and $\Psi(r = r^*)$ are independent of both a heat source at $r > r^*$ and the crystal radius R_0.

(ii) There is only one orientation ([111]) for which $\Psi = \varphi$.

(iii) For $\xi > 0$, there is no orientation for which Ψ is independent of φ.

(iv) There are only two orientations ([001] and [111]) for which Ψ is independent of r.

(v) There is only one orientation ([111]) for which δ is independent of φ.

(vi) There are only two orientations, namely, [001] and [110] ($\alpha = 0$, $\beta = \pi/4$), for which all first derivatives of δ and Ψ with respect to α and β are equal to zero for any r and φ values.

The local depolarization degree Γ (at each point of the cross section) and cross-section-integrated depolarization degree γ (output-radiation power fraction whose polarization is orthogonal to the initial polarization) are given by the known expressions [1, 2]

$$\Gamma(r, \varphi) = \sin^2(\delta/2)\sin^2(2\Psi - 2\theta),$$
$$\gamma = \frac{1}{\pi r_0^2}\int_0^{2\pi} d\varphi\int_0^{R_0}\Gamma(r, \varphi)F_L\left(\frac{r^2}{r_0^2}\right)r dr. \quad (3)$$

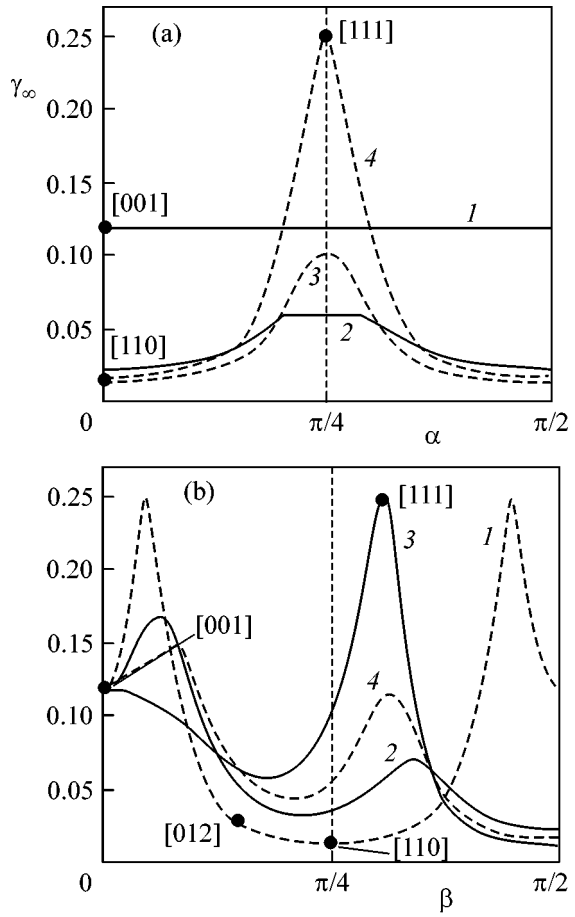

Fig. 2. Quantity γ_∞ vs. (a) α for β = (*1*) 0, (*2*) $\pi/6$, and (*3*) $\pi/4$ and (*4*) $\tan^2\beta = 2$ and (b) β for α = (*1*) 0, (*2*) $\pi/6$, and (*3*) $\pi/4$ and (*4*) $\tan^2\alpha = 2$ for a YAG crystal. The heat source is uniformly distributed over the entire crystal volume. The laser beam has a flat-top shaped profile with a radius of $r_0 = R_0/4$.

Here, R_0 and F_L are the radius and intensity profile of the beam and θ is the slope of the initial polarization (Fig. 1). From Eq. (3), we obtain

$$\gamma = \frac{R}{4\pi R_h}\int_0^{2\pi} d\varphi \int_0^{R_h} \sin^2\left(\frac{\delta}{2}\right) F_L\left(\frac{Ru_h}{R_h}\right) du_h - J_c\cos(4\theta) - J_s\sin(4\theta), \quad (4)$$

where

$$J_c = \frac{R}{4\pi R_h}\int_0^{2\pi} d\varphi \int_0^{R_h} \sin^2\left(\frac{\delta}{2}\right)\cos(4\Psi) F_L\left(\frac{Ru_h}{R_h}\right) du_h,$$

$$J_s = \frac{R}{4\pi R_h}\int_0^{2\pi} d\varphi \int_0^{R_h} \sin^2\left(\frac{\delta}{2}\right)\sin(4\Psi) F_L\left(\frac{Ru_h}{R_h}\right) du_h, \quad (5)$$

$$R = (R_0/r_0)^2.$$

Expressions (4) and (5) with Eqs. (1) and (2) completely determine the depolarization degree γ for any axisymmetric beam in any arbitrarily oriented cubic crystal for any axisymmetric distribution of heat release power.

Expression (4) can be significantly simplified in two particular cases of weak ($\delta \ll 1$) and strong ($\delta \gg 1$) birefringence. The former case for the coinciding shapes of pumping and beam (i.e., $F_L = F_h$, $R = R_h$) was considered in [10], where it was shown that the best and worse orientations are [001] and [111], respectively. Analysis of expressions (4) shows that [001] is the best orientation for any F_L, F_h, R, and R_h and that the worst orientation is either [111] for small R values or [110] for $R \gg 1$.

For active elements of high-power lasers, the case of strong birefringence is of the most interest. With increasing heat release, the function $\gamma(p)$ rapidly becomes constant. Differentiating Eq. (4) with respect to the angle θ and equating the resulting derivative to zero, one can easily find the optimum angle θ_{opt} at which γ is minimal. Therefore, the case of strong birefringence is conveniently characterized by the value

$$\gamma_\infty = \gamma_a(p \longrightarrow \infty, \theta = \theta_{opt}) = 0.25 - \sqrt{J_{c^\infty}^2 + J_{s^\infty}^2}, \quad (6)$$

where

$$J_{c^\infty} = \frac{R}{8\pi R_h}\int_0^{R_h}\left(\int_0^{2\pi}\cos(4\Psi(u_h, \varphi))d\varphi\right) F_L\left(\frac{Ru_h}{R_h}\right) du_h,$$

$$J_{s^\infty} = \left(\frac{R}{8\pi R_h}\int_0^{R_h}\left(\int_0^{2\pi}\sin(4\Psi(u_h, \varphi))d\varphi\right) F_L\left(\frac{Ru_h}{R_h}\right) du_h.\right) \quad (7)$$

For the particular cases of the [001] and [111] orientations, Eq. (6) yields

$$\gamma_\infty([001]) = 0.25 - \frac{1}{4}\left|\frac{1-\xi}{1+\xi}\right|, \quad \gamma_\infty([111]) = 0.25 \quad (8)$$

for any F_L, F_h, and ξ values. According to Eqs. (6) and (8), [111] is always the worst orientation.

It is more difficult to determine the best orientation. Figure 2 shows the function $\gamma_\infty(\alpha, \beta)$ for a YAG crystal, a flat-top shaped beam with a radius of $r_0 = R_0/4$ (R = 16), and uniform pumping ($R_h = 1$). As is seen in Fig. 2, [110] is the best orientation and ensures a depolarization of 1.3%. It is easily shown from Eq. (6) that θ_{opt} = 0 for the [110] orientation. We note that formulas presented in [1, 9] for the [110] orientation are approximate and cannot be used for most laser crystals. Calculations presented in [11] for homogeneous pumping in the [110] orientation were incorrect. Therefore, the angle θ_{opt} presented there was also incorrect, and the γ values were significantly underestimated.

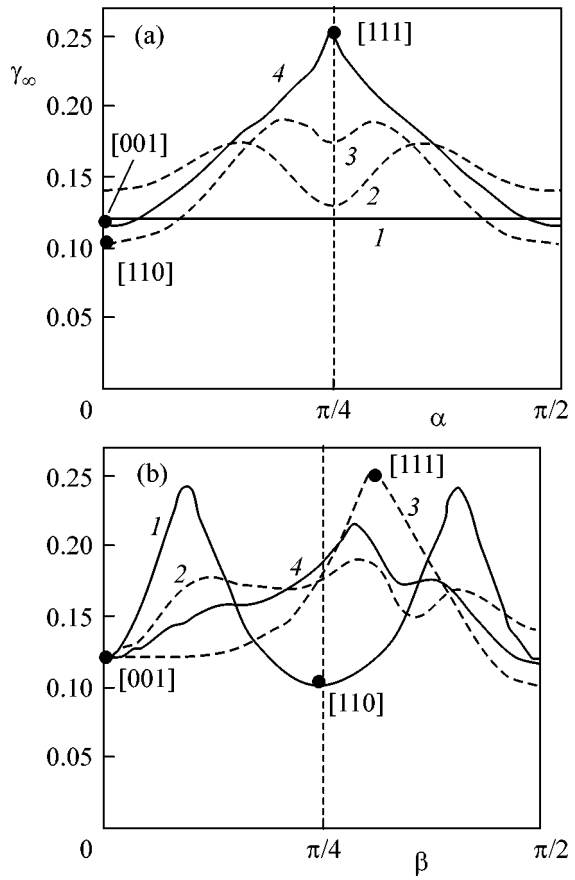

Fig. 3. Same as in Fig. 2, but when both the heat source and laser beam have a flat-top shaped profile with the same radius ($r_h = r_0 = R_0/4$).

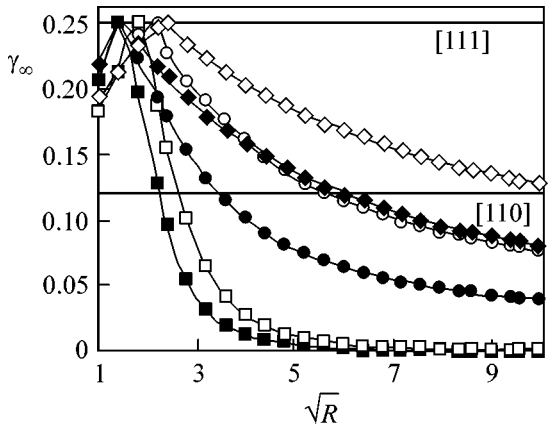

Fig. 4. Quantity γ_∞ vs. R for a YAG crystal in various geometries: a flat-top shaped beam profile with uniform pumping with R_h = (□) 1 and (○) R and (◇) a Gaussian beam with Gaussian pumping at $R_h = R$. The closed and open symbols correspond to the [110] and [012] orientations, respectively. For the [111] and [001] orientations, γ_∞ is independent of both R and geometry (horizontal straight lines without symbols).

If the heat-source radius is much smaller than the crystal radius (end pumping), the behavior is different (Fig. 3). For $r_h = r_0 = R_0/4$, depolarization in crystals with the [110] orientation is comparable to depolarization in [001] crystals. The significant difference between Figs. 2 and 3 is of great practical importance, because it is extremely inefficient to pump those regions in actual active elements that are free of a laser beam.

A considerable decrease in γ_∞ with increasing R is possible not only for the [110] orientation but also for other orientations. This conclusion follows from Figs. 2 and 3, as well as from Fig. 4, where the dependence $\gamma_\infty(R)$ is shown for three variants of the distribution of heat sources and laser beam. According to Figs. 2–4 and formula (6), [110] and [001] are the best orientations for $R \gg 1$ and $R \sim 1$, respectively.

To test the theoretical results, the local and integral depolarization was experimentally investigated for two TGG crystals with a diameter of 8.3 mm and the [001] and [110] orientations. Radiation from a continuous Yb fiber laser ($\lambda = 1076$ nm, power up to 52 W, beam profile close to a Gaussian) was used both for heating and for measurements of the depolarization; i.e., $F_h = F_L$.

For the [001] orientation, $\Gamma(r, \varphi)$ is a $\pi/2$-periodic function of the angle φ and is the well-known Maltese cross [1, 2] for any values of both the angle θ and R. At the same time, for the [110] orientation, the Maltese cross exists only for $\theta = N\pi/2$, where N is an integer (see Fig. 5). For other θ values, the pattern is significantly different, and the period of the function $\Gamma(\varphi)$ is equal to π.

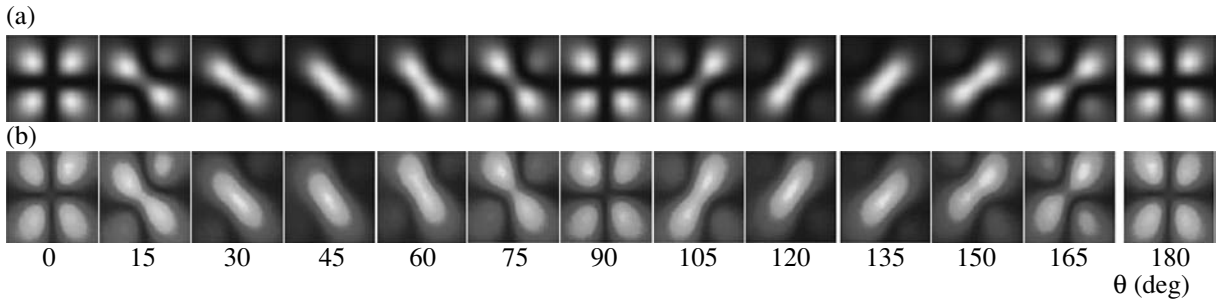

Fig. 5. (a) Theoretical and (b) experimental distributions of depolarized-radiation intensity for a TGG crystal with the [110] orientation for a beam radius of 0.45 mm. Distributions for a radius of 0.26 mm are qualitatively the same.

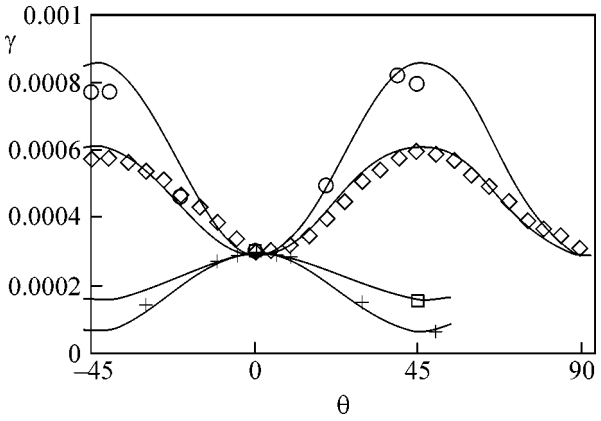

Fig. 6. (Curves) Theoretical and (points) experimental dependences $\gamma(\theta)$ for a crystal with (+) the [001] orientation for any beam radius and the [110] orientation for a beam radius of r_0 = (□) 1.8, (◇) 0.45, and (○) 0.26 mm.

The value $\gamma(\theta = 0)$ for the [110] orientation, as well as for the [001] orientation, is independent of R, which agrees well with theory (Fig. 6). At the same time, the value $\gamma(\theta = \pi/4 + N\pi/2)$ for the [110] orientation depends strongly on R. The depolarization degree γ has a minimum and a maximum at $\theta = \pi/4$ for small and large R values, respectively. Thus, the entire set of experimental data (Figs. 5, 6) agrees well with the theory.

Let us formulate the results. Analyzing and developing the previous results reported in [10], we have proved several general theorems on the fundamental physical distinguishability of the three orientations [111], [001], and [110]. The experimental data obtained for the [110] orientation agree well with the theoretical predictions.

The problem of choosing the best orientation has been solved in the general form. It has been shown that, for any cubic crystal and low heat release, [001] is always the best orientation, and the worst orientation is either [111] (for low ratios R of the crystal radius to the beam radius) or [110] (for high R values). The [111] orientation is always the worst orientation for high heat releases. The optimum orientation is [001] for $R \sim 1$ and [110] for $R \gg 1$. This property can be effectively used for active elements of disk geometry and crystal fibers. The above investigation concerned only the simplest optical scheme without depolarization compensation. The optimization of the orientation for various schemes where depolarization in active elements is compensated for, as well as for slab-form active elements, is a subject for future investigations. End diode pumping enables one to make the lateral surface of an active element unfree, which can also reduce depolarization upon the choice of the optimum orientation.

We are grateful to A.M. Sergeev for stimulating discussions and assistance in this work.

REFERENCES

1. A. V. Mezenov, L. N. Soms, and A. I. Stepanov, *Thermal Optics of Solid-State Lasers* (Mashinostroenie, Leningrad, 1986) [in Russian].
2. W. Koechner, *Solid-State Laser Engineering* (Springer, Berlin, 1999).
3. J. D. Foster and L. M. Osterink, J. Appl. Phys. **41**, 3656 (1970).
4. G. A. Massey, Appl. Phys. Lett. **17**, 213 (1970).
5. W. Koechner, Appl. Opt. **9**, 1429 (1970).
6. W. Koechner and D. K. Rice, IEEE J. Quantum Electron. **6**, 557 (1970).
7. W. Koechner and D. K. Rice, J. Opt. Soc. Am. **61**, 758 (1971).
8. L. N. Soms, A. A. Tarasov, and V. V. Shashkin, Kvantovaya Élektron. (Moscow) **7**, 619 (1980).
9. L. N. Soms and A. A. Tarasov, Kvantovaya Élektron. (Moscow) **6**, 2546 (1979).
10. E. Khazanov, N. Andreev, O. Palashov, *et al.*, Appl. Opt. **41**, 483 (2002).
11. I. Shoji and T. Taira, Appl. Phys. Lett. **80**, 3048 (2002).

Translated by R. Tyapaev

JETP Letters, Vol. 81, No. 3, 2005, pp. 95–98. Translated from Pis'ma v Zhurnal Éksperimental'noĭ i Teoreticheskoĭ Fiziki, Vol. 81, No. 3, 2005, pp. 125–128.

"Spreading" of a Biphoton in a Group-Velocity-Dispersion Medium and Two-Photon Interference

L. A. Krivitskiĭ and M. V. Chekhova*

Faculty of Physics, Moscow State University, Vorob'evy gory, Moscow, 119992 Russia

** e-mail: masha@qopt.phys.msu.su*

Received December 29, 2004

It is shown that two-photon Bell states can be prepared by "spreading" of a two-photon wave packet (biphoton) in a dispersive medium without compensating for group delays between photons with orthogonal polarizations or using narrow-band filters but by selecting the time correlation function. This is possible because two-photon interference effects are manifested in the shape of the time correlation function of intensity due to its spreading.

PACS numbers: 03.67.–a, 42.50.Dv

The transfer of quantum states of light over long distances, which is usually carried out using optical fibers, is important in problems of contemporary quantum optics. In this case, interesting effects can emerge. For example, it was shown in [1, 2] that, when two-photon light passes through a medium with group-velocity dispersion, the second-order correlation function in intensity "spreads" like a short pulse and takes the form of the spectrum in the far-field zone. We will show here that this spreading makes it possible to detect two-photon interference effects from the modulation of the time correlation function and can be used to solve one of the main problems in quantum optics, namely, preparation of Bell states.

Bell states [3] are maximally entangled states of a pair of photons, which are characterized by any two parameters, e.g., the spatial mode number and polarization (polarization–space Bell states). The simplest method of their preparation using spontaneous parametric down-conversion in the case of type-II noncollinear frequency-degenerate phase matching is described in [4]. In this case, two photons are emitted simultaneously into two different wavevector modes, and each photon is nonpolarized (i.e., a photon in a pair is polarized with the same probability in the horizontal or vertical direction, but the polarizations of these photons are correlated with each other). A basic feature of this method of preparation is the requirement that the group delay emerging between two photons in a pair due to birefringence in the nonlinear crystal must be compensated for. If the group delay is not compensated for, it is possible in principle to determine which of the two wavevector modes contains a vertically polarized photon and which contains a horizontally polarized photon from the order of the arrival of photons at the detectors. According to Feynman, such a *distinguishability in principle* serves as a criterion of the absence of interference (two-photon interference in the present case, which is a necessary property of Bell states), which means that the corresponding state is not of the Bell type.

Instead of compensation for group delay, another method is sometimes employed: narrow-band filters are placed in front of detectors, which leads to the appearance of two-photon interference. This fact is usually interpreted as follows: wave packets corresponding to individual photons are extended in time, and the delay between photons with different polarizations becomes insufficient to determine the polarization of a photon in each of two wavevector modes. Filtration is especially important in generating photon pairs in the regime of short (femtosecond) pulses, when the compensation method is inapplicable altogether [5]. Some authors report on preparing Bell states in the femtosecond regime by interference methods using two nonlinear crystals [6, 7] or a single crystal in interferometers with various configurations [8]. However, all of these methods are quite complicated and, for this reason, filtration is commonly used in applications.

Let us show that the effect of spreading of the biphoton correlation function in a medium with group-velocity dispersion makes it possible to observe two-photon interference using neither narrow-band filters nor polarization compensation but rather by observing the "fine structure" arising in the second-order correlation function. The idea of this method for preparing Bell states is that, instead of "extending" wave packets by narrow-band filters, they are made to spread in an optical fiber. We can consider a simple analogy: if we want two time-separated short pulses to overlap, these pulses can be passed through a fiber and thus be extended in time.

The biphoton wave function at the output of a nonlinear crystal in the case of type-II noncollinear fre-

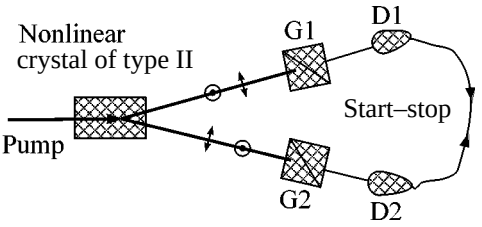

Fig. 1. Experimental layout for observing two-photon interference. A nonlinear type-II crystal serves as a source of biphotons in a nonpolarized state, and *G*1 and *G*2 are Glan polarization prisms mounted in the signal and idler arms. In experiment, the number of coincidences of photocounts from two detectors *D*1 and *D*2 is detected as a function of the orientation of the polarizer in one of the arms. The shape of the correlation function is detected using the start–stop circuit.

quency-nondegenerate spontaneous parametric down-conversion has the form [2]

$$|\Psi\rangle = |\text{vac}\rangle + \int d\Omega F(\Omega) \times \{a^\dagger_{H1}(\omega_0+\Omega)a^\dagger_{V2}(\omega_0-\Omega)e^{i\Omega\tau_0} + a^\dagger_{V1}(\omega_0+\Omega)a^\dagger_{H2}(\omega_0-\Omega)e^{-i\Omega\tau_0}\}|\text{vac}\rangle, \quad (1)$$

where $F(\Omega)$ is the biphoton spectral amplitude; Ω is the frequency detuning; $a^\dagger_{\sigma i}$ are the creation operators for photons in the vertical ($\sigma = H$) or horizontal ($\sigma = V$) polarization modes (in the laboratory system of coordinates) and in two wavevector modes labeled $i = 1, 2$; and $\omega_0 \equiv \omega_p/2$, where ω_p is the pumping frequency. Phase factors $e^{\pm i\Omega\tau_0}$ in both terms in Eq. (1) appear due to the difference in the group velocities for waves with two polarizations in the crystal; here, $\tau_0 \equiv DL/2$, where L is the crystal length and $D \equiv 1/u_V - 1/u_H$ is the difference between the inverse group velocities. State (1) resembles Bell state Ψ^+ but, strictly speaking, does not coincide with it if the delay τ_0 is not compensated for. For example, in the case of an uncompensated delay τ_0, two-photon interference, which will be considered below, is not observed for state (1).

In experiments on the observation of interference of Bell states (see, e.g., [4]), radiation in each of two wavevector modes is registered by a photodetector (Fig. 1), and polarization prisms (analyzers) are mounted in front of photodetectors. Photocounts from the detectors are fed to the input of a coincidence circuit. Interference of Bell states (two-photon interference) is manifested in oscillations in the coincidence count rate with a visibility close to 100% depending on the orientation of the polarization prisms (polarization interference) or depending on the phase delay introduced into the wavevector modes (space–time interference). (It should be noted that the intensity of light incident on the detectors and, hence, the rates of individual photocounts for all Bell states are independent of neither phase delay nor the orientation of the polarization prisms.) For example, for the Bell state Ψ^+ and polarization prisms oriented at $\mp 45^\circ$ to the vertical, a minimum in the coincidence counting rate must be observed. For this experimental configuration, substituting the standard SU(2) transform

$$a^\dagger_1(\omega) = \frac{a^\dagger_{H1}(\omega) + a^\dagger_{V1}(\omega)}{\sqrt{2}},$$

$$a^\dagger_2(\omega) = \frac{a^\dagger_{H2}(\omega) - a^\dagger_{V2}(\omega)}{\sqrt{2}}$$

for the creation operators at the output of the polarization prisms into Eq. (1), we can determine the state $|\Psi\rangle$ of the field behind the prisms (we do not present here this lengthy expression) and, then, the number of coincidences using the formula (see, e.g., [1])

$$R_c \sim \int dt \int d\tau |\langle\Phi(t,\tau)\rangle|^2, \quad (2)$$

where $|F(t,\tau)\rangle \equiv E^{(+)}_1(t)E^{(+)}_2(t+\tau)|\Psi\rangle$ and $E^{(+)}_{1,2}(t)$ are positive-frequency field operators on photodetectors. Integration with respect to t is carried out over the time interval during which the measurements are made (coincidences are counted), and integration with respect to τ is carried out within the limits of the coincidence-circuit resolution. In the stationary case, $|\Phi(t,\tau)\rangle$ is independent of t; consequently, integration with respect to t is reduced to multiplying the coincidence counting rate by the measuring time. To calculate the number of coincidences (Eq. (2)), the field operators should be represented in the form of a spectral decomposition in terms of annihilation operators (see, e.g., [9]). Taking into account the explicit form of a vector of state $|\Psi\rangle$ and commutation relations for the creation and annihilation operators, we obtain

$$|\Phi(t,\tau)\rangle = \int d\Omega F(\Omega)e^{-i\Omega\tau}\sin(\Omega\tau_0)|\text{vac}\rangle. \quad (3)$$

Using the convolution theorem, we can write this expression in the form

$$|\Phi(\tau)\rangle = \int dx F(x)\chi(\tau - x)|\text{vac}\rangle, \quad (4)$$

where

$$\chi(\tau) = \pi\{\delta(\tau-\tau_0) - \delta(\tau+\tau_0)\} \quad (5)$$

and function $F(\tau)$ is the Fourier transform of the function $F(\Omega)$ (i.e., the amplitude of the biphoton second-order correlation function).[1]

Substituting relation (5) into (4), we find that the coincidence counting rate has the form

$$R_c \sim \int d\tau |F(\tau-\tau_0) - F(\tau+\tau_0)|^2. \quad (6)$$

[1] As usual, the same letter denotes the function and its Fourier transform.

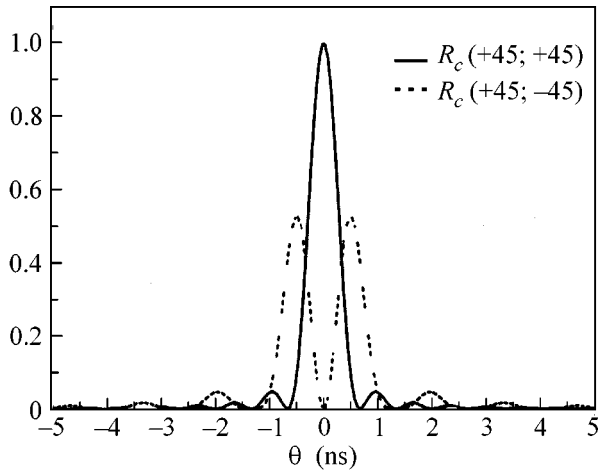

Fig. 2. Theoretical dependence of the integrands (solid curve) R_c(+45; +45) and (dashed curve) R_c(+45; –45) on the relative delay time θ. The parameters used in calculations are as follows: fiber length z = 500 m, crystal length L = 0.05 cm, and constant $k_2 = 3.2 \times 10^{-28}$ s^2/cm.

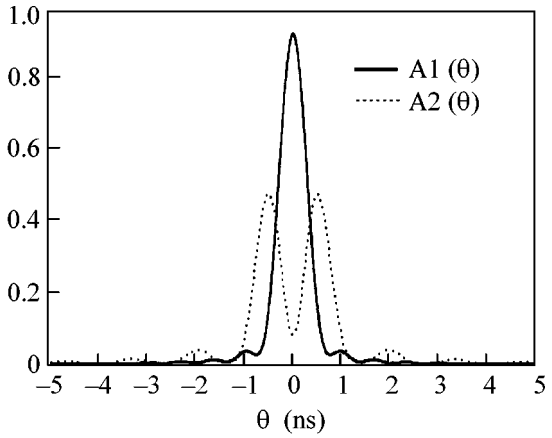

Fig. 3. Numerical results for the convolution of the functions (solid curve) R_c(+45; +45) and (dashed curve) R_c(+45; –45) with the apparatus function of the detecting system vs. the relative delay time. The apparatus function has the shape of a Gaussian curve with FWHM σ = 0.13, which corresponds to a system resolution of 0.9 ns. The visibility V of coincidence interference is equal to 84% for the time selection of the channel corresponding to zero delay.

It should be noted that, for an uncompensated delay τ_0, no interference is observed, because $F(\tau)$ has the shape of a rectangle of width τ_0 [10], and the two amplitudes appearing in expression (6) do not overlap.

Let an optical fiber of length z be mounted on the path of one of the wavevector modes behind the crystal (e.g., in mode 1). It was shown in [2] that the correlation-function amplitude for the sufficiently long fiber takes the form[2]

$$\tilde{F}(\tau) = \frac{1}{\sqrt{2\pi i k'' z}} e^{i(\tau - k'z)^2/2k''z} F(\Omega)\big|_{\Omega = \frac{\tau - k'z}{k''z}}, \qquad (7)$$

where k' and k'' are the first and second derivatives of the dispersion relation $k(\omega)$ for the fiber at frequency ω_0. Here, we assume that these quantities are independent of polarization, which is the case for a conventional (not birefringent) fiber. Taking into account that the spectral amplitude of a biphoton in the case of spontaneous parametric down-conversion with type-II phase matching has the form $F(\Omega) = \mathrm{sinc}(\tau_0\Omega)$ [10] and taking the effect of the fiber into consideration, we obtain

$$R_c \sim \int d\theta \left| f(\theta - \tau_0) - f(\theta + \tau_0) \right|^2, \qquad (8)$$

where $f(\theta) \equiv e^{i\theta^2/2\tau_0\tau_f} \mathrm{sinc}(\theta/\tau_f)$, where $\theta \equiv \tau - k'z$ is the time shift and $\tau_f \equiv k''z/\tau_0$ is the characteristic width of the correlation function behind the fiber. For a long fiber, we have $\tau_f \gg \tau_0$, and the amplitudes in expression (8) overlap. However, this is still insufficient for interference (as in the previous example with pulses, where the overlapping of the pulses behind the fiber is insufficient for interference), since interference is "smeared" due to rapid oscillations of phase factors in the amplitudes. To preserve interference, we must integrate only in narrow limits with respect to θ.

Taking into account the relation $\tau_f \gg \tau_0$, we can write expression (8) in the form

$$R_c(45°, -45°) \sim \int d\theta \frac{\sin^4(\theta/\tau_f)}{(\theta/\tau_f)^2}. \qquad (9)$$

If the polarization prisms are in positions +45°, +45°, the minus signs in relations (6) and (8) change to pluses, and relation (9) changes to

$$R_c(45°, 45°) \sim \int d\theta \frac{\sin^2(\theta/\tau_f)\cos^2(\theta/\tau_f)}{(\theta/\tau_f)^2}. \qquad (10)$$

If coincidences of photocounts are detected using the start–stop technique [1], a second-order time-extended correlation function [the integrand from Eq. (9) or (10), depending on the positions of the polarization prisms; see Fig. 2] can be observed in experiments. Naturally, the observed distribution is smeared, because the photodetectors have nonzero time resolution (usually about 1 ns). However, the correlation-function "modulation" will still be manifested for a sufficiently long fiber. Figure 3 shows the distribution expected in the start–stop scheme for the following experimental parameters: fiber length z = 500 m, group-velocity dispersion $k'' = 3.2 \times 10^{-28}$ s^2/cm in the fiber, crystal thickness L = 0.5 mm, difference in the inverse group velocities D = 1.5 ps/cm in the crystal, and a time resolution of 0.9 ns in the start–stop system (deter-

[2] The characteristic length of the fiber, beginning from which expression (7) is valid, is of the order of 1 m for typical parameters τ_0 = 1 ps and $k'' = 10^{-28}$ s^2/cm.

mined by the spread in the time response of the detectors). Thus, to observe two-photon interference, the third opportunity (i.e., analysis of the time correlation function of intensity) appears in addition to the rotation of the polarization prisms and scanning of phase delays.

If interference is detected using a coincidence circuit, Eqs. (9) and (10) determine the number of coincidences, depending on the positions of the prisms, with integration between the limits determined by the resolution T_c of the coincidence circuit. Accordingly, the visibility of interference is given by

$$V = \frac{\int_{-T_c/2}^{T_c/2} d\theta \frac{\sin^2(\theta/\tau_f)\cos(2\theta/\tau_f)}{(\theta/\tau_f)^2}}{\int_{-T_c/2}^{T_c/2} d\theta \frac{\sin^2(\theta/\tau_f)}{(\theta/\tau_f)^2}}. \quad (11)$$

For example, when a coincidence circuit with a "window" $T_c = 0.9$ ns is used with the above experimental parameters, the visibility is quite large, $V = 84\%$, in accordance with Eq. (11).

Thus, the use of a fiber, together with the time selection of the intensity correlation function, makes it possible to observe the interference of polarization Bell states without using polarization compensation or narrow-band filters. This circumstance provides another opportunity in a series of various methods for preparing Bell states. However, the manifestation of two-photon interference in a second-order correlation function is much more interesting.

We are grateful to S.P. Kulik and M. Genovese for fruitful discussions. This work was supported in part by the Russian Foundation for Basic Research (project nos. 02-02-16664 and 03-02-16444), INTAS (grant no. 2122-01), the Council of the President of the Russian Federation for Support of Young Russian Scientists and Leading Scientific Schools (project no. NSh-166.2003.02), and the Federal Program "Studies and Developments in Priority Trends of Science and Technology" (topic no. 15 in section "Fundamental Studies in Physics," block "Target Basic Research"). One of us (L.A.K.) is also grateful to INTAS for support (grant no. 03-55-1971).

REFERENCES

1. A. Valencia, M. V. Chekhova, A. S. Trifonov, and Y. H. Shih, Phys. Rev. Lett. **88**, 183601 (2002).
2. M. V. Chekhova, Pis'ma Zh. Éksp. Teor. Fiz. **75**, 271 (2002) [JETP Lett. **75**, 225 (2002)].
3. S. L. Braunstein, A. Mann, and M. Revzen, Phys. Rev. Lett. **68**, 3259 (1992); Phys. Rev. A **51**, R1727 (1995).
4. P. G. Kwiat, K. Mattle, H. Weinfurter, *et al.*, Phys. Rev. Lett. **75**, 4337 (1995).
5. G. Di Guiseppe, L. Haiberger, F. De Martini, *et al.*, Phys. Rev. A **56**, 1534 (1997); W. P. Grice and I. A. Walmsley, Phys. Rev. A **56**, 1627 (1997).
6. P. G. Kwiat, E. Waks, A. White, *et al.*, Phys. Rev. A **60**, R773 (1999).
7. Y. H. Kim, M. V. Chekhova, S. P. Kulik, *et al.*, Phys. Rev. A **63**, 062301 (2001).
8. D. Branning, W. P. Grice, R. Erdmann, and I. A. Walmsley, Phys. Rev. Lett. **83**, 955 (1999); Y.-H. Kim, M. V. Chekhova, W. P. Grice, *et al.*, Phys. Rev. A **67**, 010301 (2003).
9. D. N. Klyshko, *Photons and Nonlinear Optics* (Nauka, Moscow, 1980) [in Russian].
10. M. H. Rubin, D. N. Klyshko, Y. H. Shih, and A. V. Sergienko, Phys. Rev. A **50**, 5122 (1994).

Translated by N. Wadhwa

JETP Letters, Vol. 81, No. 3, 2005, pp. 99–101. Translated from Pis'ma v Zhurnal Éksperimental'noĭ i Teoreticheskoĭ Fiziki, Vol. 81, No. 3, 2005, pp. 129–132.

Observation of the Elastic Quasi-Mosaicity Effect in Bent Silicon Single Crystals

Yu. M. Ivanov*, A. A. Petrunin, and V. V. Skorobogatov

Petersburg Nuclear Physics Institute, Russian Academy of Sciences, Gatchina, 188300 Russia

** e-mail: yumi@pnpi.spb.ru*

Received December 6, 2004

A considerable elastic quasi-mosaicity effect has been observed upon the diffraction of x-rays on a bent silicon single-crystal plate. It has been shown that the effect depends on the choice of reflecting crystallographic planes and the orientation of the plate cut. The effect can be applied to improve the characteristics of silicon single-crystal monochromators of electromagnetic radiation and silicon single-crystal deflectors of charged-particle beams. © *2005 Pleiades Publishing, Inc.*

PACS numbers: 07.85.–m, 61.10.–i, 61.85.+p

In crystal-diffraction gamma spectroscopy, the known elastic quasi-mosaicity effect for quartz arises when quartz plates, which are used for the diffraction of radiation in focusing spectrometers, are bent to a cylinder. The effect results in the broadening of the diffraction profiles of gamma lines and changes the linear dependence of the integrated reflection coefficient on photon energy to a quadratic dependence. This effect is attributed to the anisotropic properties of quartz, which lead to the bending of radiation-diffracting atomic plates coinciding with the normal cross sections of the unbent plate. The bending angle depends on the cut of the plate with respect to the crystallographic axes and can reach a value of several tens of angular seconds for certain crystallographic planes, which is several orders of magnitude larger than the natural mosaicity of quartz. The above explanation of the effect was given by Sumbaev [1–3] and used by him and his collaborators to increase the efficiency and resolution of focusing crystal-diffraction spectrometers.

At present, single-crystal silicon has become a widely used material for manufacturing diffraction plates. However, its elastic quasi-mosaicity is poorly studied. This circumstance stimulated the present study. Another motivation is the search for new methods for bending atomic planes of single-crystal silicon for the channeling of protons of high and ultrahigh energies by short crystals [4, 5].

A noticeable elastic quasi-mosaicity effect in silicon for the (022) crystallographic plane was predicted in [6], where some bending schemes in application to crystal-diffraction spectrometers were analyzed using the calculation procedure for the deformed state of a bent anisotropic crystal plate [7]. In accordance with the cut angle recommended in [6], a silicon plate with the (022) crystallographic plane perpendicular to the large faces was manufactured and analyzed on an x-ray diffractometer. No elastic quasi-mosaicity effect was found in this investigation.

To resolve the apparent contradiction, we performed new calculations of the elastic quasi-mosaicity effect using the procedure proposed in [7]. These calculations showed that the elastic quasi-mosaicity effect must be manifested for a silicon plate with the (111) plane perpendicular to the large faces, whereas the calculated elastic quasi-mosaicity effect vanishes for a plate with the (022) plane.

Figure 1 shows a plate of the orientation under consideration that is bent to a cylinder of radius ρ, along with plate-bending-induced change in the shape of the (111) crystallographic planes. In the calculation model, this change is associated with the coefficient k_9 entering into the expression for the x projection of the displacement Δr of an arbitrary plate point (x_0, y_0, z_0) in the plate coordinate system. This projection is represented in the form

$$\Delta r_x = -k_5 z_0^2 + k_{10} x_0^2 + 2k_{11} x_0 y_0 + k_9 y_0^2.$$

After bending, cross sections perpendicular to the large faces of the plate approximately take the shape of parabolic cylinders with the projection on the xy plane that is specified by the relation

$$x = k_9 y^2.$$

The coefficient k_9 for an arbitrary (hkl) crystallographic plane is determined by the elastic constants of the crystal, the cut angle of the plate in the (hkl) plane, the bending radius, and the bending method, which determines the boundary conditions of the problem. Figure 2 shows the coefficient k_9 as a function of the cut angle φ for the (111) plane and plate bending by the method of applied moments. As is seen, the coefficient

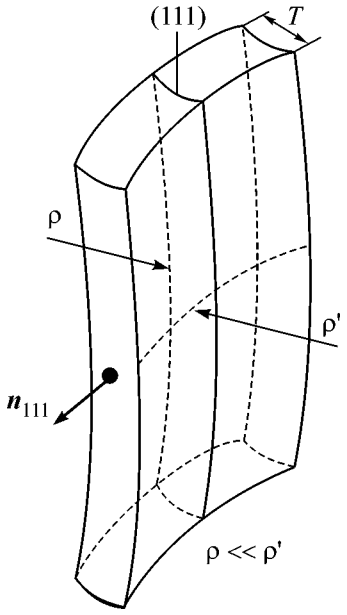

Fig. 1. Bending of the (111) crystallographic planes upon the bending of a silicon single-crystal plate to a cylinder of radius ρ. The radius ρ' characterizes the curvature in a plane perpendicular to the main bend plane.

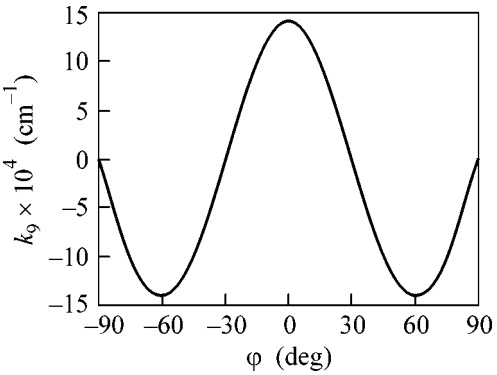

Fig. 2. Coefficient k_9 vs. the angle φ that characterizes the possible rotation of the plate cut about the normal to the (111) plane.

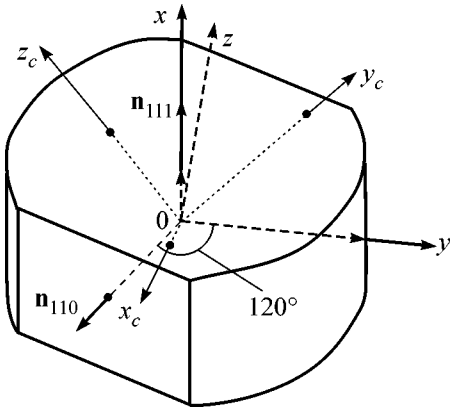

Fig. 3. Orientation of the plate coordinate axes *x*, y, and *z* that corresponds to the cut angle φ = 0° with respect to the silicon crystallographic axes x_c, y_c, and z_c for a sample grown along the [111] axis.

k_9 vanishes at the cut angles –90°, –30°, 30°, and 90° and takes an extreme value of 0.00141 cm^{-1} at the angles –60°, 0°, and 60°. The calculation was performed for a plate-bending radius of 1 m. Recalculation for another plate-bending radius is performed by dividing the coefficient k_9 by this radius measured in meters.

Figure 3 shows the orientation of the plate coordinate axes *x*, *y*, and *z* that corresponds to the cut angle φ = 0° with respect to the silicon crystallographic axes x_c, y_c, and z_c for a sample grown along the [111] axis. The axes of the *xyz* system are parallel to the plate edges, and the *xz* and *yz* coordinate planes are parallel to the large faces of the plate and the (111) crystallographic planes. The angle φ characterizes the possible rotation of the plate about the normal to the (111) plane and is measured from the *y* axis.

The calculated elastic quasi-mosaicity is determined by the bending of the (111) crystallographic planes, which is calculated for small strains as the difference between the derivatives of the function that describes the bending shape as calculated at the boundaries of the crystal. This bending is expressed by the formula

$$\Delta\theta = 2k_9T,$$

where Δθ is the plane bending and *T* is the plate thickness. It is seen that the elastic quasi-mosaicity follows the dependence of the coefficient k_9 on the cut angle φ.

On the basis of new calculations, a plate corresponding to the maximum coefficient k_9 was cut from single-crystal silicon. The plate has sizes 60 × 20 × 0.43 mm, and its orientation with the crystallographic axes is shown in Fig. 3 [the (111) plane is parallel to the 60 × 0.43-mm face]. The elastic quasi-mosaicity effect was experimentally observed on a two-crystal x-ray diffractometer [8] by measuring rocking curves before and after the bending of the plate to a cylinder.

Figure 4 shows the layout of the measurements. A tested silicon sample in the passage position was used as the first crystal, and a standard silicon crystal in the reflection position was used as the second crystal. The (111) crystallographic planes are diffracting planes in both crystals. An x-ray tube with a molybdenum anode was used as a radiation source. The beam incident on the sample under investigation was formed using a double-slit collimator, whose output slit had a width of 0.1 mm and a height of 5.0 mm. The angular divergence of the beam is equal to 1′, which is much smaller than the splitting of the fine-structure components. The Bragg diffraction angle for the MoK_{α_1} line in the first reflection order was equal to 6.5°, the natural width of the MoK_{α_1} line was equal to 9.2″, and the accuracy of determining the angular position of crystals was no worse than 0.5″.

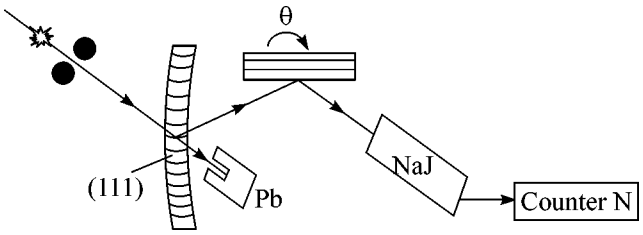

Fig. 4. Layout of rocking-curve measurement on a double-crystal diffractometer.

The measurement results are shown in Fig. 5, where both rocking curves are presented. The FWHM of the rocking curve of the unbent plate is equal to 6″ and is close to the width of the folding of diffraction curves of two ideal crystals. After the bending to a radius ρ = 92 cm, the rocking-curve width increases by a factor of 4 and reaches 24″ = 120 μrad. The observed broadening of the rocking curve agrees with the calculated elastic quasi-mosaicity, which is equal to 26″ and indicates a considerable elastic quasi-mosaicity effect in a bent plate. An increase in the width was accompanied by a considerable increase in intensity at the maximum of the rocking curve, which is a subject of special investigation that will be reported elsewhere.

Note that the shape of the bent plate differed from the cylindrical shape and was close to the saddle shape with a radius of ρ' = 410 cm in a plane perpendicular to the main bend plane (see Fig. 1). Deviation from the cylindrical shape is a common property of plates upon the bending by the method of applied moments, and the radius ρ' and curvature sign depend on the crystal symmetry, chosen crystallographic plane, and plate cut angle. Deviation from the cylindrical shape leads to broadening of the rocking curve. However, this broadening in the above measurement was much smaller than the elastic quasi-mosaicity effect.

A plate for a control experiment was made from the same ingot. This plate was identical to that studied above but differed in the cut angle, which was taken to be φ = –30° and corresponds to a calculated value of $k_9 = 0$. In the unbent state, the rocking curve of the plate with φ = –30° nearly coincides with a similar curve for the plate with φ = 0°. However, the control plate after the bending to a radius of ρ = 75 cm has absolutely different properties: the rocking curve is only slightly broadened and intensity at the maximum decreases simultaneously. This result is entirely explained by the deviation of the shape of the bent control plate from the cylindrical shape in the complete absence of the elastic quasi-mosaicity effect.

The experiment revealed the considerable elastic quasi-mosaicity effect in silicon and showed that a small change in the orientation of the cut of single-crystal silicon plates may significantly vary their deformed

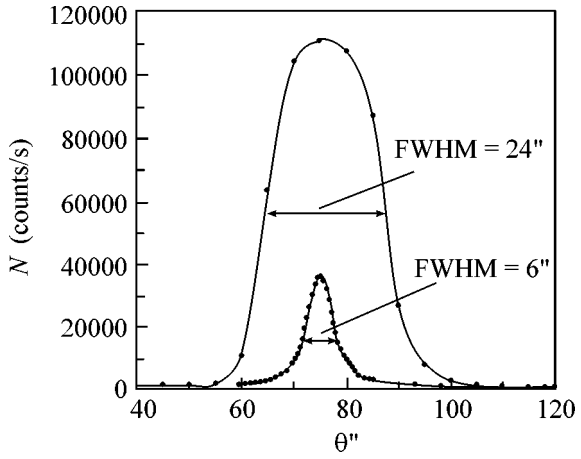

Fig. 5. Rocking curves for a plate notched at an angle of φ = 0° (6″) before and (24″) after bending.

state upon bending. We think that the use of this effect may improve the characteristics of silicon single-crystal monochromators of electromagnetic radiation and silicon single-crystal deflectors of charged-particle beams.

We are grateful to S.A. Vavilov and M.A. Koznov for assistance in manufacturing the crystals and L.P. Lapina for help in preparing the manuscript. This work was supported by the Russian Foundation for Basic Research, project nos. 01-02-18005 and 01-02-17992.

REFERENCES

1. O. I. Sumbaev, Zh. Éksp. Teor. Fiz. **32**, 1276 (1957) [Sov. Phys. JETP **5**, 1042 (1957)].
2. O. I. Sumbaev, *Crystal-Diffraction Gamma Spectrometers* (Gosatomizdat, Moscow, 1963) [in Russian].
3. O. I. Sumbaev, Zh. Éksp. Teor. Fiz. **54**, 1352 (1968) [Sov. Phys. JETP **27**, 724 (1968)].
4. A. G. Afonin, V. T. Baranov, V. M. Biryukov, *et al.*, Phys. Rev. Lett. **87**, 094802 (2001).
5. A. G. Afonin, V. T. Baranov, V. M. Biryukov, *et al.*, Pis'ma Zh. Éksp. Teor. Fiz. **74**, 57 (2001) [JETP Lett. **74**, 55 (2001)].
6. V. M. Samsonov and E. G. Lapin, Preprint No. 587, LIYaF AN SSSR (Leningrad Inst. of Nuclear Physics, USSR Academy of Sciences, Leningrad, 1980).
7. V. M. Samsonov, Preprint No. 278, LIYaF AN SSSR (Leningrad Inst. of Nuclear Physics, USSR Academy of Sciences, Leningrad, 1976).
8. S. G. Skornyakov, A. I. Smirnov, and G. P. Solodov, Preprint No. 1133, LIYaF AN SSSR (Leningrad Inst. of Nuclear Physics, USSR Academy of Sciences, Leningrad, 1985).

Translated by R. Tyapaev